Chapter 3
Gas-Based Detectors

Justin Beal, Kevin D. Berry, and Loren Funk

Abstract This chapter is devoted to thermal neutron detectors which rely on gas proportional detection technology, and in particular, detectors which use helium-3 as the proportional gas. The physics of neutron capture and charge creation and drift in helium-3 detectors is discussed. The construction and operation of position sensitive detectors, both linear PSD and 2-D, or area detectors, is described in detail. Materials of construction, detector signal processing electronics, and noise sources and noise analysis are among the topics covered. The chapter concludes with a section on neutron beam monitors, a specialized type of detector which is typically placed in the direct beam to provide neutron beam flux and timing information relevant to the neutron scattering experiment.

3.1 Neutron Detection in Helium-3

The ^{3}He-based gas-proportional counters are by far the most common type of detector installed in the neutron scatteringinstruments at the Spallation Neutron Source (SNS) and the High Flux Isotope Reactor (HFIR), comprising around 80% of the combined instrument suite. The three basic configurations are (1) the single-output gas-proportional detector tube, (2) the dual-output linear position-sensitive detector (LPSD) tube, and (3) the 2D multiwire proportional chamber. Most of the gas detectors are installed as arrangements of adjacent LPSD tubes, effectively providing relatively large areas (tens of square meters in some instances) of 2D detector coverage. LPSDs provide the flexibility of many different detector configuration options, as shown in Fig. 3.1. Planar, curved, or radial arrangements may be realized. The single-output tubes are installed either individually or side by side to construct a 1D detector array. In the multiwire proportional chambers, horizontal and vertical readout grids provide continuous neutron detection coverage over modest

J. Beal · K. D. Berry (✉) · L. Funk
Neutron Sciences Directorate, Oak Ridge National Laboratory, Oak Ridge, TN, USA
e-mail: bealjd@ornl.gov; berrykd@ornl.gov; funkll@ornl.gov

Y. Diawara (ed.), *Neutron Detectors for Scattering Applications*, Particle Acceleration and Detection, https://doi.org/10.1007/978-3-031-36546-1_3

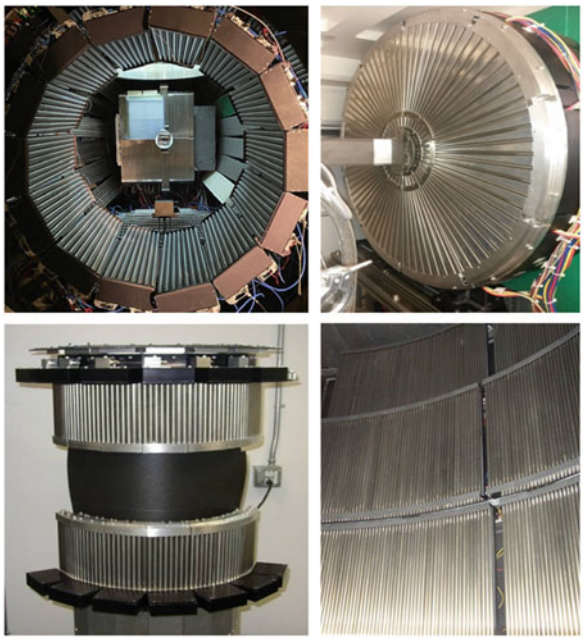

Fig. 3.1 Variety of detector configurations possible with arrangements of linear position–sensitive detectors (LPSDs). Clockwise from upper left: concave, radial, large area curved, and convex geometries

(60–250 cm^2) areas and good spatial resolution (1–3 mm) in 2D. Each of these detector types are discussed in more detail later in this chapter.

This section describes the process of neutron absorption in ^{3}He, the creation and distribution of the resulting ionization charge, and the operating principles of ^{3}He gas-proportional detectors.

3.1.1 Ionization Charge

Equation 3.1 describes the neutron conversion reaction with the ^{3}He nucleus, previously discussed in Chap. 2.

$$^1\mathrm{n} + {}^3\mathrm{He} \rightarrow {}^3\mathrm{H} + {}^1\mathrm{H} + 0.764\ \mathrm{MeV} \tag{3.1}$$

This reaction is exothermic, so the Q value energy of 0.764 MeV is imparted to the two reaction products—a tritium atom (triton) and a proton—as kinetic energy. This reaction has exactly two products, so the principle of conservation of linear momentum states that they must be emitted in antiparallel trajectories. Following the derivation in Chap. 2, the kinetic energies are distributed between the two reaction products according to their relative masses, thus the triton energy (E_T) is 191 keV, and the proton energy (E_P) is 573 keV.

Gas	First Ionization Potential (eV)	W-Value (eV/ ion pair)	
		Fast Electrons	Alpha Particles
H_2	15.6	36.5	36.4
He	24.5	41.3	42.7
N_2	15.5	34.8	36.4
Ne	21.6	35.4	36.8
Ar	15.7	26.4	26.3
Kr	14.0	24.4	24.1
Xe	12.1	22.1	21.9
CH_4	14.5	27.3	29.1
CO_2	13.8	33.0	34.2

Fig. 3.2 Table of ionization potentials and *W* values for several gases commonly used in proportional counters [1]

As these particles travel through the gas, they undergo scattering collisions with the ^{3}He gas atoms, losing kinetic energy with each interaction. Some scattering collisions result in ionization of the ^{3}He atom (with first ionization potential 24.5 eV), whereas others promote ground-state electrons to higher excitation states with no ionization. The W *value*, defined as the average energy required to produce one electron–ion pair, ranges from about 41–43 eV for ^{3}He. Because some fraction of the collisions results in electronic excitation rather than ionization, the *W* value average is always greater than the ionization potential. Comparing the average *W* value of 42 eV with the *Q* value of 764 keV suggests that 764,000/42, or approximately 18,000 electron–ion pairs are created within the ^{3}He gas following a single neutron-capture reaction (Fig. 3.2). Figure 3.2 tabulates the first ionization potentials and W-values for several gases commonly used in proportional counters.

The range of a 573 keV proton in 1 atm of ^{3}He is about 6 cm [2], much too long for a practical neutron detector that is expected to measure and record neutron interaction locations with centimeter or better precision. Proton range is inversely proportional to pressure, but even for common ^{3}He pressures of 10–20 atm, they are still too long for many applications. It is common practice to combine additional gases with the ^{3}He with the goal of reducing particle ranges to acceptable distances based on the detector's spatial resolution requirements. These so-called *stopping gases* typically have lower ionization and excitation energies and hence a greater potential for inelastic scattering collisions per unit track length than for ^{3}He alone. Commonly used stopping gases include Ar/CO_2 and CF_4.

Figure 3.3 shows the range of 573 keV protons and 191 keV tritons in several common stopping gases as a function of gas pressure, ranging from 0.1 to 10 atm [3]. Depending on the specific requirements of the detector, the stopping gas can vary from a fraction of a percent, to as much as 50% of the overall gas pressure in extreme cases.

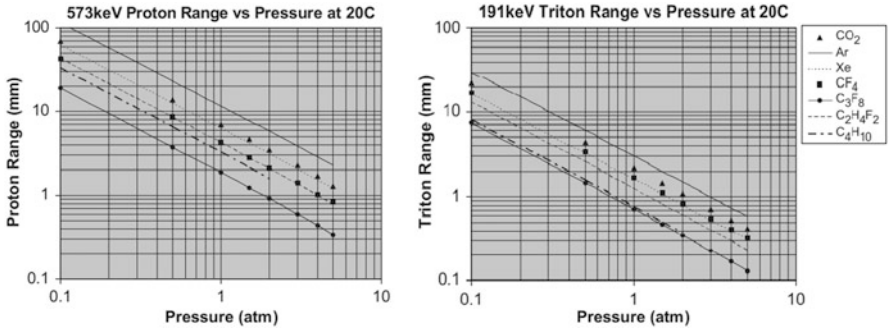

Fig. 3.3 Range of 573 keV protons (*left*) and 191 keV tritons (*right*) in various stopping gases as a function of pressure. (All data are from Stopping and Range of Ions in Matter simulations [3])

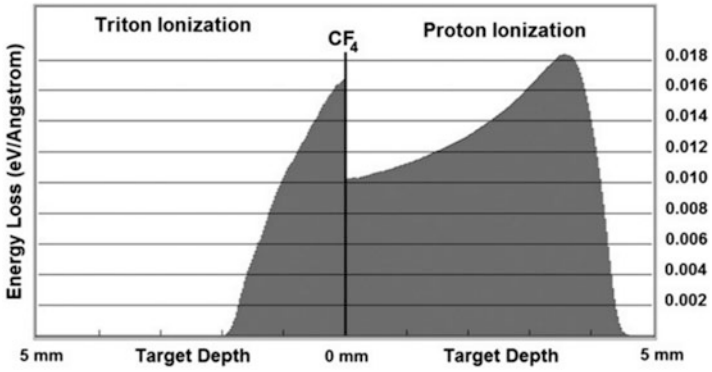

Fig. 3.4 Ionization distribution for 573 keV protons and 191 keV tritons as a function of distance traveled from the conversion site in 1 atm of CF_4 [3]

Because the proton carries three times as much kinetic energy as the triton, its range is generally larger. The resulting charge distribution is neither uniformly distributed nor centered about the interaction location. The centroid of the charge distribution is skewed closer to the proton endpoint, displaced from the interaction by about 0.4 times the proton range R_p [4]. To the extent that protons (and tritons) are emitted isotropically, the overall distribution of charge centroids for many detection events is about $0.8R_p$. Figure 3.4 is a plot of energy loss of the proton and the triton in 1 atm of CF_4. The ranges are determined by the endpoints in the energy-loss curves, roughly 4.5 mm for the proton and 2 mm for the triton. This is consistent with the values seen in Fig. 3.3 for CF_4.

Scattering collisions resulting in electron excitation are problematic for gas detectors. Visible and ultraviolet photons emitted during de-excitation can be absorbed in the detector (either in the gas or the detector wall) at points far removed from the original neutron interaction location, generating secondary electron emission that could falsely be recorded as a neutron event. To prevent this problem,

so-called *quench gases* are added to absorb this unwanted photon emission. Quench gases must be able to absorb the radiant energy and then undergo nonradiative (e.g., rotational, vibrational) de-excitations. Therefore, monatomic gas atoms are not suitable: a quench gas must be polyatomic to provide a mechanism for rotational or vibrational modes of de-excitation. Polyatomic stopping gases can however also act as quench gases (e.g., CO_2, C_3H_8, CF_4, CH_4, and C_2H_6). If a noble gas such as argon or xenon is used as the stopping gas, then a polyatomic gas must be added for photon quenching.

Strongly electronegative gases are detrimental to detector performance. *Electronegative gases* are gases that are likely to capture free electrons. Examples include oxygen, fluorine, chlorine, and water vapor. Electronegative gases within the detector gas volume act to decrease the signal charge amplitude, possibly degrading the signal-to-noise and spatial resolution. Therefore, electronegative gases are generally avoided as much as possible. Some detector manufacturers provide active filtering to remove electronegative gas species from the detection gas volume.

Selection of stopping and quench gases plays a role in the gamma sensitivity of ^{3}He neutron detectors. Gamma rays interact with matter via three main mechanisms: the photoelectric effect (PE), Compton scattering, or pair-production (PP). PP dominates at the highest gamma energies ($E_\gamma > 1.022$ MeV), the PE dominates in the lower energy regime. Both have a strong dependence on atomic number Z (PP is proportional to Z^2; PE is proportional to Z^n, with $4 < n < 5$). Figure 3.5 shows a graph of the cross section for gamma absorption for various gases commonly used in

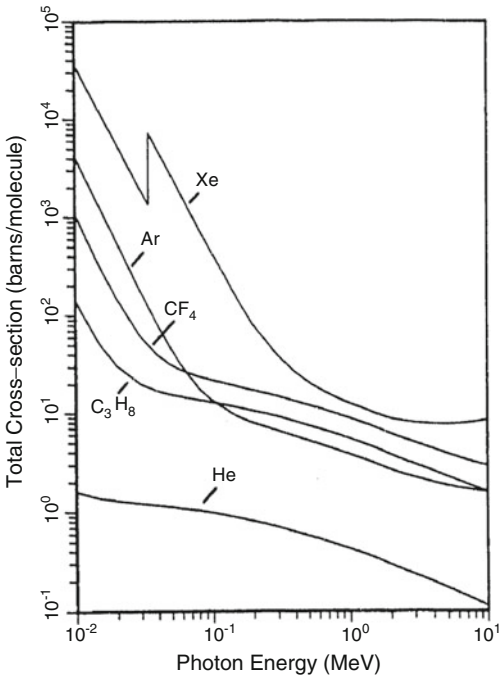

Fig. 3.5 Gamma-ray cross sections for materials commonly used in gas-proportional detectors [5]

gas detectors. The general trend of cross-section dependence on atomic number is apparent from the graph.

With the addition of different gases (stopping and quench) of typically lower W value, the resultant average energy per electron–ion pair also decreases, and therefore the number of electron–ion pairs generated by the overall process increases. Most of the ^{3}He gas detectors in use at SNS and HFIR have an ionization charge of about 4–5 fC. Considering the electron charge of 1.6×10^{-19} C, this corresponds to about 25,000–30,000 electron–ion pairs per neutron event.

Neutron capture efficiency is defined as the fraction of neutrons incident on a detector that undergo a nuclear conversion reaction. The most common expression for efficiency is derived from the Lambert law for beam attenuation in matter, given in Eq. (3.2):

$$I(x) = I_0 \exp\{-\mu x\} \tag{3.2}$$

Here, $I(x)$ is the transmitted beam intensity, I_0 is the incident beam intensity, μ is the linear attenuation coefficient (a material property of the absorbing medium), and x is the depth into the absorber where $I(x)$ is to be evaluated. Strictly speaking, this expression only applies for a narrow beam at normal incidence into a material of uniform attenuation coefficient. Because $I(x)$ is the transmitted intensity, it follows that $I_0 - I(x)$ is the absorbed intensity. Thus, the expression for beam absorption as a function of depth x is given by Eq. (3.3):

$$A = I_0 - I(x) = I_0 - I_0 \exp\{-\mu x\} = I_0(1 - \exp\{-\mu x\}) \tag{3.3}$$

Replacing x with the neutron conversion layer depth d gives the overall capture efficiency of a planar detector. Expressed as a fraction of incident beam intensity I_0, Eq. (3.3) becomes

$$Eff = \frac{I_0 - I(d)}{I_0} = 1 - \exp\{-\mu d\} \tag{3.4}$$

The absorption cross section σ from Chap. 2 is contained within the linear attenuation coefficient μ, along with the number density n of absorbing atoms. Recalling that σ is wavelength-dependent, Eq. (3.4) can be written as

$$Eff = 1 - \exp\{-n\sigma(\lambda)d\} \tag{3.5}$$

Applying dimensional analysis to the argument in the exponential confirms that n (cm^{-3}) × σ (cm^2) × d (cm) is dimensionless, as it must be.

Figure 3.6 is a plot of the neutron capture efficiency of a 1 cm thick planar gas detector containing 10 atm of ^{3}He. In this case, n is evaluated by multiplying the number density of atoms in a gas (2.69×10^{19} atoms/[cm^3·atm]) by 10 atm gas pressure to give 2.69×10^{20} atoms/cm^3. Neutron absorption in the detector window has been neglected.

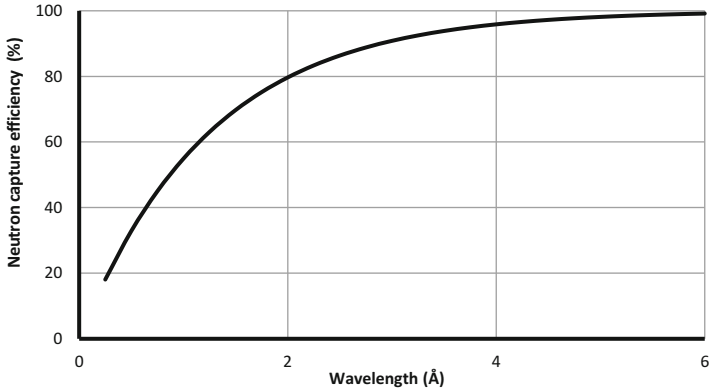

Fig. 3.6 Plot of neutron capture efficiency for a 1 cm thick gas detector containing 10 atm of ^{3}He. The capture efficiency is a function of the neutron wavelength

3.1.2 Ionization Mode vs. Proportional Mode

The previous section describes the formation of electron–ion pairs resulting from neutron capture in ^{3}He gas. No net electrical signal can be induced because the charges are created in essentially equal numbers. If there were no externally applied electric field to separate the positive and negative charges, then electron–ion recombination would occur, and the ^{3}He gas would return to its previous state. This process corresponds to the recombination region shown in the far left of Fig. 3.7.

Constructing a functioning detector requires creating an electric field within the gas volume to separate the positive and negative charge and employing some form of readout electrode or electrodes to collect the induced signal charge. Either planar or coaxial configurations can be used, and the resulting electric field is a function of the specific geometry and the strength of the applied potential.

Regardless of geometry, if the electric field strength is just sufficient to separate the initial electron–ion pairs, then the charge collected would be that of the primary ionization. This operating mode is in the ionization chamber region (the second region from the left in Fig. 3.7). Although the signal charge is rather small (typically ~ 4–5 fC), practical neutron detectors have been constructed which operate exceptionally well in ionization mode [7, 8].

In the proportional region (the center region in Fig. 3.7), the electric field strength is increased to the point at which additional ionizing collisions occur, resulting in a signal charge greater than, and proportional to, that of the primary ionization. Proportional mode is the operating regime of all ^{3}He gas-based neutron detectors at SNS and HFIR; therefore, it will be the focus of the remainder of this chapter.

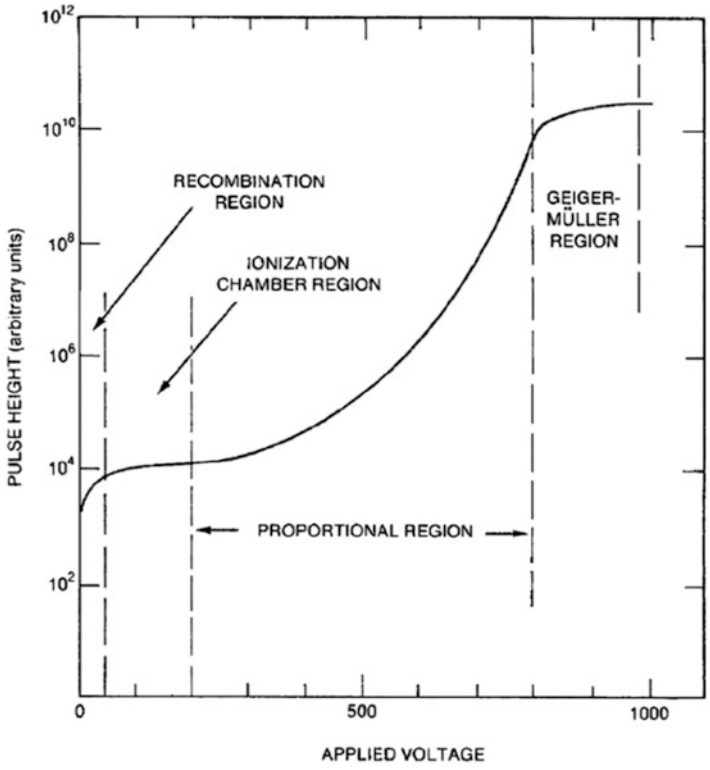

Fig. 3.7 Regions of operation for gas detectors [6]

3.1.3 Gas-Proportional Detectors

In ionization mode, an electric field is applied across the gas volume to separate the electrons from the ions in the primary ionization cloud. The signal charge is equal to that of the primary ionization.

In proportional mode, the electric field is increased to a level at which the primary ionization charges attain sufficient kinetic energy between scattering collisions to further ionize additional gas atoms as they drift toward the biased electrodes. This has the effect of increasing the signal charge beyond that of the primary ionization. This process is referred to as *impact ionization*, or *gas multiplication*. *Proportional mode* refers to the regime in which the multiplication charge remains proportional to the primary ionization charge.

Proportional detectors can have either planar or cylindrical geometry. In planar geometry, the electrodes form a parallel plate configuration, with constant electric field $E = V/d$ between the two electrodes, where V is the applied voltage, and d is the distance between electrodes. The typical configuration for cylindrical geometry is

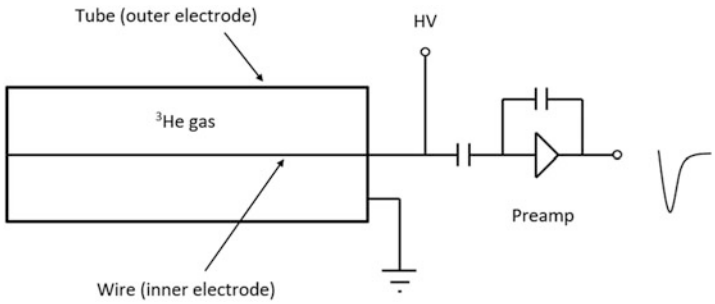

Fig. 3.8 Diagram of typical cylindrical gas-proportional tube

shown in Fig. 3.8. A cylindrical tube forms the outer electrode, and a coaxial wire along the tube center is the inner electrode.

The electric field in cylindrical (coaxial) geometry takes the form

$$E(r) = \frac{V}{r} \ln\left(\frac{b}{a}\right) \tag{3.6}$$

where V is the applied voltage across the electrodes, r is the radial distance from the center of the tube, and b and a are the distances to the outer and inner electrode surfaces, respectively. Specifically, b is the radial distance to the inside surface of the tube, and a is the radius of the wire.

The voltage to produce a given electric field is significantly higher for planar geometry than for cylindrical geometry. To give a realistic example for cylindrical geometry, let voltage $V = 1800$ V, $b = 1.25$ cm, and $a = 100$ μm. The electric field (plotted in Fig. 3.9) has a value just over 37,000 V/cm at the surface of the wire. To achieve the same field in a 2.5 cm thick (to give an equivalent gas depth) planar detector would require detector operation around 92,000 V, quite an unreasonable specification for a practical detector. For this reason, proportional detectors most often use cylindrical geometry.

Either the wire or the tube wall (or both) can be biased, but in practice, high voltage is usually applied to the central wire only while the tube wall is held at ground potential. The detectors at SNS and HFIR have this configuration, which is illustrated in Fig. 3.8. Electrons are much easier to accelerate than positive ions because of their smaller mass (proton-to-electron mass ratio is ~1836); therefore, most proportional detectors are designed to have the electrons drift into the higher electric field regions (i.e., toward the tube center). This design requires the central (anode) wire to be at positive high voltage.

The process of gas multiplication is illustrated in Fig. 3.10. A single electron drifting through a high electric field attains sufficient kinetic energy to ionize a neutral gas atom, resulting in a positively charged ion and two free electrons. The process repeats, yielding a final signal charge much larger than the initial ionization

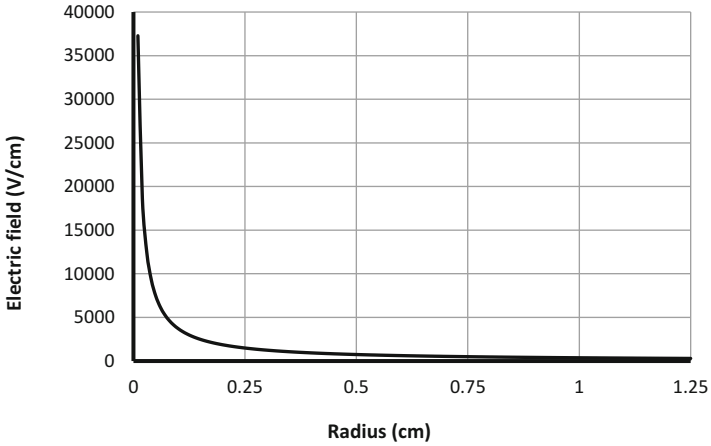

Fig. 3.9 Plot of electric field from Eq. (3.6), using the realistic example of $V = 1800$ V, $b = 1.25$ cm, and $a = 0.01$ cm. The $1/r$ dependence from Eq. (3.6) is clearly shown

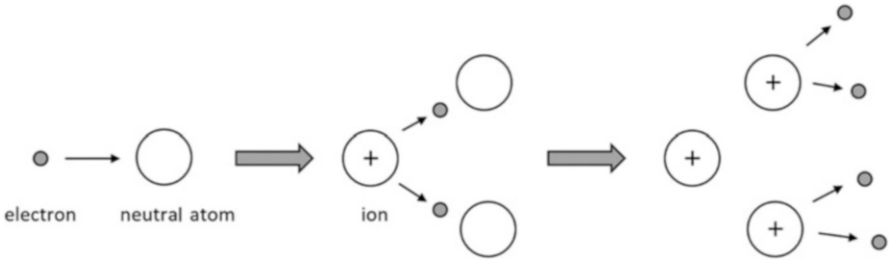

Fig. 3.10 Illustration of the process of charge multiplication in a gas. (*left*) A single electron impacts a neutral gas atom with sufficient energy to ionize it. (*center*) Both electrons (the original and the newly emitted one) are now available to ionize additional neutral gas atoms. (*right*) This process continues as long as the electric field is large enough to support impact ionization

charge. Gas multiplication factors on the order of 200-300 are common for the LPSDs.

The following presents a derivation for gas gain in coaxial geometry [9].

For electric fields above a critical value E_c (corresponding to critical radius r_c), electrons gain enough kinetic energy between scattering collisions to ionize additional gas atoms upon impact.

The fractional increase in the number of electrons created dn/n per unit path length dr is given by

$$\frac{dn}{n} = \alpha(r)dr \tag{3.7}$$

where $\alpha(r)$ is the first Townsend coefficient (number of electron–ion pairs created per unit length).

Integrating Eq. (3.7) from the anode wire radius a to the critical radius r_c (where the electric field no longer supports gas multiplication) yields Eq. (3.8):

$$\int \frac{dn}{n} = \ln\left|\frac{n}{n_0}\right| = \int_a^{r_c} \alpha(r)dr \tag{3.8}$$

where n_0 is the initial ionization charge, and n/n_0 is the gas multiplication factor, or gas gain M.

Because $(\partial r/\partial E) = [V/\ln|b/a|]\,(-1/E^2)$, changing the variable of integration from radius r to electric field E and using Eq. (3.6) for $E(r)$ gives Eq. (3.9):

$$\ln\left|\frac{n}{n_0}\right| = \ln|M| = \int \alpha(E)[\partial r/\partial E]dE = \frac{V}{\ln\left|\frac{b}{a}\right|}\int_{E(a)}^{E(r_c)} -\frac{\alpha(E)}{E^2}dE \tag{3.9}$$

The critical electric field where gas multiplication begins is given by Eq. (3.10):

$$E(r_c) = \frac{V}{r_c\ \ln\left|\frac{b}{a}\right|} \tag{3.10}$$

The electric field at the surface of the wire is given by Eq. (3.11):

$$E(a) = \frac{V}{a\ \ln\left|\frac{b}{a}\right|} \tag{3.11}$$

Removing the negative sign by changing the order of integration limits yields Eq. (3.12):

$$\ln|M| = \frac{V}{\ln\left|\frac{b}{a}\right|}\int_{E(r_c)}^{E(a)} \frac{\alpha(E)}{E^2}dE \tag{3.12}$$

At this point, the explicit form of $\alpha(E)$ must be determined as function of E.

If one assumes a linear proportionality $\alpha(E) = kE$ (first derived by Diethorn 1956 [10]) gives Eq. (3.13):

$$\ln|M| = \frac{Vk}{\ln\left|\frac{b}{a}\right|}\ln\left|\frac{E(a)}{E(r_c)}\right| \tag{3.13}$$

In this expression, $k = \ln 2/\Delta V$, where ΔV is the change in potential between two ionizing events.

Substituting Eqs. (3.10) and (3.11) into Eq. (3.13) gives Eq. (3.14):

$$\ln|M| = \frac{Vk}{\ln\left|\frac{b}{a}\right|}\ln\left|\frac{r_c}{a}\right| \tag{3.14}$$

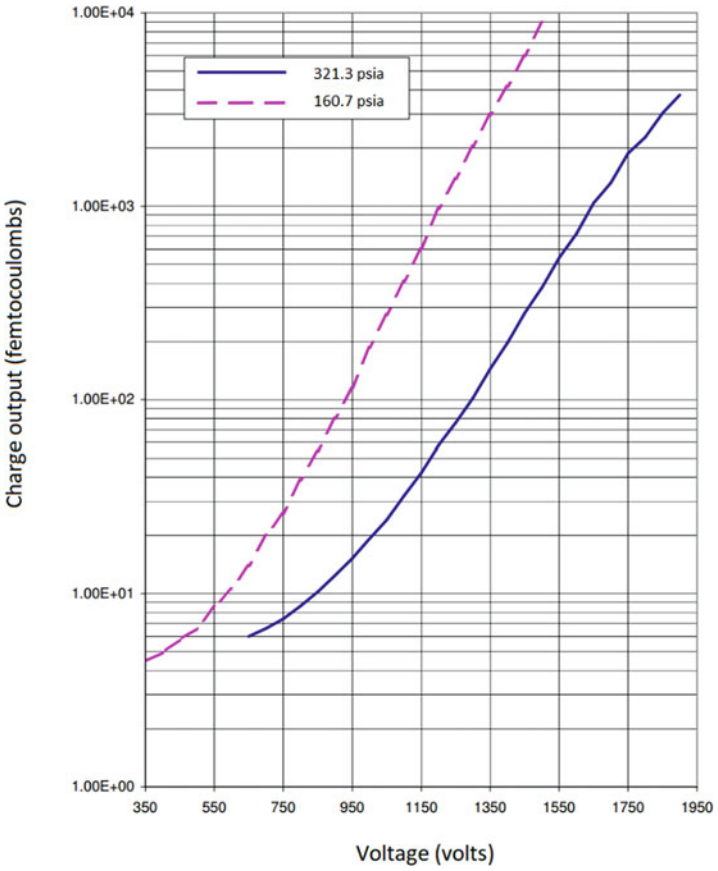

Fig. 3.11 Gas gain for two otherwise identical ^{3}He gas-proportional tubes at different gas pressures (The pressure corresponding to the dashed curve is 160.7 psia, and the pressure for the solid curve is 321.3 psia [11])

Solving for M gives Eq. (3.15):

$$M = \exp\left\{\frac{Vk}{\ln\left|\frac{b}{a}\right|}\ln\left|\frac{r_c}{a}\right|\right\} \tag{3.15}$$

Equation (3.15) suggests that gas gain M increases approximately exponentially with applied voltage. It is a function of the number of ionizing collisions and thus mean free path. Therefore, proportional tubes at higher gas pressures would be expected to require higher voltages to achieve a given gas gain, and this is found to be the case. Figure 3.11 is a plot of the gas gain for two tubes with the same dimensions and gas composition but at two different gas pressures. The gas pressure for the tube

represented by the solid curve is twice that for the tube represented by the dashed curve. A higher voltage is required for the higher-pressure tube to achieve the same charge output as the lower pressure tube.

From the Shockley–Ramo theorem [12, 13], the induced charge and induced current on a conductor (e.g., anode wire) owing to a charge carrier can be determined by postulating a weighting potential V_{W} and weighting field $\boldsymbol{E}_{\mathbf{W}}$ based on the following three criteria. (1) The charge carrier is assumed to be absent. (2) The potential on the conductor of interest is defined to be 1. (3) The potential on all other conductors is zero. The induced charge q_{ind} is a product of the actual charge of the charge carrier and the value of the weighting potential at the location of the charge carrier. The induced current i_{ind} is the product of the actual charge of the charge carrier, and the inner (or dot) product of the vector velocity of the charge carrier and the vector value of the weighting field at the charge carrier location. The expressions for induced charge and induced current are given by Eqs. (3.16) and (3.17), respectively.

$$q_{\mathrm{ind}} = qV_{\mathrm{W}} \tag{3.16}$$

$$i_{\mathrm{ind}} = q\boldsymbol{v} \cdot \boldsymbol{E}_{\mathbf{W}} \tag{3.17}$$

The weighting potential in cylindrical geometry is given by Eq. (3.18) [14]:

$$V_{\mathrm{W}}(r) = \frac{\ln\left|\frac{r}{r_2}\right|}{\ln\left|\frac{r_1}{r_2}\right|} \tag{3.18}$$

where r is once again the radial distance from the tube center, r_1 is the inner electrode radius (previously a), and r_2 the outer electrode radius (previously b).

Weighting potential $V_{\mathrm{W}}(r)$ is plotted in Fig. 3.12 for various values of the expression $(r - r_1)/(r_2 - r_1)$, which ranges from the anode wire radius r_1 (0 in the plot) to the tube radius r_2 (1 in the plot).

Inspecting Fig. 3.12 reveals that the weighting potential is largest at $r = r_1$, thus most of the induced signal charge results from charges moving very near the surface of the anode wire.

Neutron pulses from cylindrical ^{3}He gas proportional detectors can take on a variety of shapes. Figure 3.13 shows three representative examples of preamplifier output pulses, all from the same detector tube and the same operating conditions. In addition to the more familiar unipolar pulse shape (leftmost image in the figure), pulses can also have a two-lobed form (middle and right images), with the amplitude of the first lobe either greater or less than that of the second lobe. Leading edge risetimes can also vary somewhat between different pulses. It is conceivable, though entirely unsubstantiated, that these pulse shape variations reflect the difference in arrival times of the charge clouds due to the proton and triton, depending on the orientation of their trajectories relative to the anode wire.

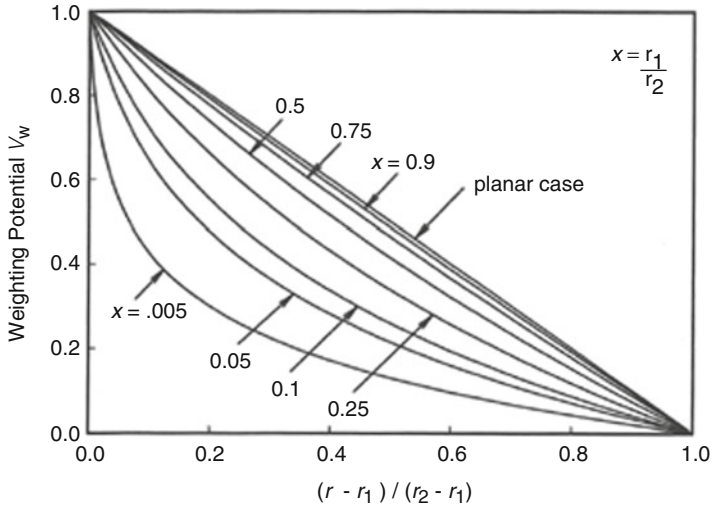

Fig. 3.12 Weighting potentials for various values of r_1/r_2 versus the normalized distance from r_1 to r_2 for a cylindrical detector [14]

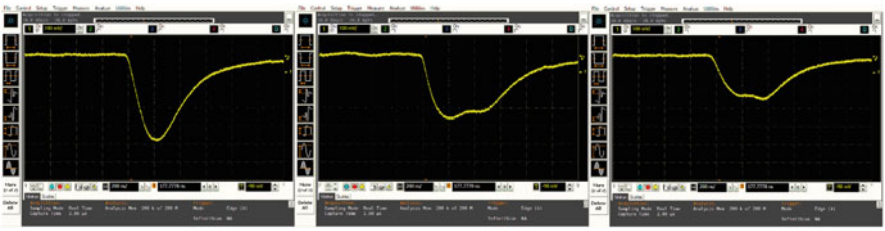

Fig. 3.13 Oscilloscope traces of typical neutron pulses from a ^{3}He proportional tube. The vertical scale is 100 mV per division and the horizontal scale is 200 ns per division for all

3.2 Linear Position–Sensitive Detectors

3.2.1 General Description

3.2.1.1 Introduction

A LPSD is a gas-filled tube with a resistive central wire stretched along its axis. It is biased to operate in proportional mode—the charge introduced to the gas by radiation absorption causes a several-fold larger charge pulse to travel from the tube wall to the central wire. The charge in the pulse is measured at both sides of the wire. Because of the resistance of the wire, the charge fraction that appears at each end varies depending on the position along the wire where the charge deposition occurs.

A detector's sensitivity to neutrons requires introduction of an isotope that can absorb a neutron (n) and then emit energetic charged particles. The most common choice is ^{3}He, which undergoes the reaction n + ^{3}He → ^{3}H + p + 0.764 MeV. Helium-3 can exist in the detector as the primary component of the fill gas. An alternative is ^{10}B, which could be introduced as a gas such as BF_3 or as a thin film of boron inside the detector.

The detector tube operates with the central wire positively charged with respect to the tube wall. The energetic charged particles emitted by the neutron absorption are emitted in opposite directions, creating ionization trails in the detector gas. The released electrons are attracted to the central wire, and the ions are attracted to the tube wall. The electrons gain energy from the electric field between collisions with the detector gas, and, for a high enough field, this energy is enough to cause additional ionization of the detector gas. The electric field increases near the central wire, and it eventually becomes high enough for this additional ionization to occur, creating a region of charge multiplication near the wire, which increases the number of electrons reaching the wire by some factor. Positive ions are left behind, and they drift to the tube wall at a slower rate. These reactions are illustrated in Fig. 3.14.

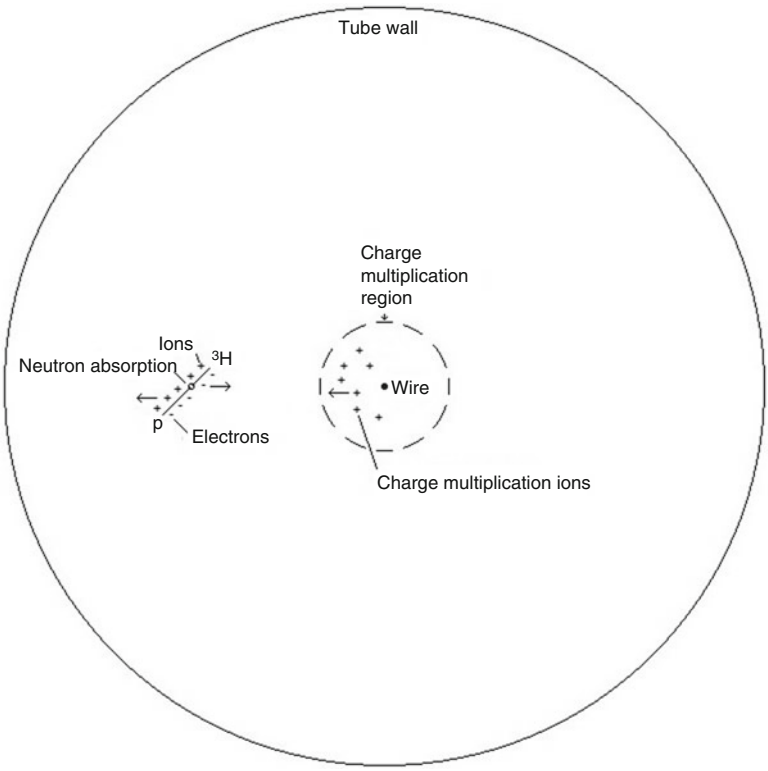

Fig. 3.14 Events associated with neutron detection

There is a space charge from the positive ions, which limits the extent to which the electrons deposited on the wire can exit along the wire. As discussed in Sect. 3.1.2, this effect is strongest when the ions are near the wire, and it diminishes as the ions drift away from the wire. The ions influence the rate at which the charge from an event is released along the wire, but most of the charge will be released before the ions drift all the way to the tube wall.

3.2.1.2 Detector Tube Construction

Because of the detector tube's cylindrical geometry, the electric field inside the tube is inversely proportional to the distance from the center of the central wire. The rate of secondary ionization is highly sensitive to the electric field strength. Therefore, secondary ionization primarily occurs near the central wire. For a given bias, a small-diameter wire has a higher electric field at its surface than a large-diameter wire. This higher electric field allows for a higher amount of charge multiplication, which allows the small-diameter wire to achieve a desired rate of charge multiplication at a smaller bias voltage. The smaller-diameter wire also has more margin between its operating point and the bias at which electrical breakdowns occur. For these reasons, a very small diameter is chosen for the central wire, typically approximately 50 μm.

Figure 3.15 shows some details of how an end of an LPSD tube is constructed. A central electrode passes through and is sealed to a surrounding length of insulating material, which is typically alumina. Near the center of this insulator's length, its outer surface is sealed to some form of metallic ring, upon which the feedthrough is mounted. Because this feedthrough must hold off high voltages, the insulator extends beyond the outer mounting ring on both sides by approximately a centimeter, typically. The feedthrough is mounted to a machined metallic mounting piece, which also connects to the tube that forms the detector's outer wall. Typically, the tube forming the outer wall is welded to the mounting piece. In many cases, this mounting piece includes additional features to create attachment points between the detector tube and the detector module.

A metallic shielding tube is attached to the feedthrough electrode on the end that is inside the detector. One end of a tiny coil spring inside the shielding tube is attached to the shielding tube and suspended near the center line. The other end is attached to the center wire that runs along the length of the detector tube. The spring

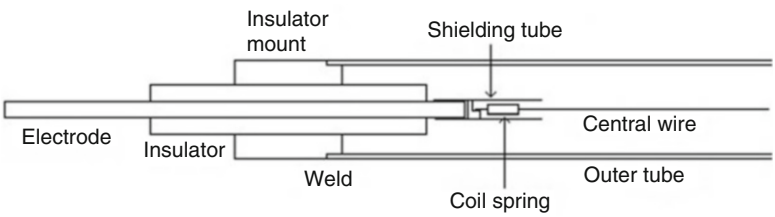

Fig. 3.15 Structure of an LPSD tube

maintains the tension on the central wire. The shielding tube is also used to create a well-defined distance, along which the central wire is exposed to the full biasing electric field of the detector. At this distance, the wire becomes active for neutron detection.

At least one of the central electrodes of the feedthroughs is a tube, which creates a passage for evacuating the detector tube and backfilling it with the detector gas. After the filling is complete, this tube is pinched off to create a seal.

Aluminum and stainless steel are the most common material choices for the tube that forms the detector's outer wall. The choice of aluminum is motivated by its low tendency to absorb or scatter neutrons. Aluminum tubes bend under modest loads. They can easily be strained beyond their elastic limit, beyond which the bend does not spring back. Aluminum also tends to form a poorly conductive surface layer, which can hinder achieving solid ground connections. Stainless steel tubes have a greater resistance to bending than aluminum tubes. Stainless steel's threshold for inelastic bending is also much higher that aluminum's, so most deflections that occur tend to spring back. Stainless steel is less likely than aluminum to form a resistive surface layer. It absorbs neutrons somewhat more strongly than aluminum. Stainless steel's better mechanical properties allow tubes to be built with a thinner wall than is needed for aluminum, thereby compensating for the higher absorption.

The fill gas pressure is often dictated by the range of neutron wavelengths the detector must manage. Helium-3 has a 5330 barn neutron absorption cross section for thermal neutrons. It is a $1/v$ absorber, which makes its cross section proportional to the wavelength. Thermal neutrons have a 1.8 Å average wavelength, so the cross section for wavelength λ is $\sigma = \lambda\sigma_0$, where $\sigma_0 = 5330$ barn/1.8 Å $= 2.961 \times 10^{-24}$ cm^2/Å. A neutron beam of intensity I and wavelength λ traveling through a region with ^{3}He atom density N will have a loss of intensity over a travel distance dL of $dI = -\sigma_0\lambda N dL$. After traversing a total distance L, a beam of original intensity I_0 will have intensity $I = I_0\exp\{-\sigma\lambda NL\}$. The fraction of the beam that is absorbed into the gas, causing potentially detectable reactions, is given by Eq. (3.19).

$$f = \frac{I_0 - I}{I_0} = 1 - \exp\{-\sigma_0\lambda NL\} \tag{3.19}$$

The value of f decreases as $\sigma_0\lambda NL$ increases, with $f = 0.63$ for $\sigma_0\lambda NL = 1$. If that is taken as the minimum acceptable efficiency, the efficiency is acceptable for all $\lambda > 1/(\sigma_0 NL)$. The maximum value of L is the inner diameter of the detector tube—even less for neutrons that enter the tube offset from the central axis. The value of N is proportional to the gas pressure given by the gas law $N = P/(k_B T)$, where P is the ^{3}He partial pressure, T is the temperature, and k_B is the Boltzmann constant (1.38×10^{-23} J/K). Typically, the chosen fill gas pressure is a few atmospheres. The mean free path for electrons in the gas decreases as the pressure increases, which increases the bias voltage required to obtain a desired gas gain.

If a neutron that has a high wavelength (compared with the wavelength at which the efficiency drops off) enters the detector, then that neutron is likely to interact very soon after it enters the detector. A neutron whose wavelength is comparable to the

drop off wavelength is likely to penetrate more deeply. This effect may result in some wavelength dependence on the amount of charge collected. If the neutron's trajectory is not perpendicular to the tube, the penetration depth may also influence the position determination.

3.2.1.3 Pulse-Height Spectrum

Figure 3.16 is a pulse-height spectrum from a ^{3}He-filled LPSD. The horizontal axis is the amount of charge collected from the central wire of the LPSD owing to a detection event. The charge range for which the detector is configured is divided into 1024 bins. The vertical axis is the number of events that are detected in each bin during an acquisition. For the acquisition in Fig. 3.16, the maximum charge observed in the pulse height spectrum is approximately 1 pC. This maximum charge is sensitive to the bias, gas pressure, and geometry of an LPSD tube. Under conditions in which the detector works well, it is often in the 1–2 pC range. The nuclear reaction by which a neutron is detected always occurs with the same energy, independent of the neutron wavelength. The pulse-height spectrum reveals a considerable variation in the amount of charge collected from such events. In the 0.8–1.0 pC region in the figure, the intensity drops off to zero moderately rapidly after the primary peak.

In the 0.2–0.8 pC region, a more gradual intensity drop-off occurs before the central peak. Two secondary peaks appear in this region. These secondary peaks are caused by the wall effect, in which one of the charged particles emitted from the

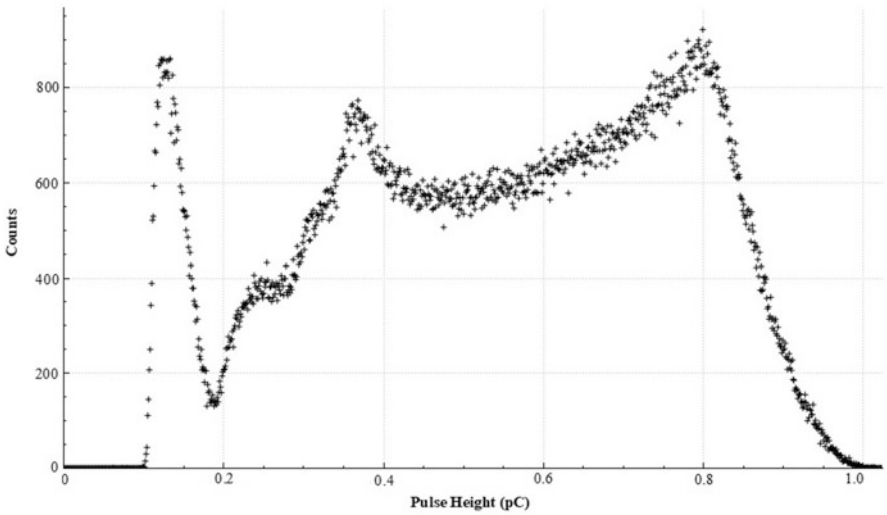

Fig. 3.16 Pulse-height spectrum. The horizontal axis is the charge collected during a detection event. The charge range for which the detector is configured is divided into 1024 bins. The vertical axis is the number of events detected within each bin

reaction strikes the tube wall and is absorbed before its kinetic energy is fully used to ionize the gas. The gradual drop-off is partly caused by the tube geometry. An event near the tube wall is in a region where the electric field is low, the ion drift distance is low, and the electron drift distance is high. An event near the wire is in a region where the electric field is high, the ion drift distance is high, and the electron drift distance is low. These differences because of the position of an event can influence the probability that electrons and ions will recombine before being collected. They might influence the amount of charge multiplication that occurs. They will influence the drift time required for the ions to reach the tube wall and for the electrons to reach the tube wire. In some cases, the drift time may exceed the integration time for the detector pulse. This excess time can cause pulse height spectrums obtained using short integration times to have less clearly defined peaks than pulse-height spectrums obtained with long integration times. The spectrum in Fig. 3.16 used a short 750 ns integration time, chosen to optimize other aspects of detector performance.

In the 0.12–0.20 pC region, the intensity increases. Gamma ray detections occur in this region. The lack of counts in the 0.0–0.1 pC region is an artifact of the discriminator settings. Otherwise, gamma rays and electronic noise would also appear in this region. The energy released from the nuclear reaction is high enough that the charge released from a neutron absorption is considerably higher than the charge released from a gamma ray interaction with the detector. Therefore, it is straightforward to establish discriminator settings that strongly reject gamma ray events while still accepting most of the neutron events. A small portion of the pulse-height spectrum from neutrons does extend into the region where gamma ray rejection is required, so a few percent of neutrons that have a reaction in the tube will still be rejected.

The charge multiplication in the detector tube is sensitive to the bias voltage. Typically, the range of the pulse-height spectrum doubles after a 100 V increase in the bias voltage. Both gamma ray– and neutron-sensitive fractions of the pulse-height spectrum range tend to increase when a higher bias voltage is used.

3.2.1.4 Count-Rate Effects

Count-rate limitations for LPSDs can be difficult to characterize because the performance does not decline abruptly. A dead time of approximately a microsecond occurs while the charge from an event is being integrated. High rates increase the probability that the charge from a second event will arrive while the charge from the first event is being integrated, resulting in an incorrect position determination. A small amount of the charge from an event arrives after the end of the integration interval. If a second event is integrated while this residual charge is arriving, then the position determination is skewed. The increased levels of ionization in the tube at high rates can reduce the amount of charge multiplication. The decreased amount of charge collected degrades the position resolution and increases the fraction of events that are vetoed. These effects are of minimal importance at rates of 10,000 counts per second, but these effects increase gradually at higher rates.

3.2.1.5 Circuitry for Position Determination

First, the charge-division principle for determining the position of a neutron detection along a detector tube is derived for an idealized case that ignores error sources. Figure 3.17 shows a simplified diagram of the circuitry used for position determination. Here, the detector tube is assumed to have a central wire of resistance R and length L. At some time t after a detection event, a current I_0 is deposited on the wire at a distance D from side one. The portion of the wire on side one from the deposition location has resistance $R_1 = RD/L$, whereas the portion on side 2 has resistance $R_2 = R(L - D)/L$. A current-to-voltage amplifier that—in the ideal case—maintains its negative input at ground potential is located on each side of the tube. Therefore, the current I_0 conducts to ground through resistances R_1 and R_2 in parallel, raising the voltage at the deposition location by $V_0 = (I_0R_1R_2)/(R_1 + R_2)$. Therefore, currents

$$I_1 = \frac{I_0R_2}{R_1 + R_2} = \frac{I_0(L-D)}{L} \tag{3.20}$$

and

$$I_2 = \frac{I_0R_1}{R_1 + R_2} = \frac{I_0D}{L} \tag{3.21}$$

go to the amplifiers, creating voltages

$$V_{A1} = \frac{I_0R_{f1}(L-D)}{L} \tag{3.22}$$

and

$$V_{A2} = \frac{I_0R_{f2}D}{L} \tag{3.23}$$

at their outputs. These voltages go to integrators, which have time constants τ_1 and τ_2 such that $(dV_{I1}/dt) = (V_{A1}/\tau_1)$ and $(dV_{I2}/dt) = (V_{A2}/\tau_2)$. If the total charge Q from the detection event is assumed to be delivered between times $t = 0$ and $t = t_m$, $Q = \int_0^{t_m} I_0 dt$. If $V_{I1} = V_{I2} = 0$ at $t = 0$, then at $t = t_m$,

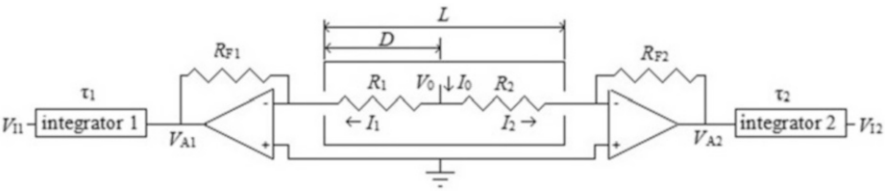

Fig. 3.17 Simplified diagram of position-measuring circuit

$$V_{I1} = \frac{R_{f1}(L-D)}{\tau_1 L}\int_0^{t_m} I_0 dt = \frac{R_{f1}(L-D)Q}{\tau_1 L} \tag{3.24}$$

and

$$V_{I2} = \frac{R_{f2}D}{\tau_2 L}\int_0^{t_m} I_0 dt = \frac{R_{f2}DQ}{\tau_2 L} \tag{3.25}$$

For matched gains where $(R_{f1}/\tau_1) = (R_{f2}/\tau_2)$,

$$D = \frac{LV_{I2}}{V_{I1} + V_{I2}} \tag{3.26}$$

and

$$Q = \frac{\tau_1(V_{I1} + V_{I2})}{R_{f1}} \tag{3.27}$$

A complete circuit for handling LPSD detection events must handle many details not included in the simplified diagram of Fig. 3.17. A more complete but still simplified diagram is shown in Figs. 3.18 and 3.19. These figures are based on a design used for LPSDs at SNS. Figure 3.18 has circuits for the preamplifier boards, along with their connection to the detector tube. These amplify the weak high-impedance signal from the detector tube to a larger, low-impedance signal. These boards are mounted to the detector within shielded enclosures with short, shielded connections to the tube ends. The preamplifier output is transmitted as a low-voltage differential signal (LVDS) over a cable to the rest of the signal processing circuits located on a board called the readout circuit (ROC). These circuits are diagrammed in Fig. 3.19.

One feature shown in Fig. 3.18 is the means for applying bias to the detector wire. Components R_{fill1}, C_{F1}, R_{fill2}, and C_{F2} form a pair of cascaded low pass filters, which are intended to reduce ripple in the voltage V_{bias} coming from the high-voltage power supply. The ripple can be a significant source of noise introduced to the detector. R_B is the resistor that restores the charge lost from the wire when a detection event occurs. These features are only needed for one side of the wire. Both sides need the capacitors C_{S1} and C_{S2}, which block the steady bias voltage on the tube wire while passing the rapid fluctuations caused by a detection event. Typical values used are $R_{\text{fil1}} = R_{\text{fil2}} = R_B = 2$ MΩ, $C_{F1} = C_{F2} = 8.5$ nF, and $C_{S1} = C_{S2} = 15$ nF.

Additional resistances, R_{P1} and R_{P2}, are often in the path from the detector wire to the current to voltage amplifier. These resistances are part of transient protection circuits for the amplifier with values in the 10–100 Ω range. The current pulses from neutron detections tend to have durations in the 500 ns to 1 μs range, so the impedance of capacitors C_{S1} and C_{S2} at 1 MHz should be a reasonable estimate of their influence on such pulses. At 15 nF, this influence is approximately10 Ω. A real-world current-to-voltage amplifier also exhibits some impedance between its

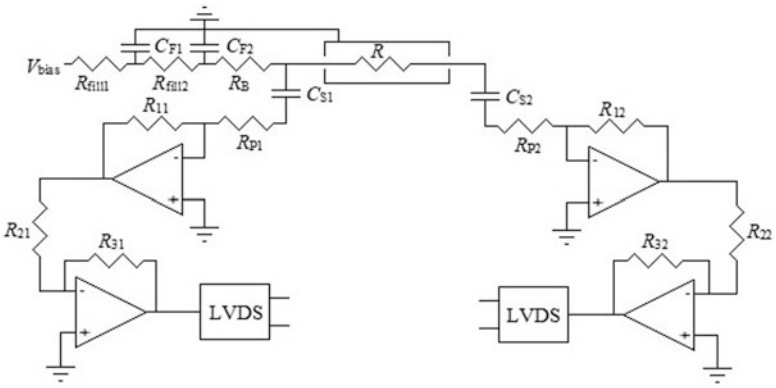

Fig. 3.18 Bias circuit for the detector wire and preamplifier stages

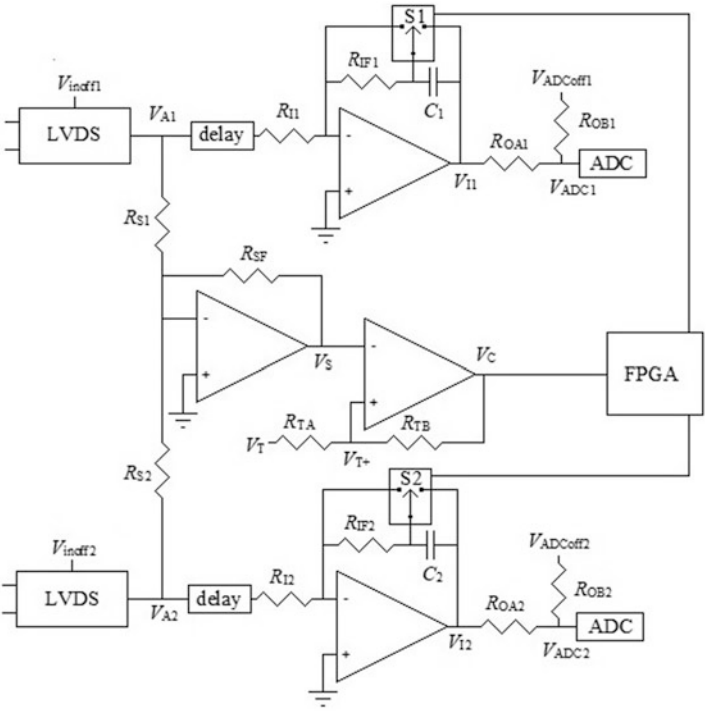

Fig. 3.19 ROC board components of position-measuring circuit

negative input and its ground. All these effects influence the charge-division position calculations, causing the calculated position along the wire to be displaced toward the tube center away from the actual position. Because uncertainties exist both in the magnitude of some of these impedances and in the mounting details of the detector

wire, correcting for this error empirically is best. Neutrons can be supplied to the detector at several known positions along the tube, and the ratio between the known and the calculated displacements can be used to determine a correction factor.

Figure 3.18 also has a more complete depiction of the preamplifier stages. Two stages of amplification are seen. These stages are followed by a conversion of the single-ended signal to LVDS for transmission to the next board. As far as gain is concerned, R_{F1} and R_{F2} in Fig. 3.17 actually mean $R_{F1} = (R_{11}R_{31}G_{L1})/R_{21}$ and $R_{F2} = (R_{12}R_{32}G_{L2})/R_{22}$. G_{L1} and G_{L2} are the gains associated with the conversion to LVDS. R_F should be high enough to use as much of the voltage range of the preamplifier second stage as possible without causing preamplifier saturation for the strongest pulses. The desired value can vary owing to detector characteristics and operating conditions, but common values of R_F are in the 70–150 kΩ range.

The ROC board signal processing in Fig. 3.19 begins with two convertors from LVDS to single-ended signals, one for each side of the tube. These convertors also have a provision for applying offset voltages V_{inoff1} and V_{inoff2} to compensate for any offset voltages that may be present in the preamplifier. The output of these convertors corresponds to the voltages V_{A1} and V_{A2} in Fig. 3.17. For these voltages to be integrated at the correct time, some form of discriminator circuit must exist to determine if an event is occurring. One scheme is to look for times when the current to the tube wire exceeds some threshold. Owing to the charge division, this scheme is equivalent to determining when $V_{A1} + V_{A2}$ exceeds some threshold. From Fig. 3.19, if $R_{S1} = R_{S2} = R_S$, then

$$V_S = R_{SF}\left(\frac{V_{A1}}{R_{S1}} + \frac{V_{A2}}{R_{S2}}\right) = \frac{R_{SF}}{R_S}(V_{A1} + V_{A2}) \tag{3.28}$$

The circuit after V_S is a comparator, for which $V_C = V_{CH}$ when it is saturated high, and $V_C = V_{CL}$ when it is saturated low. Initially, $V_C = V_{CH}$, yielding Eq. (3.29):

$$V_{T+} = V_T + (V_{CH} - V_T)\frac{R_{TA}}{R_{TA} + R_{TB}} = \frac{V_T R_{TB}}{R_{TA} + R_{TB}} + \frac{V_{CH} R_{TA}}{R_{TA} + R_{TB}} \tag{3.29}$$

When V_S is greater than V_{T+}, V_C decreases from V_{CH} to V_{CL}, causing V_{T+} to decrease to V_{T-}, as calculated using Eq. (3.30):

$$V_{T-} = \frac{V_T R_{TB}}{R_{TA} + R_{TB}} + \frac{V_{CL} R_{TA}}{R_{TA} + R_{TB}} \tag{3.30}$$

The change in V_T is given by Eq. (3.31):

$$V_{T+} - V_{T-} = (V_{CH} - V_{CL})\frac{R_{TA}}{R_{TA} + R_{TB}} \tag{3.31}$$

This decrease in V_{T+} creates a hysteresis, which reduces the chance that the comparator will fire multiple times on a single pulse. For typical values of $V_{CH} = 3.3$ V, $V_{CL} = 0$ V, $R_{TA} = 1000\ \Omega$, and $R_{TB} = 330$ KΩ, the hysteresis is 0.01 V.

By the time the comparator responds, a large portion of the pulse from the detector has already occurred. For the entire pulse to be integrated, its arrival to the integrator must be delayed. This delay is the purpose of the delay lines shown in Fig. 3.19. The delay time is set at 200 ns.

The integrators are gated by the complementary metal–oxide–semiconductor (CMOS) switches, which appear as components S1 and S2 in Fig. 3.19. When the integrators are off, the capacitors C_1 and C_2 are shorted to have zero charge, and resistors R_{IF1} and R_{IF2} provide feedback. Thus, the integrator behaves as an amplifier with gain less than 1. When the integrators are on, resistors R_{IF1} and R_{IF2} are shorted, and capacitors C_1 and C_2 provide feedback. The integrators integrate the delayed voltages V_{A1} and V_{A2} with time constants $\tau_1 = R_{I1}C_1$ and $\tau_2 = R_{I2}C_2$, generating outputs V_{I1} and V_{I2}, which correspond to the voltages of the same name in Fig. 3.17. The outputs are read by analog to digital convertors (ADCs), which cover a range from 0 V on the low end to a high end that ranges from 1 to 2 V depending on the configuration. The time constant should be chosen so that it is high enough for the integrated pulses to use most of the ADC range but not so high that the strongest integrated pulses exceed the ADC range. On the SNS ROC boards, $\tau = 2.2 \times 10^{-7}$ s is used.

When integrating with no signal, which is sometimes required for calibrations, noise can sometimes cause V_{I1} to be negative, which is outside of the ADC range, forcing the reading to be inaccurately reported or vetoed. In either case, the result is an inaccurate determination of the average value of V_{I1}. To avoid this issue, resistors R_{OA1} and R_{OB1} are added to provide a voltage offset, as shown in Eq. (3.32).

$$V_{\mathrm{ADC1}} = V_{I1} + (V_{\mathrm{ADCoff1}} - V_{I1})\frac{R_{OA1}}{R_{OA1} + R_{OB1}} = \frac{V_{I1}R_{OB1}}{R_{OA1} + R_{OB1}} + \frac{V_{\mathrm{ADCoff1}}R_{OA1}}{R_{OA1} + R_{OB1}} \tag{3.32}$$

For typical values of $R_{OA1} = 50\ \Omega$ and $R_{OB1} = 1000\ \Omega$, 95% of V_{I1} is passed to V_{ADC1}, and the offset is 5% of V_{ADCoff1}. The offset circuit for the second integrator works the same way.

A field-programmable gate array (FPGA) on the board handles all digital logic activities. It monitors the comparator output and times the gating of the integrators. The FPGA captures the ADC outputs at the desired times during the integration, and it loads values into digital to analog converters (DACs), which supply voltages such as V_{inoff1}, V_{inoff2}, V_{ADCoff1}, V_{ADCoff2}, and V_T. It controls communications with other components of the data acquisition system, and it can read the time from the last synchronizing trigger for a detected event. Depending on the acquisition mode, the FPGA either returns the raw ADC readings and time for an event, or it can calculate the position and return a position and time.

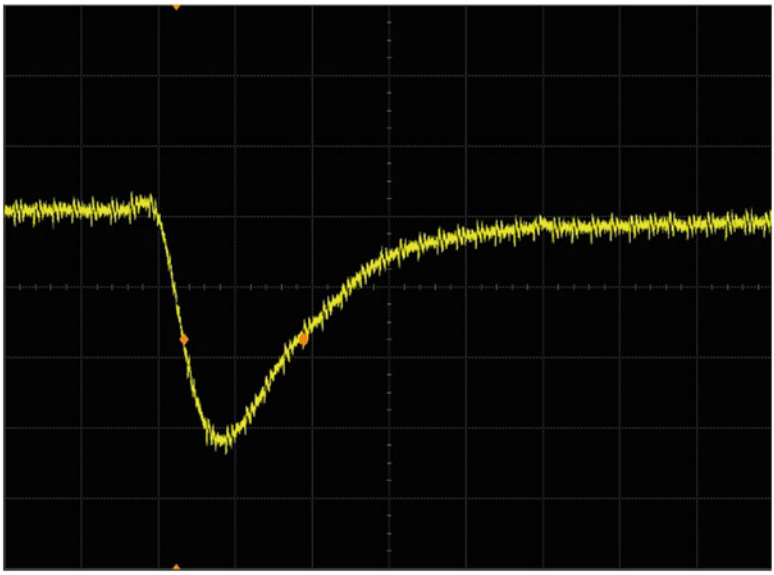

Fig. 3.20 Typical pulse shape from neutron detection by an LPSD tube, measured at point corresponding to V_{A1} in Fig. 3.19. 200 mV/division with 200 ns/division sweep rate

Figure 3.20 shows an oscilloscope trace for a typical pulse from an LPSD tube for a neutron detection. It was measured at the point corresponding to V_{A1} in Fig. 3.19 after being amplified by the preamplifier. Figure 3.21 shows an oscilloscope trace for a typical gated integrator output from a neutron detection. It was measured at a point corresponding to V_{I1} in Fig. 3.19.

The shape of the pulse from the detector tube can vary between detection events. Therefore, a range in the amount of delivered charge Q corresponds to the discriminator cutoff. If Q is the basis for discrimination, then the discriminator settings must be low enough to admit most events with the minimum desired Q. The ADC readings after the integration can then be examined to veto events with less than the desired Q. Notably, the vetoed events still contribute to the dead time of the detector.

3.2.1.6 Correction for Voltage Offset Errors in Position Determination

One source of error in the position determination is a voltage offset in an amplifier. Referring to Fig. 3.17, assume the following in Eq. 3.33:

$$V_{A1} = V_{A1\text{off}} + \frac{I_0 R_f (L - D)}{L} \tag{3.33}$$

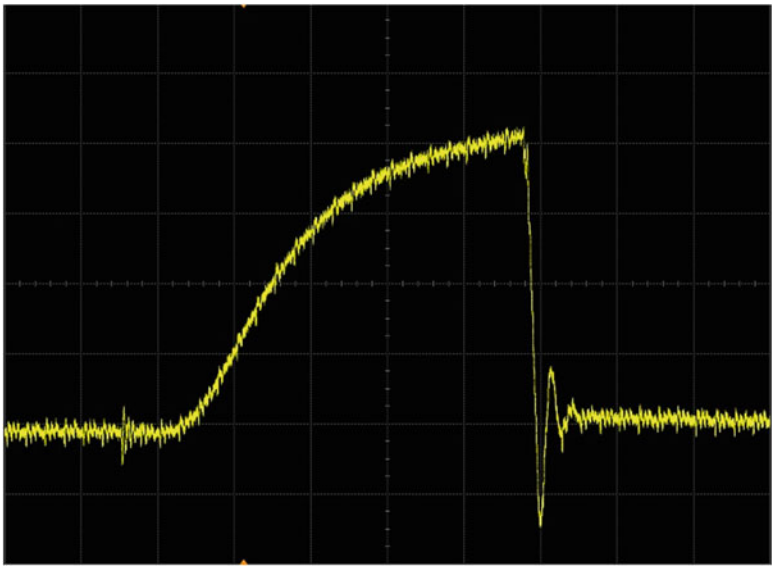

Fig. 3.21 Typical gated integrator output from a neutron detection, measured at a point corresponding to V_{I1} in Fig. 3.19. 200 mV/division with 200 ns/division sweep rate

For this calculation, assume that $\tau_1 = \tau_2 = \tau$ and $R_{F1} = R_{F2} = R_F$, ignoring gain differences. After integrating a detection event, the output of integrator 1 is given by Eq. (3.34):

$$V_{I1\text{off}} = \int_0^{t_m} \frac{V_{A1\text{off}}}{\tau} dt + \frac{R_f(L-D)}{\tau L} \int_0^{t_m} I_0 dt = \frac{t_m V_{A1\text{off}}}{\tau} + \frac{R_f(L-D)Q}{\tau L} \tag{3.34}$$

A position calculation using this value gives Eq. (3.35):

$$\begin{aligned} D_{\text{off}} &= \frac{LV_{I2}}{V_{I1\text{off}} + V_{I2}} \\ &= \frac{L\dfrac{R_f DQ}{\tau L}}{\dfrac{t_m V_{A1\text{off}}}{\tau} + \dfrac{R_f(L-D)Q}{\tau L} + \dfrac{R_f DQ}{\tau L}} \\ &= \frac{R_f DQ}{t_m V_{A1\text{off}} + R_f Q} \\ &= \frac{D}{B+1} \end{aligned} \tag{3.35}$$

where $B = (t_m V_{A1\text{off}})/(R_f Q)$.

B can be interpreted as the error in determining the delivered charge on side 1 because of the offset voltage divided by the total charge from the event. The error in the position determination is determined by Eq. (3.36):

$$\Delta D = D_{\text{off}} - D = \frac{-BD}{B+1} \tag{3.36}$$

The error is seen to be position-dependent, rising linearly from 0 on the side with the voltage offset to the maximum value on the other side. ΔD is also inversely proportional to the delivered charge Q from the event.

The position-measuring circuit contains adjustment provisions for canceling out voltage offsets. The value of the offset correction can be measured by integrations at times when no current owing to detection events is present. If the offset correction has the correct value, the output from the integrator at the end of an integration will be the same as it was at the start of the integration. Because of noise that is present in the detector, the results from many integrations must be averaged to measure the change reliably. In practice, a series of stepwise changes to the offset correction are tried until a value is found that minimizes the difference between the starting and ending integrator outputs, but a small difference will remain owing to the finite size of the DAC steps. This difference can be canceled out by using an alternate correction technique. The offset dependent term in Eq. (3.34), $(t_m V_{A1\text{off}})/\tau$, is independent of the size of the pulse being detected. If $V_{I1\text{off}0}$ is the measured value of $V_{I1\text{off}}$ for integrations when no current owing to detection events is present, then a measurement of a pulse, which has an integrator 1 output of $V_{I1\text{off}}$, will have an offset corrected value of $V_{I1} = V_{I1\text{off}} - V_{I1\text{off}0}$. This correction can be included as part of the position calculation.

The type of coupling between amplifier stages has implications for offset corrections. Although direct coupling between stages can minimize frequency-dependent effects in signal transmission, it has the drawback that temperature -dependent drifts in the offset of the first stage of the amplifier are multiplied by the full amplifier gain. This multiplication causes the offset correction to be strongly temperature -dependent, so a calibration to update the offset corrections must be repeated after a change in the detector temperature of only a few degrees. Capacitive coupling between stages creates high-pass filters, which block offsets from earlier stages. This blocking greatly reduces the temperature sensitivity. Pulse widths for detection events are typically a microsecond or less. Care must be taken to ensure that the time constant of the filter formed by a coupling capacitor interacting with the input impedance of the next stage is substantially longer than a microsecond.

3.2.1.7 Correction for Mismatched Gain Errors in Position Determination

Another source of error in the position determination is mismatched gains between the amplifiers or integrators on each side of the tube. In this case, $(R_{f1}/\tau_1) \neq (R_{f2}/\tau_2)$.

Given a gain mismatch A such that $(R_{f1}/\tau_1) = A(R_{f2}/\tau_2)$, then a position calculation, which is not corrected for the gain mismatch, gives the result in Eq. (3.37):

$$\begin{aligned} D_A &= \frac{LV_{I2}}{V_{I1}+V_{I2}} \\ &= \frac{\dfrac{LR_{f2}DQ}{\tau_2 L}}{\dfrac{R_{f1}(L-D)Q}{\tau_1 L}+\dfrac{R_{f2}DQ}{\tau_2 L}} \\ &= \frac{LD}{\dfrac{R_{f1}\tau_2}{R_{f2}\tau_1}(L-D)+D} \\ &= \frac{LD}{A(L-D)+D} \\ &= \frac{LD}{AL+(1-A)D} \end{aligned} \tag{3.37}$$

D_A differs from the actual position by Eq. (3.38):

$$\begin{aligned} \Delta D &= D_A - D = D\left(\frac{L}{AL+(1-A)D}-1\right) \\ &= D\left(\frac{(1-A)L-(1-A)D}{AL+(1-A)D}\right) \\ &= \frac{(1-A)D(L-D)}{LA+(1-A)D} \end{aligned} \tag{3.38}$$

The numerator is a parabola with a maximum value of $([1-A]L^2)/4$ at the center of the tube and 0 at the tube ends. The denominator varies linearly from AL at side 1 of the tube to L at side 2. Most cases of interest have small differences in gain where A is close to 1, so to a good approximation, the denominator can be assigned the value L everywhere. This approximation gives $\Delta D = ([1-A]L)/4$ near the center of the tube, or Eq. (3.39):

$$A = 1 - \frac{4\Delta D}{L} \tag{3.39}$$

If the value of A is known, then the position can be correctly calculated using Eq. (3.40):

$$D = \frac{ALV_{I2}}{V_{I1}+AV_{I2}} \tag{3.40}$$

An experimental determination of ΔD can be used to determine a value for A. This determination can be done by placing a neutron absorber in front of the detector tube

at a known position near its center. The detector is put in a state where voltage offset corrections are handled. The detector is illuminated by a neutron source, and a position histogram of counts vs. position along the tube is collected. If the absorber is a slit, a peak will appear in the position histogram, whose shape will be nearly Gaussian if the detector is working well. A least squares fit of a Gaussian curve to the peak is performed, allowing the peak position to be deduced from the fit coefficients. Then, ΔD is the difference between the peak position and the absorber position. If the absorber is not a slit, its edge will cast a shadow, which will appear in the position histogram. The shadow edge often declines gradually over a span of several pixels. A hyperbolic tangent function is used as a model of such an unsharp edge. The coefficients from a least squares fit of the hyperbolic function to the shadow edge are used to deduce its position. These fits are restricted to a small range of pixels spanning the feature to avoid distortion from other features that may exist elsewhere in the histogram. Adequate statistics for curve fitting are required, which usually requires at least 50 counts per pixel in the histograms.

Data acquisition systems will generally split up the length of a detector tube into some number N of pixels and only report the pixel number in which an event is calculated to lie. Position calculations often take place within an FPGA, in which it is awkward to carry out floating point multiplications. The gain correction is therefore accomplished by multiplying V_{I1} by some integer K_1, and V_{I2} is multiplied by the integer closest to $K_2 = AK_1$. If the feature in the position histogram is determined to be ΔN pixels displaced from the absorber position, the gain mismatch is $A = 1 - (4\Delta D/L) = 1 - (4\Delta N)/N$, and the multiplier for V_{I2} becomes Eq. (3.41):

$$K_2 = K_1 - \frac{4K_1}{N}\Delta N \tag{3.41}$$

For the common case where $K_1 = 2048$ and $N = 256$, $(4K_1)/N = 32$.

3.2.1.8 Position Resolution and Noise Sources

Another parameter of interest for an LPSD is its position resolution. If many neutrons hit the detector at the same location along its length, the measured positions will scatter around that location. If an acquisition is performed where neutrons are only allowed to reach the detector tube at one position along its length, a peak will appear in the position histogram. The resolution can be measured as the full width at half maximum (FWHM) of the peak in the position histogram from such a measurement, with small values for the FWHM being desirable. For a detector that is working well, the peak shape is often well-approximated by a Gaussian curve. In such cases, the resolution can be measured by a least squares fit of a Gaussian curve to the peak. The FWHM can then be deduced from the fit parameters. The achievable resolution is dependent on many factors, which will be discussed in this section. FWHM values in the 5–20 mm range are often observed.

The position resolution is primarily determined by noise in the electronics used to measure the position. An important contribution to this noise is the intrinsic noise in the resistors and operational amplifiers, which are used in the detector circuits. A detailed analysis of the influence of these noise sources on the resolution is the subject of Sect. 3.2.2. One significant result is that noise from the central wire of the detector tube is often dominant. Under such conditions (with other factors being equal), the FWHM will be inversely proportional to the square root of the central wire resistance. Another result is that the FWHM is inversely proportional to the charge Q delivered by a detection event. Actions to increase Q, such as raising the detector bias or restricting attention to events high on the pulse height spectrum, will make the FWHM smaller. The S/N in the detector tends to be proportional to the FWHM, expressed as a fraction of the tube length. For a constant S/N, the FWHM in distance units will be proportional to the tube length. If the central wire resistance is the dominant noise source and that resistance is proportional to the tube length, the S/N will be inversely proportional to the square root of the tube length, making the FWHM in distance units proportional to the square root of the tube length.

This dependence of resolution on the delivered charge creates a tradeoff in the choice of discriminator settings. As can be seen in Fig. 3.16, considerable variation exists in the amplitude of pulses from an LPSD tube. As the discriminator threshold is increased, the fraction of low amplitude events that get rejected will increase. Because the eliminated events have the poorest position resolution, the overall position resolution of the detector will improve. This comes at the cost of a decreased fraction of accepted events.

Noise pickup can add to the intrinsic noise. One source can be the preamplifier power cables. The need to supply power forces some current to flow along the ground wires in these cables, which tries to create an offset between the preamplifier ground and the power supply ground, which may differ between the preamplifiers. The preamplifiers also need to be grounded to the detector frame to be referenced to the detector tube ground. The competing ground references can cause a ground loop current to flow through the detector frame and along the power cable ground wires. Magnetic pickup in the loop formed by the power cables and the detector frame can also generate similar ground loop currents. If resistance along the path of the ground loop current exists between the preamplifiers along the detector frame, offset voltages will be generated, which the preamplifiers pick up as noise. To minimize this effect, it is important to have a low-resistance connection of the preamplifier ground to the detector frame. There must also be low resistance for the ground current along the detector frame. For detector geometries where most of the ground loop current passes along the detector tubes, a solid grounding of the tube to the frame on both sides is important. Magnetic pickup can be minimized by routing the power supply cables close to the detector frame.

The currents in the tube to preamplifier wires are small. The lowest resistance path for pickup voltages on these wires to create noise currents is along the central wire of the tube between the preamplifiers. This path has a few thousand ohms of resistance, low enough for such currents to be significant compared with the currents from a detection event. The tube to preamplifier wires need to be mounted within a

grounded enclosure to minimize noise pickup. Crosstalk between traces on a circuit board can be significant. One observed example of this crosstalk was a trace carrying a 10 MHz timing signal that ran too close to the trace from an integrator output to the ADC. The ADC saw the integrator output with crosstalk from the 10 MHz signal added, increasing the noise in the measurement. Noise pickup can come from differences and fluctuations in ground references between the power supplies, the communication connections, the bias connections, and the mounting points of a detector module. Such problems are solved by isolating some grounds and tying together other grounds, with judgement and compromises required.

During a measurement, the ADC converts the continuous analog signal from the integrator to a digital output, making the uncertainty in the reading at least as large as the ADC step size. The length of the detector tube is partitioned into some number of bins. When a position calculation is performed, the result is used to determine the bin in which it fits. The bin number gets turned into a pixel ID, which is what gets transmitted as data. This process makes the uncertainty in the position reading at least as large as the bin length.

The ADC step size is represented by ΔV_{ADC}. Assume that a detector pulse delivers a charge Q at a distance D from side 1 along a tube of length L. If this pulse delivers voltage V_{ADC1} to ADC 1, this amounts to $(N_{\mathrm{ADC1}} + E_1) = (V_{\mathrm{ADC1}}/\Delta V_{\mathrm{ADC}})$ ADC steps, where N_{ADC1} is the nearest integer, and E_1 is the error from digitization. Rounding is assumed to be carried out so that $-1/2 < E_1 < 1/2$. Figure 3.22 illustrates the definition of these quantities.

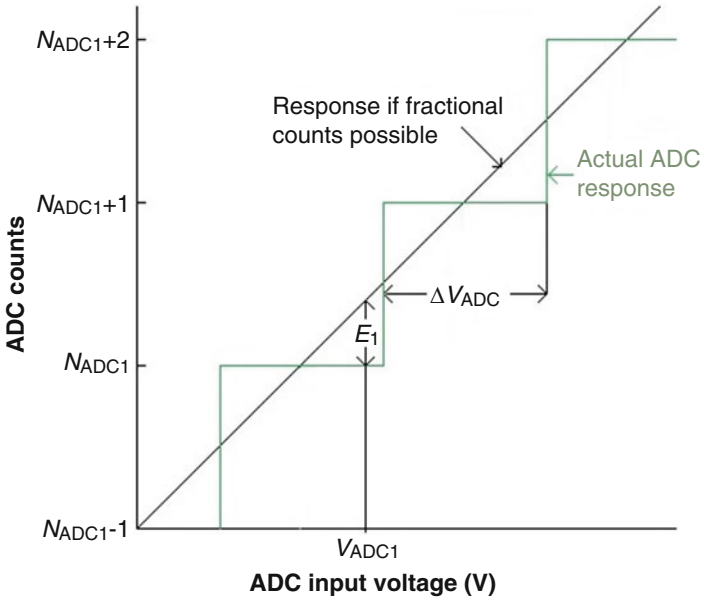

Fig. 3.22 Plot of ADC counts as a function of the input voltage, illustrating the definition of quantities used in digitization error calculations

An error E_2 can similarly be defined as the error from digitization on side 2. When $N = Q/\Delta V_{\mathrm{ADC}}$, a calculation analogous to the derivation of Eq. (3.36) yields a position offset $\Delta D_1 = (-E_1 D)/(E_1 + N)$ owing to E_1 and a position offset $\Delta D_2 = (E_2[L - D])/(E_2 + N)$ owing to E_2. The combined offset is $\Delta D = \Delta D_1 + \Delta D_2$. Defining $R = D/L$ and assuming $N \gg 1$ gives Eq. (3.42):

$$\begin{aligned} \Delta R &= \frac{\Delta D_1 + \Delta D_2}{L} \\ &= \frac{E_2(1-R)}{E_2 + N} - \frac{E_1 R}{E_1 + N} \\ &\approx \frac{E_2(1-R) - E_1 R}{N} \end{aligned} \tag{3.42}$$

Assuming E_1 and E_2 vary independently and are equally likely to have any value in their range, the average value of $(\Delta R)^2$ is given by Eq. (3.43):

$$\int_{E_1=-\frac{1}{2}}^{\frac{1}{2}} \int_{E_2=-\frac{1}{2}}^{\frac{1}{2}} (\Delta R)^2 dE_2 dE_1 = \frac{1}{12N^2}\left((R-1)^2 + R^2\right) \tag{3.43}$$

Because the average value of ΔR is 0, the root mean square (RMS or rms) value of ΔR is given by Eq. (3.44):

$$\Delta R_{\mathrm{rms}} = \frac{1}{2N}\sqrt{\frac{(R-1)^2 + R^2}{3}} \tag{3.44}$$

ΔR_{rms} weakly depends on the position along the tube: $\Delta R_{\mathrm{rms}} = 0.2886/N$ at the tube ends, and $\Delta R_{\mathrm{rms}} = 0.2041/N$ at the center. The factor for converting an RMS deviation to FWHM for a Gaussian distribution is $2\sqrt{2\ln 2} = 2.354$. To the extent that ΔR matches this distribution, $\Delta R_{\mathrm{FWHM}} = 0.6795/N$ at the tube ends, and $\Delta R_{\mathrm{FWHM}} = 0.4805/N$ at the center. Large values of N are desired for minimizing this deviation. An upper limit on its value is set by the number of bins on the ADC, which is 1024 for the version used on the ROC board. Gains should be set up to make the pulse height spectrum come as close to spanning the full range of the ADC without saturating as is feasible.

Assume that the length of the detector tube is partitioned into K bins. An event calculated to lie at distance D along the tube is at $(DK/L) = N_{\mathrm{bin}} + E$ bins, where N_{bin} is the nearest integer, and $-½ < \mathrm{E} < ½$. The position offset as a fraction of the tube length is $\Delta R = E/K$. The average value of $(\Delta R)^2$ is given by Eq. (3.45):

$$\int_{-\frac{1}{2}}^{\frac{1}{2}} \frac{E^2 dE}{K^2} = \frac{1}{12K^2} \tag{3.45}$$

The RMS deviation is given by Eq. (3.46):

$$\Delta R_{\text{rms}} = \frac{1}{\sqrt{12}K} = \frac{0.2886}{K} \tag{3.46}$$

which is independent of the position. Converting ΔR_{rms} to ΔR_{FWHM} yields $\Delta R_{\text{FWHM}} = 0.6795/K$.

The contributions to the resolution must be added in quadrature, as shown in Eq. (3.47):

$$\Delta R_{\text{FWHM total}} = \sqrt{\Delta R^2_{\text{FWHM tube bins}} + \Delta R^2_{\text{FWHM ADC bins}} + \Delta R^2_{\text{FWHM noise}}} \tag{3.47}$$

3.2.1.9 Detector Module Construction

The position determinations reveal the location of a neutron along the axis of the tube. Perpendicular to that axis, the neutron is only determined to have arrived within the inner diameter of the tube. Arrays of tubes must be used to locate a neutron in two dimensions. Several LPSD tubes are usually mounted together to form a detector module, which usually comprise eight tubes each. The modules are often designed to be installed beside each other so that an array of modules can cover a greater distance perpendicular to the tubes. Several geometries are possible, as indicated in Fig. 3.23. The two-sided geometry has two preamplifier boxes—one for each side of the tube. The tubes mount to these boxes, which hold them in the correct positions relative to the module. This mounting is also a place where the tubes connect to the module ground. The preamplifier is mounted in the box, which forms a shielded enclosure for it and for the wires from the tube end to the preamplifier. The preamplifier must

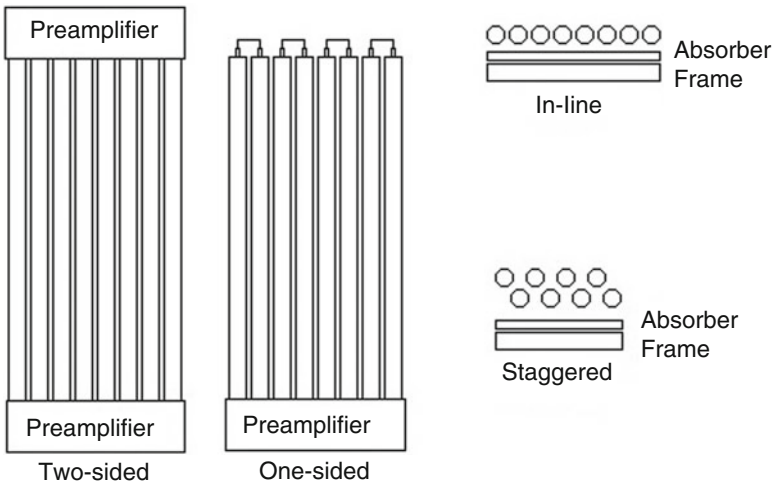

Fig. 3.23 Detector geometries

be mounted to the box in a manner that creates a good ground connection to the module. In some cases, the tubes are attached to the detector frame instead of the preamplifier box. Details of the shape and mounting of the preamplifier boards and their boxes can vary greatly. They often depend on the geometric constraints of the instrument for which the module is designed.

Sometimes, the instrument geometry may be such that no room is available to install a preamplifier on one of the detector sides. A one-sided geometry is then used—the preamplifier and its box are installed on only one side of the module. The tubes of the module are grouped into adjacent pairs. A jumper is installed between the center wire feedthroughs of a pair on the other side of the tubes. As far as resolution and position determination are concerned, the two tubes of length L behave as if they form a single tube of length $2L$.

The most straightforward way to arrange the tubes on the detector module is in-line; that is, the tubes are in the same plane, parallel to each other, and near each other. This arrangement helps maintain uniform illumination conditions between tubes. It also minimizes differences in neutron flight distance from tube to tube. The primary drawback is the gaps between the tubes, which are regions in which an arriving neutron will fail to be detected. The staggered arrangement is sometimes used to eliminate these gaps. The tubes are mounted in two rows—one slightly more than a tube's diameter behind the other. Traversing sideways across the module, the tubes alternate between being in the front or back row. The spacing between tubes is such that the inner diameters of the front-row tubes overlap the inner diameters of the back-row tubes. This overlap eliminates the gaps in coverage and causes the back-row of tubes to be partially shadowed by the front-row tubes. The amount of shadowing depends on the direction of an arriving neutron. An arriving neutron must travel farther to reach a back-row tube than to reach a front-row tube. This discrepancy must be accounted for when interpreting time-of-flight (TOF) measurements.

Figure 3.23 shows an absorber mounted between the tubes and the detector frame. It is possible for neutrons that have traveled past the detector tubes to be scattered off the frame and back into the tubes. Neutrons backscattered by other means may also approach the detector tubes from the rear. In either case, the neutrons create a neutron background with a poorly defined trajectory that should be eliminated. To absorb the backscattered neutrons, an absorber—a sheet of neutron-absorbing material—is often attached to the frame.

The frame's importance as a structural component varies. In some cases, the detector tubes are the main source of structural support between the preamplifier boxes at the ends, and the frame is only a thin sheet of metal to support the absorber plates and some circuit boards. In other cases, the frame is the primary source of structural support for the module and therefore must have more rigid construction. The frame should provide a low-resistance ground path between the preamplifiers to minimize the sensitivity of detector noise to the quality of the tube-to-ground connections.

The position resolution of an LPSD perpendicular to the detector tube is limited by the inner diameter of the tube. This relation creates a desire to use small diameter

tubes, which can lead to tubes with a high length-to-diameter ratio. These tubes are susceptible to a form of catastrophic failure in which the central wire of a biased tube is electrostatically attracted to the tube wall. When the wire approaches the wall, an electrical discharge occurs, which is powerful enough sever the wire. A theoretical analysis of this mechanism is the subject of Sect. 3.2.3. This analysis predicts that the danger of such a failure occurring depends on the value of a parameter K, which will be derived as Eq. (3.107) and is reproduced here as Eq. (3.48):

$$K = \frac{V_0^2 L^2}{W_0 R^2 (\ln[w])^2} \tag{3.48}$$

where V_0 is the bias voltage, L is the tube length, W_0 is the tension on the central wire, R is the inner radius of the tube, and w is the ratio of the wire diameter to the inner diameter of the tube. The mechanism begins to be a concern for $K > 9 \times 10^{10}$ V^2/N, where N refers to newtons. Failure is likely regardless of the tube straightness at $K = 18 \times 10^{10}$ V^2/N. The value of K that can be tolerated improves if the tube is kept very straight. When operating close to the upper limit, the tolerance for deviations from straightness can be as low as 0.1 mm. To give some sense of conditions for which these effects matter, a 1 m long detector tube with an 8 mm outer diameter and 7.1 mm inner diameter can be successfully operated at an 1800 V bias, but attention to straightness is important at these conditions.

Tubes with a high length-to-diameter ratio are not very stiff with respect to sideways deflections. Therefore, additional supports along the length of the tube are needed to maintain the required straightness. Typically, three additional supports are used at approximately one-fourth, one-half, and three-fourths of the way along the length of the tube. These supports can be a source of additional neutron absorption and scattering behind the detector tubes, and they create gaps in the absorber plates. Such effects can cause minor variations in the counts at the positions where a support is present.

3.2.1.10 Detector Calibration and Characterization

One objective of detector calibration is to have a known relationship between the bin number where a neutron detection is reported and the physical location along the detector tube where the neutron was absorbed. This objective involves three lower levels of calibration. One level is correction for voltage offsets in the detector electronics. Section 3.2.1.6 discussed the influence of such offsets on position determinations and calibration techniques for canceling them out. The second level is to ensure that a linear relationship exists between the bin number and the corresponding position along the detector tube. Section 3.2.1.7 discussed the influence of gain mismatches on this type of error and outlined techniques for determining the required corrections. The third level is to determine the distance along the detector tube that a bin occupies. As mentioned in Sect. 3.2.1.5, end effects make this

more complex than dividing the tube length by the number of bins. It is perhaps best determined by illuminating the detector with neutrons emerging from a slit at several known distances along the detector tube and then determining the shift in the position of the peaks in the measured position histograms.

Another position-related characterization of a detector is its position resolution. Section 3.2.1.8 discusses what this means, how it is measured, and the factors that influence it.

Two related characterizations of detector performance are the counting efficiency and gamma rejection. Counting efficiency is the fraction of neutrons arriving at the detector that are detected, which requires two steps to occur. The first step is for the neutron to have an interaction with the detection gas, which has a probability discussed in Sect. 3.2.1.2. The second step is for the detector pulse generated by the reaction to be strong enough to trigger the discriminator. The efficiency of this step can be improved by lowering the discriminator setting. However, as discussed in Sect. 3.2.3, too low of a discriminator setting will allow some unwanted gamma ray detections to also occur, resulting in poor gamma ray rejection. Although LPSD detectors have better gamma ray rejection than many alternative detector types, a trade-off still exists between counting efficiency and gamma ray rejection, which must be considered. Examination of the pulse-height spectrum from a detector can provide some guidance in the selection of the best discriminator setting. The pulse-height spectrum can also be used to estimate how the fraction of neutron rejections varies with the discriminator setting. The counting efficiency and gamma ray rejection of a detector can be determined by measuring its count rate when exposed to neutron and gamma ray sources of known intensity. The accuracy of this technique is usually limited by uncertainties in the intensity of the sources. Although a reference detector can be used to measure the source intensities, the results are still no better than the uncertainties in the counting efficiency of the reference detector.

Similar to other types of detectors for neutrons in thermal energy ranges, LPSD detectors have no intrinsic ability to measure the kinetic energy of the neutrons they detect. This lack of ability is because the kinetic energy of a thermal neutron is approximately 0.025 eV, which is swamped by the 765 keV released when the neutron reacts with ^{3}He. The kinetic energy determination is dependent on other features of the instrument in which they operate. For continuous neutron sources, the energy is typically set using either a velocity selector or diffraction of the neutrons by a crystal. For pulsed neutron sources, TOF can be used to determine the kinetic energy of a neutron. This use of TOF requires every neutron detection to be associated with a time stamp measuring the time interval between the creation and the detection of the neutron. The time resolution needed for this time stamp can be estimated by noting that a typical thermal energy neutron moves at 2200 m/s, but there is an uncertainty of a millimeter or more in the distance within the detector tube in which the neutron interacts with the detector gas. This uncertainty creates an uncertainty of at least 0.5 μs in the time in which the neutron will be detected. A time stamp resolution of 100 ns, as is used at SNS, is short enough to be a negligible contribution to the TOF uncertainty.

3.2.2 LPSD Intrinsic Noise

The influence of intrinsic noise in amplifier first-stage components on the resolution of an LPSD is examined in this section. Noise contributions from external sources are not considered, nor is additional noise owing to later amplification or integration stages. The simplified representation of the input circuit shown in Fig. 3.24 is analyzed in this section. All arrows next to current labels in this figure show the direction of current flow for positive values of the parameter. All arrows next to voltage symbols show the direction of increasing voltage for positive values of the parameter. Here, I_P is current injected by a detection event at some point along the wire of a detector tube. This wire is represented by resistors R_{W1} and R_{W2}. The total wire resistance is $R_W = R_{W1} + R_{W2}$. The gain of first-stage amplifiers 1 and 2 is set by resistors R_{F1} and R_{F2}. Each of these resistors has an intrinsic noise, which is represented by V_{nF1}, V_{nF2}, V_{nW1}, and V_{nW2}. Furthermore, intrinsic noise is associated with the operational amplifiers for the first stage, which occurs in two distinct ways. First, voltage noise can be thought of as fluctuating inaccuracies in an operational amplifier's determination of the voltage presented to its input. This quantity is represented by V_{n1} and V_{n2}. Second, current noise is caused by fluctuations in the current draw of the operational amplifier input. This quantity is represented by i_{n1} and i_{n2}. The first-stage outputs, V_{O1} and V_{O2}, are integrated over a time interval t_m to create the outputs V_{I1} and V_{I2}, which are used for the position calculation.

3.2.2.1 Solution Using Instantaneous Values of Noise Voltages

In the circuit in Fig. 3.24, voltages should add up to 0 around the loop from the positive input of amplifier 1, through the ground to the positive input of amplifier 2, across to the negative input of amplifier 2, through the tube wire to the negative input of amplifier 1, and back to the positive input. This path gives $0 = -V_{n1} - V_{nW1} + R_{W1}I_{W1} - R_{W2}I_{W2} + V_{nW2} + V_{n2}$. Because $I_{W1} = I_p - I_{W2}$, $0 = -V_{n1} - V_{nW1} + V_{nW2} + V_{n2} + R_{W1}I_P - R_WI_{W2}$. Solving for I_{W2} gives Eq. (3.49):

$$I_{W2} = \frac{R_{W1}I_p - V_{n1} - V_{nW1} + V_{nW2} + V_{n2}}{R_W} \tag{3.49}$$

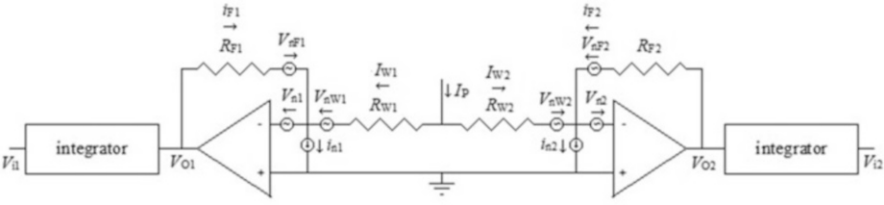

Fig. 3.24 Simplified first-stage input circuit for an LPSD

Substituting Eq. (3.49) into $I_{W1} = I_p - I_{W2}$ gives Eq. (3.50):

$$I_{W1} = \frac{R_{W2}I_p + V_{n1} + V_{nW1} - V_{nW2} - V_{n2}}{R_W} \tag{3.50}$$

The feedback connection from the amplifier 1 output to its input yields $V_{O1} = R_{F1}i_{F1} - V_{nF1} - V_{n1}$.

Because $i_{F1} = i_{n1} - I_{W1}$, V_{O1} is given by Eq. (3.51):

$$V_{O1} = -V_{nF1} - V_{n1} + R_{F1}i_{n1} - \frac{R_{F1}}{R_W}\left(R_{W2}I_p + V_{n1} + V_{nW1} - V_{nW2} - V_{n2}\right) \tag{3.51}$$

Similarly, V_{O2} is given by Eq. (3.52):

$$V_{O2} = -V_{nF2} - V_{n2} + R_{F2}i_{n2} - \frac{R_{F2}}{R_W}\left(R_{W1}I_p - V_{n1} - V_{nW1} + V_{nW2} + V_{n2}\right) \tag{3.52}$$

The integrator output is the integral of the input voltage over a fixed time interval t_m. If an integrator time constant τ is defined such that the output voltage of the integrator is $\frac{1}{\tau}\int_0^{t_m} V dt$, then the integration function can be defined by Eq. (3.53):

$$\mathrm{INT}(V) = \frac{1}{\tau}\int_0^{t_m} V dt \tag{3.53}$$

The action of this function is illustrated in Fig. 3.25.

Note that $\mathrm{INT}(I_P) = Q/\tau$, where Q is the charge delivered by I_P over the time interval t_m. It is convenient to define the following values in Eqs. (3.54), (3.55), and (3.56):

$$D = \mathrm{INT}(V_{n1} + V_{nW1} - V_{nW2} - V_{n2}) \tag{3.54}$$

$$E = \mathrm{INT}(-V_{nF2} - V_{n2} + R_{F2}i_{n2}) \tag{3.55}$$

$$F = \mathrm{INT}(-V_{nF1} - V_{n1} + R_{F1}i_{n1}) \tag{3.56}$$

Then, V_{I1} and V_{I2} are given by Eqs. (3.57) and (3.58), respectively:

$$V_{I1} = \mathrm{INT}(V_{O1}) = F - \frac{R_{F1}R_{W2}Q}{\tau R_W} - \frac{R_{F1}D}{R_W} \tag{3.57}$$

$$V_{I2} = \mathrm{INT}(V_{O1}) = E - \frac{R_{F2}R_{W1}Q}{\tau R_W} + \frac{R_{F2}D}{R_W} \tag{3.58}$$

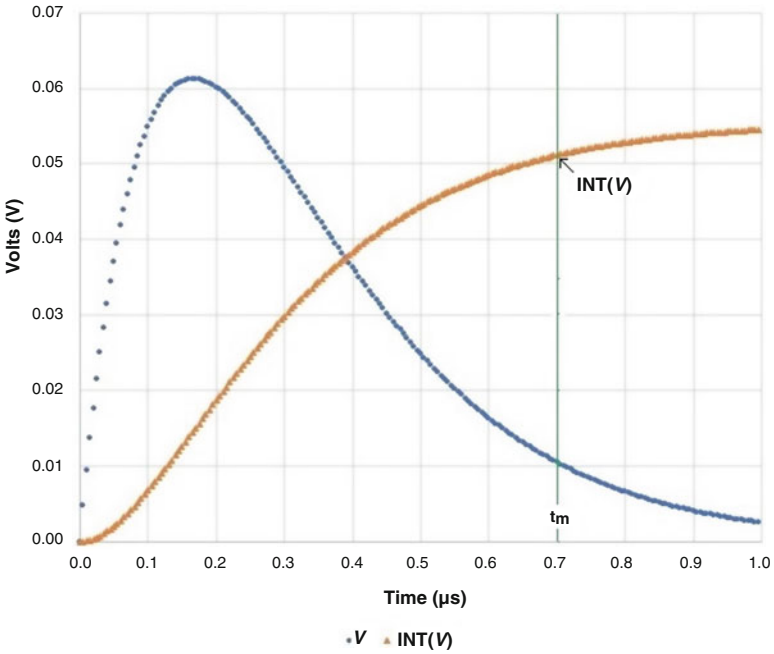

Fig. 3.25 Illustration of the integrator function acting on a voltage input that resembles a pulse from a detector. For this illustration, $\tau = 0.5$ μs, and $t_m = 0.7$ μs. The arrow points to the voltage, which would be the output value of INT(V)

The amplifier gains must be matched for this circuit to yield accurate position measurements, so $R_{F1} = R_{F2} = R_F$ is expected. The position P along the wire can be calculated using Eq. (3.59):

$$P = \frac{V_{I2}}{V_{I1} + V_{I2}} = \frac{E - \frac{R_F R_{W1} Q}{\tau R_W} + \frac{R_F D}{R_W}}{E + F - \frac{R_F Q}{\tau}} = \frac{\frac{R_{W1}}{R_W} - \frac{\tau E}{Q R_F} - \frac{\tau D}{Q R_W}}{1 - \frac{\tau}{Q R_F}(E + F)} \tag{3.59}$$

If Q is large enough that $(\tau/QR_W)(E + F) \ll 1$, then a good approximation is obtained by multiplying the numerator and denominator by $1 + (\tau/QR_F)(E + F)$ and then discarding any terms that are a product of noise voltages. This process results in Eq. (3.60):

$$P = \frac{R_{W1}}{R_W} - \frac{\tau E}{Q R_F} - \frac{\tau D}{Q R_W} + \frac{\tau R_{W1}}{M Q R_F R_W}(E + F) = \frac{R_{W1}}{R_W} - \frac{\tau D}{Q R_W} - \frac{\tau R_{W2} E}{Q R_F R_W} + \frac{\tau R_{W1} F}{Q R_F R_W} \tag{3.60}$$

This calculation gives the expected P based on whatever values the various noise voltages and currents happened to be during a particular acquisition. The next goal is

to determine the expected variation in the measured P values over many acquisitions. The noise voltages present at the amplifier outputs are filtered through the integrators before being applied to the calculation of P, so calculating the influence of this filtering is necessary.

3.2.2.2 Filtering of Noise by the Integrator

A noise source with spectral density N_f is assumed to be processed through an integrator, which outputs $1/\tau$ times the integral of its instantaneous values over time t_m. If it can be assumed that N_f is significant over a frequency range from f_1 to f_2, then a frequency interval Δf can be chosen such that $\Delta f \ll 1/t_m$. The resultant waveform, selecting all noise in the range f to $f + \Delta f$, will have an average RMS amplitude of A_f, which is determined by Eq. (3.61):

$$A_f^2 = \int_f^{f+\Delta f} N_f^2 df = N_f^2 \Delta f \tag{3.61}$$

The frequency dispersion will be small enough that within the integration time t_m, the dispersion can be approximated as $V_f = \sqrt{2} A_f \exp\{iB\} \exp\{i2\pi ft\}$, where t is the time since the integration began, and B is a phase factor, which varies randomly between frequency intervals and between successive integrations. The noise from the frequency interval Δf will emerge from the integrator as a contribution V_{If} calculated by Eq. (3.62):

$$\begin{aligned} V_{If} &= \frac{1}{\tau} \int_0^{t_m} V_f dt \\ &= \sqrt{2\Delta f} \frac{N_f}{\tau} \exp\{iB\} \int_0^{t_m} \exp\{i2\pi ft\} dt \\ &= \sqrt{2\Delta f} \frac{N_f}{2\pi f \tau} \frac{\exp\{iB\}}{i} (\exp\{i2\pi f t_m\} - 1) \end{aligned} \tag{3.62}$$

Euler's formula yields Eq. (3.63):

$$\exp\{i2\pi f t_m\} - 1 = \cos 2\pi f t_m - 1 + i \sin 2\pi f t_m \tag{3.63}$$

which has amplitude given by Eq. (3.64):

$$\| \exp\{i2\pi f t_m\} - 1 \| = \sqrt{2 - 2\cos 2\pi f t_m} \tag{3.64}$$

Because $(\exp\{iB\})/i$ remains a random phase, V_{If} is a vector with amplitude given by Eq. (3.65):

$$\| V_{If} \| = \sqrt{2\Delta f}\frac{N_f}{2\pi f\tau}\sqrt{2-2\cos 2\pi f t_m} \tag{3.65}$$

The amplitude in Eq. (3.65) is random phase, yielding an RMS amplitude given by Eq. (3.66):

$$V_{If\text{rms}} = \frac{N_f\sqrt{\Delta f}}{2\pi f\tau}\sqrt{2-2\cos 2\pi f t_m} \tag{3.66}$$

To calculate the RMS amplitude over the frequency range from f_1 to f_2, the sum of squares must first be formed, given by Eq. (3.67):

$$S = \sum V_{If\text{rms}}^2 = \sum_{j=0}^{(f_2-f_1)/\Delta f}\frac{N_f^2\Delta f(2-2\cos 2\pi f t_m)}{4\pi^2 f^2\tau^2} \tag{3.67}$$

where $f = f_1 + j\Delta f$. Going to the limit $\Delta f = 0$ gives the integral in Eq. (3.68):

$$S = \frac{1}{4\pi^2\tau^2}\int_{f_1}^{f_2}\frac{N_f^2}{f^2}(2-2\cos 2\pi f t_m)df = \frac{t_m}{\tau^2}G\left(N_f^2\right) \tag{3.68}$$

where $G\left(N_{\text{f}}^2\right)$ is given by Eq. (3.69):

$$G\left(N_f^2\right) = \frac{1}{\pi}\int_{\omega_1}^{\omega_2}\frac{N_f^2}{\omega^2}(1-\cos\omega)d\omega \tag{3.69}$$

where $\omega_1 = 2\pi f_1 t_m$, and $\omega_2 = 2\pi f_2 t_m$.

The RMS value for the noise over the full frequency range is then given by Eq. (3.70):

$$V_{I\text{rms}} = \sqrt{S} \tag{3.70}$$

For cases in which N_f is not frequency-dependent, $G\left(N_f^2\right) = G_1 N_f^2$, where G_1 is given by Eq. (3.71):

$$G_1 = \frac{1}{\pi}\int_{\omega_1}^{\omega_2}\frac{(1-\cos\omega)d\omega}{\omega^2} \tag{3.71}$$

$G_1 = 0.5$ when all frequencies are included. For a low-frequency cutoff $\omega_1 = 2\pi f_1 t_m \ll 1$, subtract $(\omega_1/2\pi)\left(1-\omega_1^2/18\right)$ from G_1. For a high-frequency cutoff $\omega_2 = 2\pi f_2 t_m \gg 1$, subtract $1/(\pi\omega_2)$ from G_1.

3.2.2.3 Calculation of RMS Noise Amplitudes

A resistor of size R will at best have noise with a spectral density $N_f = \sqrt{4\pi k_B T R}$, where $k_B = 1.38 \times 10^{-23}$ J/K is the Boltzmann constant, and T is the temperature. In upcoming equations, $C_r = 4\pi k_B T$ is used as the noise multiplier for resistors, and $S\left(N_f^2\right)$ is used as an operator that calculates the integral of Eq. (3.68) for N_f^2. Also, V_{n1}, V_{n2}, and i_n are interpreted as the spectral density of these noise sources. Let D_n, E_n, and F_n be the squared noise sums associated with the values D, E, and F, which were defined in Eqs. (3.54), (3.55), and (3.56).

$$D_n = S\left(V_{n1}^2 + V_{n2}^2 + C_r R_{W1} + C_r R_{W2}\right) = S\left(V_{n1}^2 + V_{n2}^2 + C_r R_w\right) \tag{3.72}$$

$$E_n = S\left(C_r R_{F2} + V_{n2}^2 + R_{F2}^2 i_{n2}^2\right) \tag{3.73}$$

$$F_n = S\left(C_r R_{F1} + V_{n1}^2 + R_{F1}^2 i_{n1}^2\right) \tag{3.74}$$

H is defined as the sum of the squares of all noise sources in the position calculation in Eq. (3.60). Then, H is given by Eq. (3.75):

$$H = \frac{\tau^2}{Q^2}\left(\frac{D_n}{R_W^2} + \frac{R_{W2}^2 E_n}{R_W^2 R_F^2} + \frac{R_{W1}^2 F_n}{R_W^2 R_F^2}\right) \tag{3.75}$$

If a good match in amplifier properties exists between the two sides, then $V_{n1} = V_{n2} = V_n$, $i_{n1} = i_{n2} = i_n$, and $R_{F1} = R_{F2} = R_F$. Therefore, $E_n = F_n$, and Eq. (3.75) can be rewritten as Eq. (3.76):

$$\begin{aligned} H &= \frac{\tau^2}{Q^2}\left(\frac{D_n}{R_W^2} + \frac{R_{W1}^2 + R_{W2}^2}{R_W^2 R_F^2} E_n\right) \\ &= \frac{\tau^2}{Q^2} S\left(\frac{2V_n^2}{R_W^2} + \frac{C_r}{R_w} + \frac{R_{W1}^2 + R_{W2}^2}{R_W^2}\left(\frac{C_r}{R_F} + i_n^2 + \frac{V_n^2}{R_F^2}\right)\right) \end{aligned} \tag{3.76}$$

The RMS amplitude of the noise in the position determination, as a fraction of the wire length, is given by Eq. (3.77):

$$\begin{aligned} P_n = \sqrt{H} &= \frac{\tau}{Q}\sqrt{S\left(\frac{2V_n^2}{R_w^2} + \frac{C_r}{R_W} + \frac{R_{W1}^2 + R_{W2}^2}{R_W^2}\left(\frac{C_r}{R_F} + i_n^2 + \frac{V_n^2}{R_F^2}\right)\right)} \\ &= \frac{\sqrt{t_m}}{Q}\sqrt{G\left(\frac{2V_n^2}{R_W^2} + \frac{C_r}{R_W} + \frac{R_{W1}^2 + R_{W2}^2}{R_W^2}\left(\frac{C_r}{R_F} + i_n^2 + \frac{V_n^2}{R_F^2}\right)\right)} \end{aligned} \tag{3.77}$$

For a Gaussian distribution, conversion from an RMS amplitude to FHWM requires multiplication by a factor of $2\sqrt{2\ln 2} = 2.354$.

P_n would need to be multiplied by the wire length to obtain the noise in terms of a distance. The only term in H that depends on the position along the wire is $\left(R_{W1}^2 + R_{W2}^2\right)/R_W^2$, which varies from 0.5 at the center of the wire to 1 at the ends of the wire.

J is defined as the sum of the squares of all noise sources in the determination of V_{I1} in Eq. (3.78):

$$J = F_n + \frac{R_{F1}^2}{R_W^2} D_n = S\left(CR_{F1} + V_{n1}^2 + R_{F1}^2 i_{n1}^2 + \frac{R_{F1}^2}{R_w^2}\left(V_{n1}^2 + V_{n2}^2\right) + \frac{CR_{F1}^2}{R_W}\right) \quad (3.78)$$

The RMS noise at the integrator output V_{I1} is given by Eq. (3.79):

$$\begin{aligned} V_{I1\text{rms}} &= \sqrt{J} \\ &= \sqrt{S\left(C_r R_{F1} + V_{n1}^2 + R_{F1}^2 i_{n1}^2 + \frac{R_{F1}^2}{R_W^2}\left(V_{n1}^2 + V_{n2}^2\right) + \frac{C_r R_{F1}^2}{R_W}\right)} \\ &= \frac{\sqrt{t_m}}{\tau}\sqrt{G\left(C_r R_{F1} + V_{n1}^2 + R_{F1}^2 i_{n1}^2 + \frac{R_{F1}^2}{R_W^2}\left(V_{n1}^2 + V_{n2}^2\right) + \frac{C_r R_{F1}^2}{R_W}\right)} \end{aligned} \quad (3.79)$$

3.2.2.4 Noise Calculations for a Specific Detector

In this section, values for noise parameters are calculated for an actual detector with 654 mm long tubes whose wire resistance is measured to be 3380 Ω. The feedback resistance is $R_F = 24{,}000\ \Omega$. AD8022 operational amplifiers are used, for which the data sheet [15] quotes $i_n = 1.2 \times 10^{-12}$ A/√Hz and $V_n = 2.5 \times 10^{-9}$ V/√Hz. The integrators use an integration time of $t_m = 7 \times 10^{-7}$ s.

Bandwidth limitations on the noise sources vary with the nature of the source. For the thermal noise from the tube wire resistance, a low-frequency roll-off is created because the currents from this source must travel along a path between the preamplifier inputs on each side of the tube. As can be seen in Fig. 3.18, this path includes capacitors C_{s1} and C_{s2}. These are 15 nF bias isolation capacitors, which, for this path, are connected in series, giving a combined capacitance of 7.5 nF. At low frequencies, the impedance of these capacitors limits the current that the wire noise can induce along this path, which limits the gain of the preamplifiers. A roll-off frequency for this mechanism can be estimated by calculating the frequency for which the amplitude of the capacitor impedance is equal to the tube wire resistance, as shown in Eq. (3.80):

$$f_1 = \frac{1}{2\pi\left(3{,}830\ \Omega \times \left(7.5 \times 10^{-9}\ \text{F}\right)\right)} = 5{,}540\ \text{Hz} \quad (3.80)$$

For the correction to G_1, $\omega_1 = 2\pi f_1 t_m = 0.0243$, $\Delta G_1 \approx \omega_1/2\pi = 0.0038$.

Table 3.1 Equation terms

Term	Value (A^2/s)	S (A^2)	$R_F^2 S$ (V^2)
$\frac{2V_n^2}{R_W^2}$	1.094×10^{-24}	1.01×10^{-15}	5.81×10^{-7}
$\frac{C_r}{R_W}$	1.538×10^{-23}	1.419×10^{-14}	8.176×10^{-6}
$\frac{C_r}{R_F}$	2.166×10^{-24}	1.999×10^{-15}	1.151×10^{-6}
i_n^2	1.44×10^{-24}	1.329×10^{-15}	7.655×10^{-7}
$\frac{V_n^2}{R_F^2}$	1.08×10^{-26}	9.96×10^{-18}	5.74×10^{-9}

Although they are not depicted in Fig. 3.18, 5 pF capacitors are installed in parallel with feedback resistors R_{11} and R_{12} to suppress feedback oscillations. These capacitors decrease the preamplifier gain at high frequencies because they reduce the feedback impedance. This creates a high-frequency roll-off for many of the noise sources. A roll-off frequency can be estimated by calculating the frequency for which the amplitude of the capacitor impedance equals the resistance of R_{11} or R_{12}, as shown in Eq. (3.81):

$$f_2 = \frac{1}{2\pi\left(24{,}000\ \Omega \times \left[2 \times 10^{-12}\ \mathrm{F}\right]\right)} = 1.32 \times 10^6\ \mathrm{Hz} \tag{3.81}$$

For the correction to G_1, $\omega_2 = 2\pi f_2 t_m = 5.833$, and $\Delta G_1 = 1/\pi\omega_2 = 0.0545$. Combining both corrections, $G_1 = 0.5 - 0.0038 - 0.0545 = 0.4417$. An additional gain of 12 occurs between the first-stage output and the integrator input, which then integrates with a time constant of 2.2×10^{-7} s. Therefore, $\tau = (2.2 \times 10^{-7}\ \mathrm{s})/12 = 1.83 \times 10^{-8}$ s. For noise sources whose spectral density is not frequency-dependent, the effect of applying the operator S (Eq. [3.68]) is to multiply by an effective bandwidth of $(t_m G_1)/\tau^2 = 9.23 \times 10^8$ Hz. The charge delivered by a pulse is $Q = ([V_{I1} + V_{I2}]\tau)/R_F$. To get $V_{I1} + V_{I2} = 1$ V requires $Q = 7.62 \times 10^{-13}$ C for an average current over the integration period of $Q/T = 1.09 \times 10^{-6}$ A. If operation at 300 K is assumed, then the noise multiplier for resistors $C_r = 4\pi(1.38 \times 10^{-23})(300) = 5.20 \times 10^{-20}$ (V^2s)/Ω.

The terms that appear in the formulas for H and J are listed in Table 3.1.

The term C_r/R_W, which is the thermal noise current from the tube wire, dominates. At the center of the wire, using Eq. (3.77), the uncertainty in the position determination evaluates to $P_n = (1/Q) \times (2.381 \times 10^{-15})$ C. For $Q = 7.62 \times 10^{-13}$ C, $P_n = 0.00312$, and Eq. (3.79) yields $V_{I1n} = 0.00327$ V.

3.2.2.5 Experimental Test of Noise from Wire Resistance

A test of some of the predictions about the influence of the tube wire resistance on noise was done, using the detector which was the basis for the previous calculations. For these tests, the tube wire connections to the preamplifiers for channel 1 were altered in various ways. After each alteration, a calibration was performed. During

Table 3.2 Standard deviations

Test	σ_1 (ADC)	σ_2 (ADC)
1	2.35	2.27
2	1.27	1.21
3	2.63	1.25
4	2.09	0.84
5	2.46	2.10
6	1.27	1.65
7	0.71	1.73

this calibration, the values of V_{I1} and V_{I2} were measured approximately 300 times with no pulse present, and the standard deviation of these values was one of the calculations performed. Calling these standard deviations σ_1 and σ_2, the results are shown in Table 3.2. The standard deviations are in units of ADC steps, in which one ADC step is approximately 0.1 V.

For test 1, the tube wire was connected normally. For test 2, the wire was disconnected on side 2 and left floating. This disconnection decreased the noise by nearly a factor of 2. For test 3, the wire was connected directly to the detector ground on side 2. This connection caused the higher noise on side 1 to reappear. For test 4, the power to the preamplifier for side 2 was disconnected. This disconnection was a check to determine if the return currents along the preamplifier power supply ground wires could be driving a ground loop current between the preamplifiers, which is a potential noise source. The noise for side 2 decreased but did not go all the way to 0 owing to noise in the integrator and later preamplifier stages. The noise on side 1 decreased slightly but remained high. For test 5, the side 2 preamplifier power was restored. A 3300 Ω resistor was attached between the side 2 preamplifier input and the preamplifier ground. The tube wire was connected to ground. The noise levels on both sides were close to the levels observed during test 1. Test 5 suggests that the thermal noise current owing to the tube wire resistance dominates over any currents induced by external sources. For test 6, the resistor was increased to 6600 Ω, and the tube wire connection to ground was removed. The noise levels at side 2 decreased, showing that an increased resistance reduces the noise. The side 1 noise was the same as that for test 2, and it had a low value because the tube wire lacked a path through which noise currents could travel. For test 7, the side 1 preamplifier power was disconnected, and the rest of the setup remained the same. The noise on side 2 was very close to the level seen on test 6. Test 7 was performed as a further verification that crosstalk between preamplifiers was not contributing to the noise.

3.2.3 The Attraction of the Central Wire to the Tube Wall for LPSD Tubes

LPSD tubes are constructed as circular tubes with an electrical feedthrough on each end. A small-diameter central wire is suspended under tension between these feedthroughs. This wire must be electrically biased with respect to the tube wall

for the detector to function. For tubes with a high length-to-diameter ratio, a significant failure mechanism is the electrostatic attraction of the wire to the tube wall. If the wire reaches the wall, then a spark will be created, which can be strong enough sever the central wire, ruining the detector. This attraction can be theoretically modeled to gain some insight into the conditions under which it occurs.

3.2.3.1 Electrostatic Attraction of an Off-Center Wire to a Cylindrical Tube

The electrostatic attraction of an off-center wire to a cylindrical tube is calculated using the following simplifying assumptions. Variations in the off-center distance of the wire with the position along the axis of the tube are ignored. Variations in the potential along the axis of the tube are ignored, and the second derivative of any such variations is assumed to equal zero. For these assumptions to be reasonable, any such variations must occur over distances that are large compared with the tube radius. Variations in the angular distribution of charge on the surface of the wire are ignored. For this assumption to be reasonable, the wire diameter must be small compared with the tube diameter.

A straight, infinitely long conducting cylindrical tube of inside radius R_T is assumed to be held at ground potential. Inside this cylinder is a straight, infinitely long wire of radius R_W held at voltage V_B. This wire is displaced by a distance R_D from the center of the tube. A cylindrical coordinate system is defined such that R is the distance from the central axis of the tube, Z is the distance along the axis of the tube, θ is the angle around the axis, and the origin is chosen so that $\theta = 0$ is in the direction of the wire displacement. It is convenient for the analysis to express the wire radius and wire displacement as fractions of the tube radius, so set $w = R_W/R_T$ and $D = R_D/R_T$. Figure 3.26 illustrates the definition of these quantities.

If the wire is at the center of the cylinder, then no charge redistribution is on the tube surface, and the potential distribution around the wire follows the free-space result $V = V_S \ln(R/R_T)$. The ratio R/R_T is chosen for the logarithm so that $V = 0$ when $R = R_T$. V_S must be chosen so that $V = V_B$ when $R = R_W$, implying that $V_B = V_S \ln(R_W/R_T) = V_S \ln(w)$. This creates an electric field $E = -\partial V/\partial R = -V_S/R$. The charge density at the wire surface is $\epsilon_0 E = -(\epsilon_0 V_S)/R_W$, where $\epsilon_0 = 8.854 \times 10^{-12}$ F/m is the electric permittivity. Given the wire circumference $2\pi R_W$, this charge density yields a charge per length given by Eq. (3.82):

$$Q = -\frac{2\pi\epsilon_0 V_B}{\ln w} \tag{3.82}$$

When the wire is offset from the center, its distance R_A to the tube wall varies with θ, as given by Eq. (3.83):

$$R_A(\theta) = R_T\sqrt{1 - 2D\cos\theta + D^2} \tag{3.83}$$

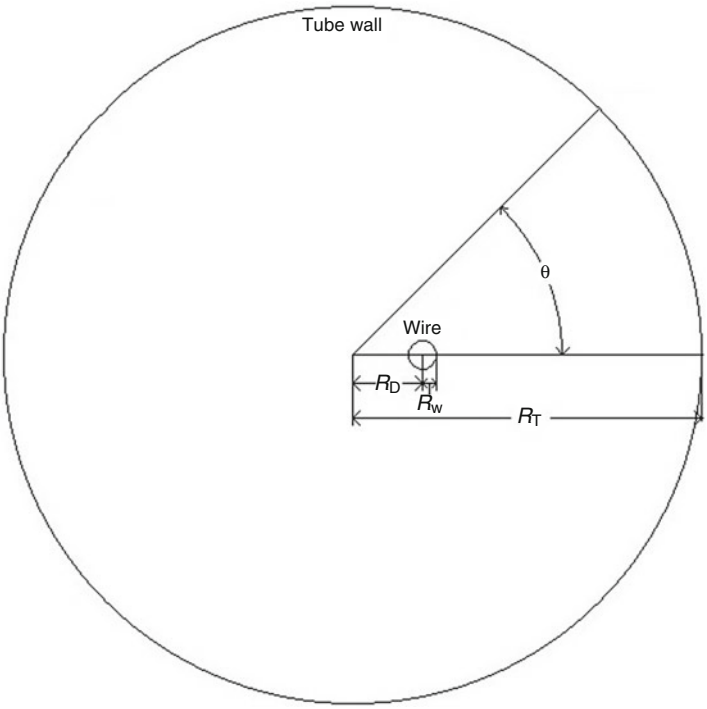

Fig. 3.26 Diagram of a cross section of an LPSD tube, illustrating the definition of several quantities used in the calculations. The z-axis is along the length of the detector tube, rising out of the page. The radius of the central wire is exaggerated in the diagram

If the redistribution of charge at the tube wall was suppressed, then the potential at the tube wall varies with θ, as given by Eq. (3.84):

$$V_1(\theta) = V_S \ln\left(\frac{R_A}{R_T}\right) = V_S \ln\left(\sqrt{1 - 2D\cos\theta + D^2}\right) \tag{3.84}$$

Because the tube is conductive, the surface charge at the tube wall redistributes to create an additional potential of $-V_I(\theta)$, restoring the sum of the potentials to zero. Inside the tube, the potential owing to the redistributed charge is source-free, yielding Eq. (3.85):

$$\nabla^2 V = 0 = \frac{\partial^2 V}{\partial R^2} + \frac{1}{R}\frac{\partial V}{\partial R} + \frac{1}{R^2}\frac{\partial^2 V}{\partial \theta^2} + \frac{\partial^2 V}{\partial Z^2} \tag{3.85}$$

Assuming that $(\partial^2 V)/(\partial Z^2) \approx 0$, voltage can be calculated using Eq. (3.86):

$$V = V_0 + \sum_{n=1}^{\infty} A_n R^n \cos(n\theta) + \sum_{n=1}^{\infty} B_n R^n \sin(n\theta) \tag{3.86}$$

The symmetries of this problem are such that $B_n = 0$ for all n. At the tube radius R_T, Eq. (3.86) must evaluate to the required potential $-V_I(\theta)$, as shown in Eq. (3.87):

$$-V_S \ln\left(\sqrt{1 - 2D\cos\theta + D^2}\right) = V_0 + \sum_{n=1}^{\infty} A_n R_T^n \cos(n\theta) \tag{3.87}$$

Defining coefficients C_n such that $V_0 = V_S C_0$ and $V_S C_n = A_n R_T^n$ forms Eq. (3.88):

$$-\ln\left(\sqrt{1 - 2D\cos\theta + D^2}\right) = C_0 + \sum_{n=1}^{\infty} C_n \cos(n\theta) \tag{3.88}$$

The coefficients C_n are dimensionless, depend only on D, and can be determined by Fourier fitting to this formula.

For $\theta = 0$, electric field is given by Eq. (3.89):

$$E = -\frac{\partial V}{\partial R} = -\sum_{n=1}^{\infty} n A_n R^{n-1} = -V_S \sum_{n=1}^{\infty} n C_n R_T^{-n} R^{n-1} \tag{3.89}$$

For $R = R_D$, Eq. (3.89) evaluates to a field E_D at the wire position given by Eq. (3.90):

$$E_D = \frac{-V_S}{R_T} G(D) \tag{3.90}$$

where $G(D)$ is given by Eq. (3.91):

$$G(D) = \sum_{n=1}^{\infty} n C_n D^{n-1} \tag{3.91}$$

E_D acts on the charge on the wire to create a force per length, given by Eq. (3.92):

$$F = QE_D = \frac{2\pi\epsilon_0 V_B^2}{R_T \ln(w)^2} G(D) \tag{3.92}$$

The remaining evaluation is of function $G(D)$, which is calculated numerically. For a chosen value of D and for $n < 10$, the expression $-\ln\left(\sqrt{1 - 2D\cos\theta + D^2}\right)\cos(n\theta)$ was evaluated at 0.5° intervals. The results were summed to generate the integral needed to evaluate C_n. Then, $G(D)$ can be

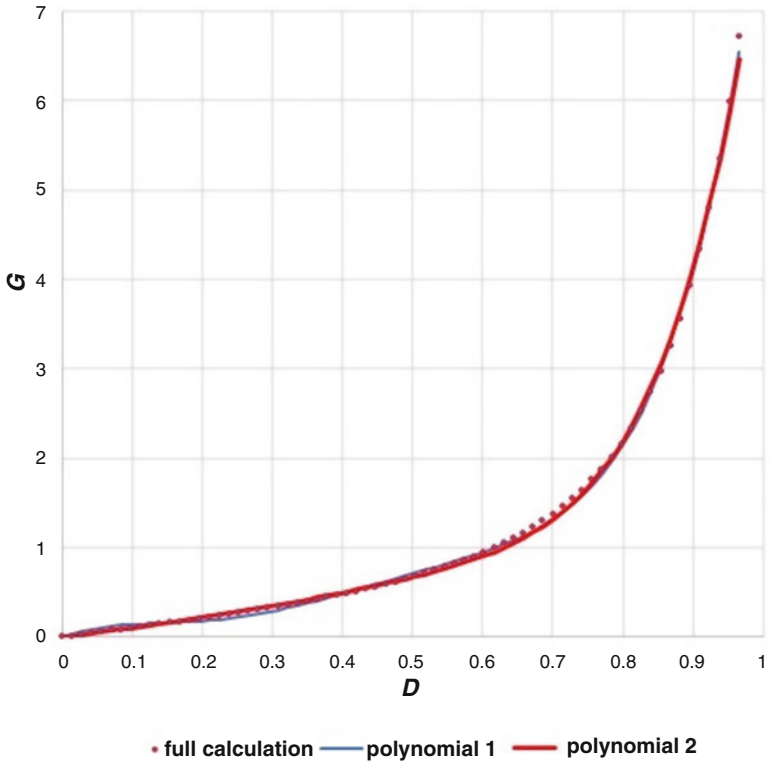

Fig. 3.27 Full-scale plot of $G(D)$

calculated for terms in which $n < 10$. For 70 values of D, $G(D)$ was calculated at intervals of 0.014, covering the range $0 \leq D \leq 0.966$. The results are plotted over the full range in Fig. 3.27 and with an expanded view of the low-amplitude portion in Fig. 3.28. The results were fitted to polynomials to create a less computationally intensive representation. The first polynomial tried was $G(D) = \sum_{n=1}^{5} H_n D^n$, which had fit results $H_1 = 3.0649$, $H_2 = -24.748$, $H_3 = 9.5873$, $H_4 = -14.586$ and $H_5 = 79.954$ and is plotted as polynomial 1 in Figs. 3.27 and 3.28. Although polynomial fitting works well for tracking the behavior at large values of D, the polynomial oscillates around the true values when D is small and is therefore a poor model of the behavior for small values of D. The second polynomial tried is given in Eq. (3.93):

$$G(D) = D + \sum_{n=1}^{3} H_n D^{2n+1} \tag{3.93}$$

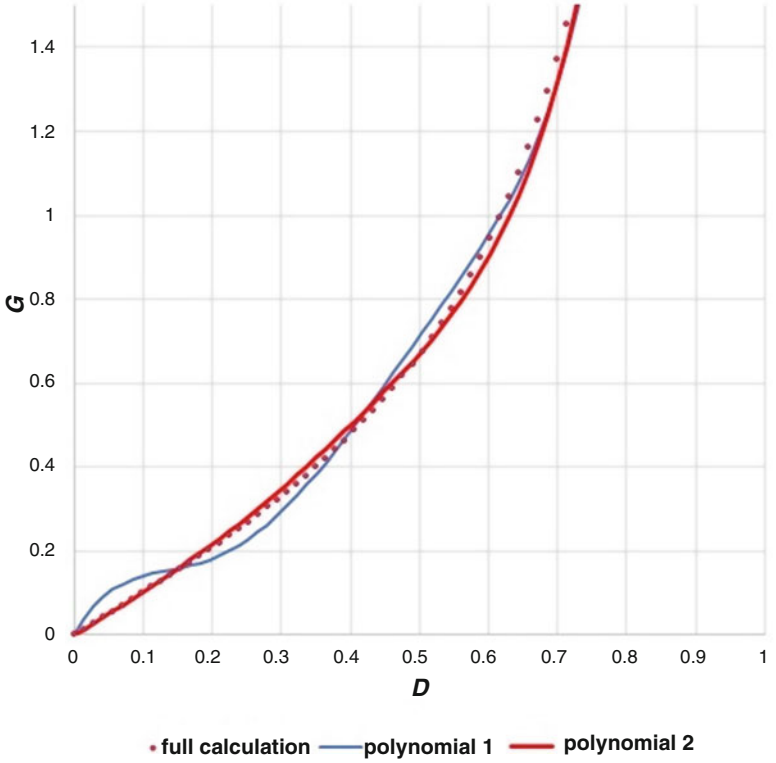

Fig. 3.28 Expanded-scale plot of $G(D)$

which had fit results $H_1 = 2.334$, $H_2 = -6.770$, and $H_3 = 11.564$ and is plotted as polynomial 2 in Figs. 3.27 and 3.28. Polynomial 2 tracks the function well for large values of D and is much better behaved for small values of D compared with polynomial 1.

G(D) is defined in Eq. (3.91). D is a normalized measure of the offset of the wire from the tube center, and G is a normalized measure of the strength of the electrostatic attraction.

3.2.3.2 Wire Deflection in Response to Side Forces

This section's analysis assumes that all side forces remain within a single plane. The z-axis is the line between the feedthroughs of the detector tube, and $z = 0$ is one of the attachment points of the wire to the feedthrough. Then the y-axis is the direction perpendicular to the z-axis that lies in the plane where the side forces are being exerted. The function $Y(z)$ describes the y coordinate of the deflected wire's position. The function $\theta(z)$ describes the angle between the wire and the z-axis direction at

position z. The function $W(z)$ describes the tension in the wire at position z. The function $F_y(z)$ describes the force on the wire from sources other than tension in the y direction per unit length in the z direction at position z, and $F_z(z)$ describes the force on the wire from sources other than tension in the z direction per unit length in the z direction at position z.

A section of the wire between $z = z_0$ and $z = z_0 + \Delta z$ experiences a force in the z direction of $-W(z_0)\cos(\theta[z_0])$ at one side, a force of $W(z_0 + \Delta z)\cos(\theta[z_0 + \Delta z])$ at the other side, and a distributed force of $F_z\Delta z$. For the wire to remain stationary, these forces must add up to zero: $0 = F_z\Delta z + W(z_0 + \Delta z)\cos(\theta[z_0 + \Delta z]) - W(z_0)\cos(z_0)$. For small Δz, $W(z_0 + \Delta z)\cos(\theta[z_0 + \Delta z])$ expands to $W(z_0 + \Delta z)\cos(\theta[z_0 + \Delta z]) = W(z_0)\cos(\theta[z_0]) + (dW/dz)\cos(\theta[z_0])\Delta z - W(z_0)\sin(\theta[z_0])(d\theta/dz)\Delta z$. Using this expansion and dividing by Δz gives Eq. (3.94):

$$0 = F_z + \frac{dW}{dz}\cos\theta - W\sin\theta\frac{d\theta}{dz} \tag{3.94}$$

A similar analysis for forces in the y direction yields Eq. (3.95):

$$0 = F_y + \frac{dW}{dz}\sin\theta + W\cos\theta\frac{d\theta}{dz} \tag{3.95}$$

Adding Eq. (3.94) multiplied by $\cos\theta$ to Eq. (3.95) multiplied by $\sin\theta$ yields Eq. (3.96):

$$0 = F_z\cos\theta + F_y\sin\theta + \frac{dW}{dz} \tag{3.96}$$

Substituting dW/dz from Eq. (3.96) into Eq. (3.94), applying some trigonometric identities, and dividing out a common $\sin\theta$ term yields Eq. (3.97):

$$0 = F_z\sin\theta - F_y\cos\theta - W\frac{d\theta}{dz} \tag{3.97}$$

Because $\tan\theta = dY/dz$, $d^2Y/dz^2 = (1 + \tan^2\theta)(d\theta/dz)$. Therefore, Eq. (3.97) can be rewritten as Eq. (3.98):

$$\frac{d^2Y}{dz^2} = \left(1 + \tan^2\theta\right)\frac{F_z\sin\theta - F_y\cos\theta}{W} \tag{3.98}$$

$E_z(z)$ is defined as the component of the electric field in the z direction at the wire for$z$ coordinate z, and $E_y(z)$ is the component of the electric field in the y direction. $V(z)$ is defined as the voltage present on the wire at z coordinate z. Between a point on the wire (y_0, z_0) and a nearby point on the wire $(y_0 + \Delta y, z_0 + \Delta z)$, $\Delta V = E_y\Delta y + E_z\Delta z = (E_y(dY/dz) + E_z)\Delta z$. Therefore, Eq. (3.99) is written as

$$\frac{dV}{dz} = E_y \frac{dY}{dz} + E_z \tag{3.99}$$

The electrostatic attraction analysis provides an expression for evaluating E_y. Although some E_z component to the field may be present, it is difficult to characterize. The value of E_z is not likely to be large because any charge redistributions driving it will be spread out over the length of the tube; therefore, the approximation $E_z = 0$ can be made. Because E_z is the only source for F_z, F_z can also be set equal to zero. Therefore, for small θ, Eq. (3.100) is written as

$$\frac{d^2Y}{dz^2} = \left(1 + \tan^2\theta\right)\frac{-F_y \cos\theta}{W} = \frac{-F_y}{W\cos\theta} \approx \frac{-F_y}{W} \tag{3.100}$$

To relate this equation to the wire deflection in a detector tube, the y-axis will be associated with the $\theta = 0$ direction in Fig. 3.26. The wire offset from the tube center R_D comes from two sources. One source is the deviation of the wire from straightness, described by the function $Y(z)$. The other source is the deviation of the tube from straightness. Attention will be limited to deviations of the tube in the y-axis direction, with $C(z)$ defined as the deviation of the center of the tube from a straight line between the feedthroughs to which the wire is mounted. The sign convention for $C(z)$ is chosen such that $R_D = Y + C$. Therefore, $D = (Y + C)/R_T$. The source for F_y is the electrostatic attraction of the wire to the tube wall given by Eq. (3.92). Thus, Eqs. (3.101), (3.102), and (3.103) are obtained:

$$\frac{d^2Y}{dz^2} = \frac{-2\pi\epsilon_0 V^2}{WR_T(\ln w)^2} G\left(\frac{Y + C}{R_T}\right) \tag{3.101}$$

$$\frac{dW}{dz} = -F_Y \sin\theta \approx \frac{-2\pi\epsilon_0 V^2}{R_T(\ln w)^2}\frac{dY}{dz} G\left(\frac{Y + C}{R_T}\right) \tag{3.102}$$

$$\frac{dV}{dz} = \frac{-V}{R_T \ln w}\frac{dY}{dz} G\left(\frac{Y + C}{R_T}\right) \tag{3.103}$$

3.2.3.3 Scaling Rule

It is desirable to determine rules for how the deflection of the wire in a detector tube scales with tube construction and operation parameters such as length, diameter, wire tension, straightness, and bias voltage. This determination helps to identify combinations of parameters that pose a risk for catastrophic wire deflection. It also allows results from numerical simulations of wire deflection to be applied to a wider variety of cases.

Parameter $A = 0$ at one side of the tube and 1 at the other side. Parameter $B = 0$ when $Y = 0$ and equals 1 when Y equals the tube radius R_T. Then, $z = LA$ for a tube of length L, and $Y = R_T B$ with

$$\frac{d^2Y}{dz^2} = \frac{R_T}{L^2}\frac{d^2B}{dA^2} \text{ and}$$

$$\frac{dY}{dz} = \frac{R_T}{L}\frac{dB}{dA}.$$

If functions $C_B(A)$ and $V_m(A)$ are defined as

$$C_B(A) = \frac{C(LA)}{R_T} \text{ and}$$

$$V_m(A) = \frac{V(LA)}{V_0}$$

where V_0 is the bias at $z = 0$, then Eq. (3.103) becomes Eq. (3.104):

$$\frac{dV_m}{dA} = \frac{-V_m}{\ln(w)}\frac{dB}{dA}G(B + C_\mathrm{B}) \tag{3.104}$$

Define function $W_m(A)$ as

$$W_m(A) = \frac{W(LA)}{W_0},$$

where W_0 is the wire tension at the feedthrough. Equations (3.101) and (3.102) can be combined to yield

$$\frac{dW}{dz} = W\frac{dY}{dz}\frac{d^2Y}{dz^2},$$

which becomes Eq. (3.105):

$$\frac{dW_m}{dA} = W_m\frac{R_T^2}{L^2}\frac{dB}{dA}\frac{d^2B}{dA^2} \tag{3.105}$$

Then, Eq. (3.101) can be rewritten as Eq. (3.106):

$$\frac{d^2B}{dA^2} = \frac{-2\pi\varepsilon_0 V_0^2 L^2}{W_0 R_T^2(\ln[w])^2}\frac{V_\mathrm{m}^2}{W_\mathrm{m}}G(B + C_\mathrm{B}) = -2\pi\varepsilon_0 K\frac{V_m^2}{W_m}G(B + C_B) \tag{3.106}$$

where

$$K = \frac{V_0^2 L^2}{W_0 R_T^2 (\ln(w))^2} \tag{3.107}$$

which is independent of the distance along the tube and the position of the wire.

Some path is assumed to exist for the wire $B = P(A)$, which satisfies Eq. (3.106) for some choice of V_0, T_0, L, R, w, and $C(z)$. A different set of choices for V_0, T_0, L, R, and w can yield the same value for K, and $C(z)$ can be altered as required to leave C_B unchanged. To within the accuracy that V_m^2/W_m remains unchanged, $P(A)$ still satisfies Eq. (3.106). As long as changes in voltage along the wire are small compared with the applied bias V_0, the value of V_m should remain near 1. As seen in Eq. (3.104), the only tube parameter that affects the determination of V_m is w, and that dependence is weak. W_m is a small correction to the tension on the wire, whose value should remain near 1. As seen in Eq. (3.105), its determination depends on the tube parameter dependent value R_T/L. Although w and R_T/L are terms that appear in Eq. (3.107) for K, their values are not uniquely determined by K. Within the approximation that K independent variations in V_m^2/W_m can be ignored, the wire path B is determined by K and C_B.

3.2.3.4 Numerical Simulation

The length of the wire was divided into 200 equal segments, and arrays were created to list the values of Y, dY/dz, d^2Y/dz^2, C, V, and T at each segment boundary. An iteration cycle used a set of known estimates for d^2Y/dz^2, initially from calculations for an undeflected wire and later from the results of the previous iteration. Starting with $z = 0$, $y = 0$, and an estimate of the slope at $z = 0$ from the previous iteration, the second derivatives were used to extrapolate values for Y and dY/dz to the other end of the wire. This extrapolation was not guaranteed to end up at $Y = 0$ for $z = L$, so a slope correction was then added to all the Y and dY/dz values to force $Y = 0$ at $z = L$. Integrating from $z = 0$, Eqs. (3.102) and (3.103) can be used to determine values of V and T at each segment boundary. Equation (3.101) can then be used to calculate a new set of estimates for d^2Y/dz^2, completing the iteration cycle. Values for $G(D)$ were calculated using polynomial 2 in Figs. 3.27 and 3.28.

Values for the deviation from straightness C were generated from three parameters: the deviation depth D_D, the deviation position P_D, and the deviation length L_D. Equation (3.108) was used in regions where C is positive; $C = 0$ was used elsewhere.

$$C = D_D - \frac{4D_D}{L_D^2}(z - P_D)^2 \tag{3.108}$$

The iterations are not guaranteed to converge on a stable deflection of the wire. If all other parameters are kept the same and only the voltage is varied, then a threshold

voltage is observed. Below the threshold, the wire deviation settles to a stable value. Above the threshold, the deviation increases with each iteration until it encounters the tube wall. For voltages far below the threshold, a small number of iterations is sufficient to converge on a stable deflection. For voltages far above the threshold, the wire reaches the tube wall after a small number of iterations. The number of iterations required becomes large when the voltage is close to the threshold. This threshold likely represents a genuine instability in the wire's behavior, and it can be interpreted as the voltage at which the tube will fail.

3.2.3.5 Simulation Results

The simulation calculations used $L = 1.0$ m, $R = 0.0035$ m, and $R_W = 0.00005$ m (giving $w = 0.01428$). These are typical dimensions for LPSD tubes used in small-angle neutron scattering arrays. A wire tension of 0.115 N was selected to yield threshold voltages consistent with known failures.

A simulation using 100 iterations with an indent position of 0.5 m, an indent length of 0.25 m, an indent depth of 0.00025 m, and bias equal to 1925 V was examined for the variation of the voltage and the tension along the wire. The bias was 1 V under the threshold voltage. The maximum tension observed was 0.115000478 N, a fractional increase of only 4.21×10^{-6}. The maximum voltage observed was 1936.24 V, an increase of 11.24 V, or 0.583%. Changes in wire tension were negligible, and changes in the wire voltage could be considered a small correction, improving the justification for using Eq. (3.48) as a measure of a tube's susceptibility to wire deflections.

A series of threshold voltages for runaway wire deflection were determined while varying the deviation depth and the deviation position. The deviation length was kept at one-fourth of the tube length. Initially, the highest voltage V_{100}, for which the wire does not reach the tube wall after 100 iterations, was determined by varying the voltage in 1 V increments. A sampling of a few cases in which the number of iterations was increased to 1000 revealed that $V_{100} - V_{1000} \approx 4$ V, so $V_{100} - 4$ V was used as a better measure of the threshold voltage. The results are plotted in Fig. 3.29.

A series of threshold voltages for runaway wire deflection were determined while varying the deviation depth and the deviation length. The deviation position was kept at the center of the tube. The results are plotted in Figs. 3.30 and 3.31.

The depth of a deviation from straightness is not by itself sufficient to assess the risk for a tube failure. The position of the deviation along the tube and the length over which it is occurring also have a significant influence.

The threshold voltages are dependent on the detector dimensions and wire tension chosen for the simulation. A more universal way to state the thresholds is in terms of the value of K to which they correspond. Table 3.3 lists the value of K in units of 10^{10} V^2/N for several voltages in the range of interest. The dimensionless quantity $2\pi\epsilon_0 K$, which appears in Eq. (3.106), is also listed.

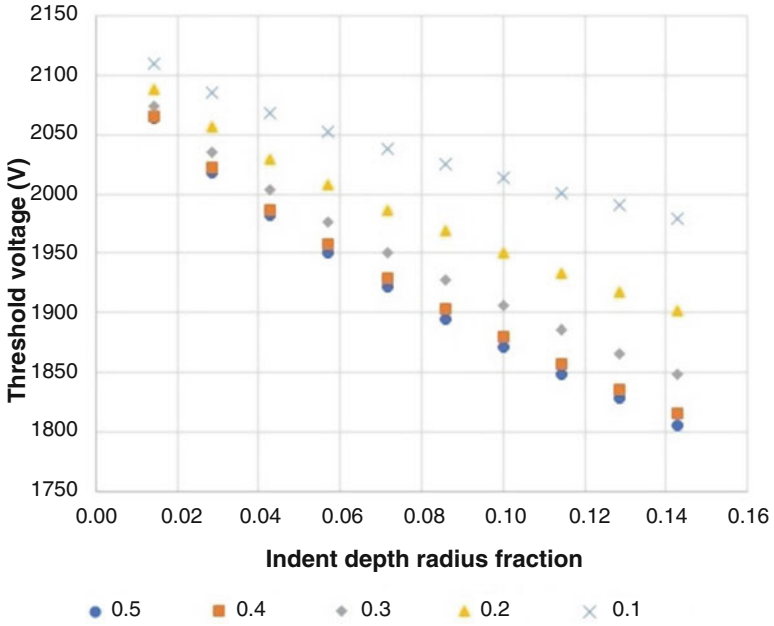

Fig. 3.29 Voltage threshold for runaway wire deflection using an indent length of one-fourth of the tube length. Entries in the legend are the location of the center of the indentation, expressed as the fraction of the tube length from a tube end

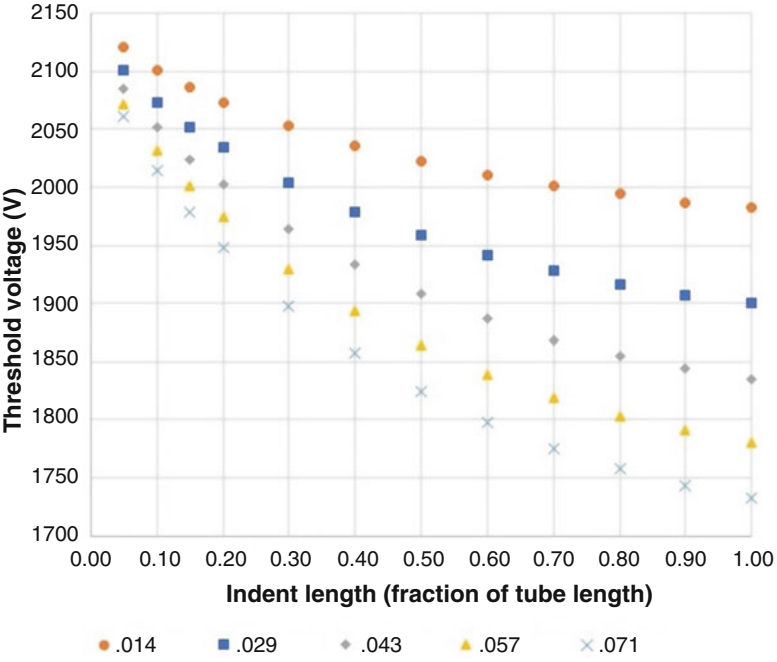

Fig. 3.30 Threshold voltage for runaway wire deflection using an indent position at the tube center. Entries in the legend are the depth of the indentation, expressed as a fraction of the tube radius

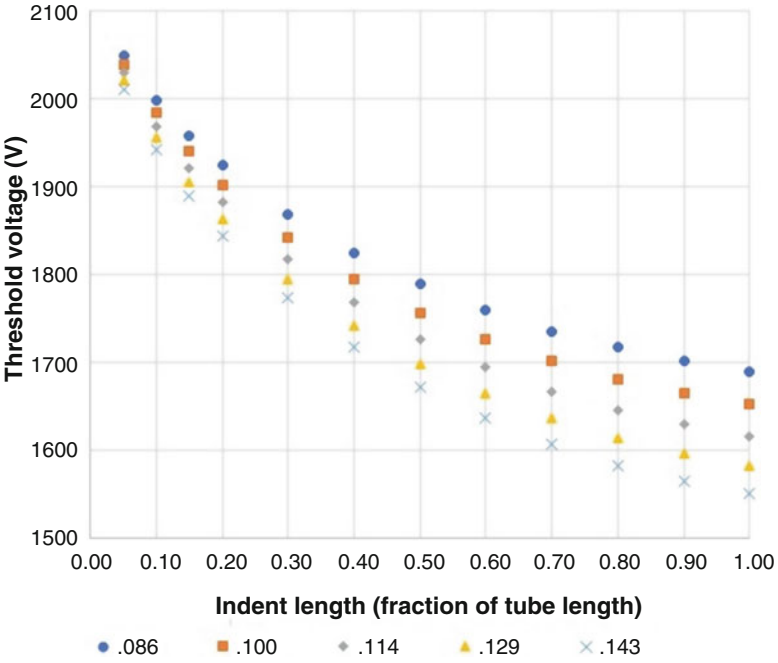

Fig. 3.31 Threshold voltage for runaway wire deflection using an indent position at the tube center. Entries in the legend are the depth of the indentation, expressed as a fraction of the tube radius

Table 3.3 Values of K

Volts (V)	K (10^{10} V^2/N)	$2\pi\epsilon_0 K$
1550	9.448	5.256
1600	10.068	5.601
1650	10.707	5.956
1700	11.366	6.323
1750	12.044	6.700
1800	12.742	7.088
1850	13.460	7.488
1900	14.197	7.898
1950	14.954	8.319
2000	15.731	8.751
2050	16.527	9.194
2100	17.343	9.648
2150	18.179	10.133

3.3 Single-Output Helium-3 Detector Tubes

Helium-3–filled gas-proportional detector tubes can be constructed as position-sensitive detectors or as simple neutron counters. In the first configuration, two outputs are required to provide a way to determine position along the central anode

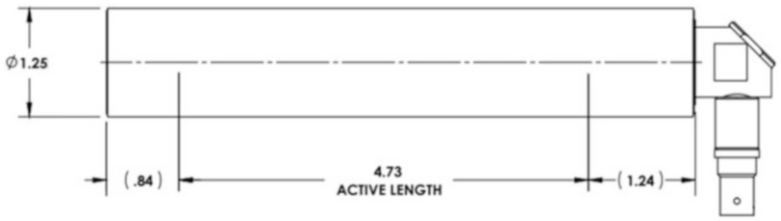

Fig. 3.32 Single-output gas-proportional neutron detector. The anode connector in this example is a right angle–type safe high voltage (SHV) adapter. All dimensions are in inches. (Drawing courtesy of Reuter–Stokes)

wire, either by using resistive charge division or some other method (e.g., time-based encoding using delay lines). If position determination is not required, then a single output suffices. In this instance, the anode wire exits the tube at only one end, and all signal charge is delivered to a single preamplifier. The only information available about the neutron interaction location is that it occurred somewhere within the gas volume.

This section describes the construction and operation of a single-ended ^{3}He detector tube, such as that shown in Fig. 3.32. For the detector in this example, the outer diameter of the tube shell is 3.175 cm (1.25 in.), and the tube length is 17.3 cm (6.8 in.). The enclosed gas is 4 atm of ^{3}He with a trace amount (<0.1 atm) of CO_2 as the quench gas.

An anode wire runs down the center of the tube. Alumina headers electrically isolate the anode wire from the 304 stainless steel outer shell. Two field tubes, one at either end of the anode wire, surround the anode but are of a somewhat larger radius. Referring to Eq. (3.6), a larger inner radius (a) yields a smaller electric field around the field tubes than around the anode wire. This larger inner radius affects a gradual rather than sharp transition region where the electric field decreases to zero, thus minimizing the effect of fringing fields near the ends of the detector active region. The active length, defined as the region between the field tubes, is 12.01 cm (4.73 in.).

The anode wire is accessible outside the tube via a standard right-angle safe high voltage (SHV) type high-voltage connector. Other connector types that can support high voltage, such as Type HN and MHV, may also be used. A biased preamplifier is connected to the anode wire via this connector. The anode is biased to positive high voltage (1350 V in this case) to produce the necessary gas gain. A transimpedance preamplifier with gain equal to 1.8×10^6 V/A provides the output pulses, which are then fed to a counter in the data acquisition system.

The neutron capture efficiency across the tube diameter (within the active region) is shown in Fig. 3.33. This plot shows the efficiency values calculated using Eq. (3.5) (for $\lambda = 2$ Å), scanned across the tube diameter. As expected, the efficiency is greatest at the center, where the diameter, hence the gas depth, is largest, and efficiency diminishes as the gas depth decreases to zero.

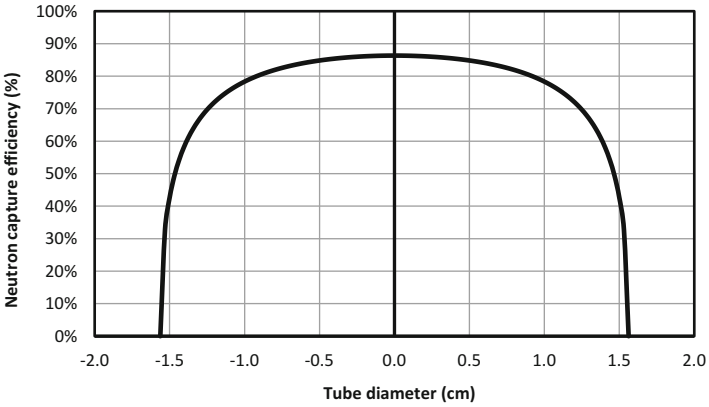

Fig. 3.33 Plot of neutron capture efficiency across the tube diameter. The gas depth, hence efficiency, is greatest at the full diameter (0.0 on the horizontal axis). This plot is for neutron wavelength $\lambda = 2$ Å

Neutrons are absorbed throughout the entire detector active volume. However, interactions that occur very near the inside surface of the tube wall have important ramifications on the distribution spectrum of pulse amplitudes.

For interactions near the wall that occur within the range of either of the reaction products (the proton or triton), the proton or the triton may reach the wall before converting their full kinetic energy into ionization charge. The subsequent signal charge is then reduced by an amount proportional to what was lost to the wall interaction. This reduction is referred to as the *wall effect*.

The wall effect is illustrated by the three examples in Fig. 3.34, corresponding to three different regimes of charge collection, indicated in the pulse amplitude spectrum. In the upper half of Fig. 3.34, the circles represent the cross section of a cylindrical proportional tube, and the anode wire is the dot in the center. The left example represents the case where the proton range exceeds the distance from the neutron interaction point to the wall. If the ^{3}He atom is just inside the surface, then the proton does not contribute to the ionization charge. The resulting signal charge is solely due to the kinetic energy associated with the triton (i.e., $764 - 573 = 191$ keV). As the interaction location moves farther away from the wall, the proton contributes more and more to the ionization charge. This contribution is indicated by the continuum represented by the dotted lines ranging from 191 keV to the full ionization charge of 764 keV. Full ionization charge collection occurs when the interaction location is sufficiently far from the wall that both particles (proton and triton) convert all their respective kinetic energies into ionization. This full ionization is represented by the full-energy peak at 764 keV and the right illustration above the peak.

The example in the center of Fig. 3.34 represents the case where the proton and triton swap roles (i.e., the triton is absorbed by the wall, and the resulting signal charge is reduced by the corresponding ionization deficit). The endpoint in this case,

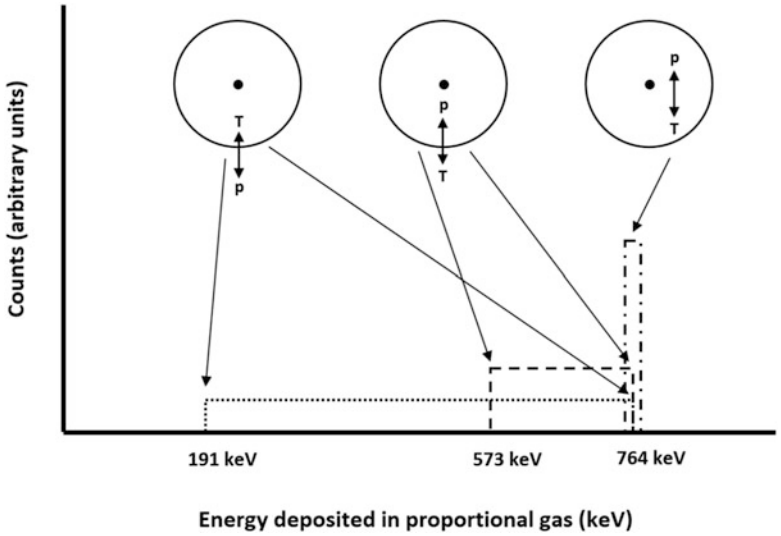

Fig. 3.34 Illustration of wall effect interactions for ^{3}He. T stands for triton, and p stands for proton

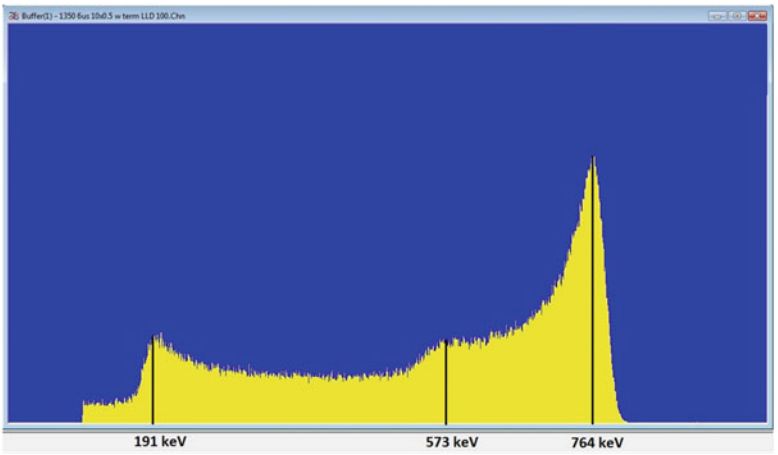

Fig. 3.35 Pulse height distribution for a ^{3}He proportional detector. A low-level discriminator was set to 100 keV (where the distribution abruptly decreases to 0) to reject electronic noise and other non-neutron events from the spectrum

764 keV − 191 keV = 573 keV, occurs when the triton contributes nothing to the ionization charge. The continuum, represented by the dashed lines, ranges from 573 keV to the full energy at 764 keV.

Factors that contribute to the wall effect include gas pressure and composition, tube diameter, and neutron energy (wavelength).

A typical pulse amplitude spectrum for the proportional tube described in this section is given in Fig. 3.35. In practice, electronic noise and other dispersion-

Fig. 3.36 Forty-four single-output tubes comprising a curved 1D detector array. (HB-2A Powder Diffractometer, HFIR)

broadening effects tend to smooth the sharp edges seen in Fig. 3.34, but the essential form is still observed.

Single-ended tubes are used individually (e.g., the triple-axis instruments), or they can be configured as a 1D detector array. The proportional tubes described in this section comprise the curved array at the Neutron Powder Diffractometer instrument at HFIR beamline HB2A. Figure 3.36 is a photo of this array. It consists of 44 single-output tubes, vertically oriented, forming an arc with a radius of 102 cm. Soller-type collimators, one per detector tube, are located just in front of the tubes, pointing toward the sample position to the left in the photo. The green structure is a radiation-shielding monolith, and the three pins support an upper shield plate that is installed during operation.

3.4 Brookhaven National Laboratory 20 cm Multi-Wire Proportional Chamber

An array of 1D position-sensitive detectors can be configured to effectively give 2D, or areal, coverage. One example of this is the ^{3}He-filled gas-proportional LPSD tube. A single tube has position sensitivity in one direction, but when the tubes are placed side by side, a 2D detector array is realized, as illustrated in Fig. 3.37*left*.

However, in this textbook, the terms 2D, or *area*, detectors will refer to a specific class of detector where position encoding exists in two orthogonal directions (e.g., horizontal and vertical). This detector is shown in Fig. 3.37*right*. Often, the two readouts are independent from each other but are combined to provide a 2D map of interaction locations, as determined from the intersection of coincident 1D neutron interactions. Many types of 2D or area detectors exist; in this chapter, the focus is only on those that utilize ^{3}He gas for the conversion medium.

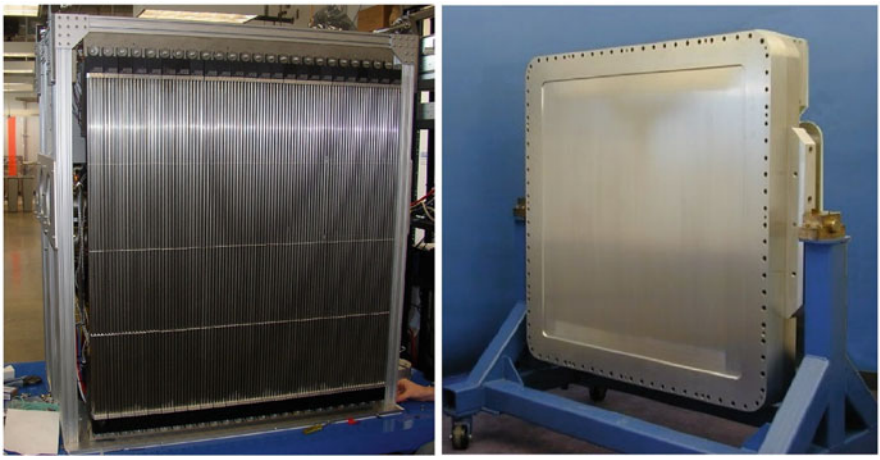

Fig. 3.37 Two methods of achieving 2D, or *areal*, detector coverage. (*left*) A vertical arrangement of individual 1D LPSDs (Reuter–Stokes). (*right*) A detector constructed with true 2D readout (ORDELA, Inc.)

The ^{3}He gas-based area detectors in use at SNS and HFIR can be classified into three types based on the position encoding electronics. The first type was designed and constructed at Brookhaven National Laboratory (BNL) and uses multi-node charge division. The second type was built by DENEX, GmbH and is based on delay line readout. The third type, from ORDELA, Inc., utilizes individual preamplifiers per wire. The BNL detector is described in this section, and the other two types will be described in subsequent sections.

For several decades beginning in the 1970s, the Instrumentation Division at BNL in Upton, NY had a robust program dedicated to research and development of high spatial resolution gas-based neutron detectors [16, 17]. This program was largely in support of the neutron scattering program at the High Flux Beam Reactor, formerly a research reactor on Long Island, NY. Following its shutdown in 1999, 3 of these detectors were made available for use at the SNS. These are multi-wire proportional counters with multi-node charge division and are identical in construction. They are generally referred to as the *Brookhaven detectors* and were among the earliest neutron detectors installed on SNS beamlines. Details of construction and principles of operation are summarized in the following sections.

3.4.1 Details of Construction: Pressure Vessel and Fill Gas

Figure 3.38 shows a photo of the three BNL detectors side by side. To give dimensional perspective, the square regions machined into the 6061-T6 aluminum entrance windows are 20 × 20 cm. This size corresponds with the active region of the detectors. The total enclosed gas pressure is 140 psia, necessitating a machined

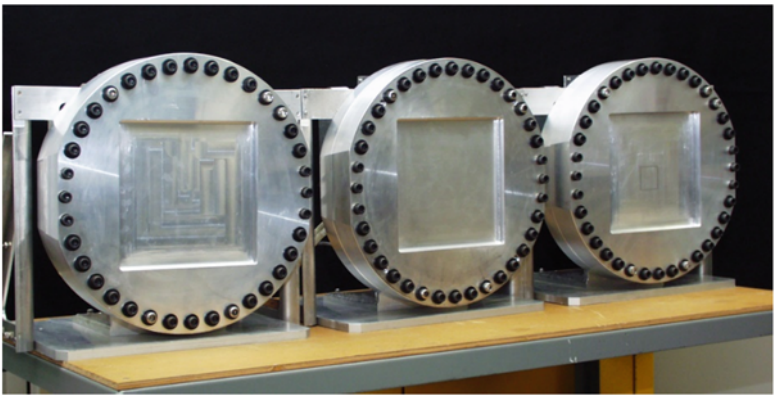

Fig. 3.38 Front view of three 20 cm BNL multi-wire proportional chambers. These detectors were designed and constructed at BNL and delivered to ORNL in 2003 for use in the SNS project

thickness of 9 mm for the aluminum entrance window for minimum deflection under gas load. The detector gas is a mixture of ^{3}He at 100 psia and propane at 40 psia. These partial pressures result from the detection efficiency and spatial resolution requirements. The rationale for these specific values is described in this section.

Helium-3 gas provides the medium for neutron conversion through the nuclear reaction discussed in Chap. 2. Neutron detection efficiency is a function of the total amount of ^{3}He the neutron must pass through; hence, it is related to the product of the gas pressure and gas depth. These detectors were designed to provide a detection efficiency of 80% at 2 Å. Figure 3.39 is a plot of neutron conversion efficiency versus wavelength for a range of ^{3}He gas pressures. This graph is for a gas thickness of 1.5 cm, which corresponds to the gas depth of these detectors. As shown in the figure, this efficiency specification requires a ^{3}He partial pressure just over 6 atm; the Brookhaven detectors contain 6.8 atm (100 psia) ^{3}He gas.

To achieve the desired spatial resolution (<1.5 mm FWHM), the size of the ionization cloud formed during the neutron conversion reaction must be minimized. In the BNL detectors, propane was selected as a stopping gas because of its relatively high stopping power for protons. It has the additional benefit of acting as a quench gas. According to the plot in Fig. 3.40 [19], a propane partial pressure greater than 2 atm provides the proton range necessary to meet the spatial resolution specification. For the BNL detectors, the propane partial pressure is 2.7 atm (40 psia).

The BNL detectors are also equipped with a gas purifier and a gas recirculating pump that operate as a closed-loop system. Electronegative gases, such as oxygen and water vapor, are known to act as electron traps and can degrade detector performance if they are present in large enough concentrations. The gas purifier consists of a stainless cylinder, which is half filled with Ridox (Fisher Scientific; Fair Lawn, New Jersey, USA) and half filled with a 3 Å zeolite molecular sieve. Ridox is an oxygen scavenger, and the molecular sieve adsorbs water vapor. The gas

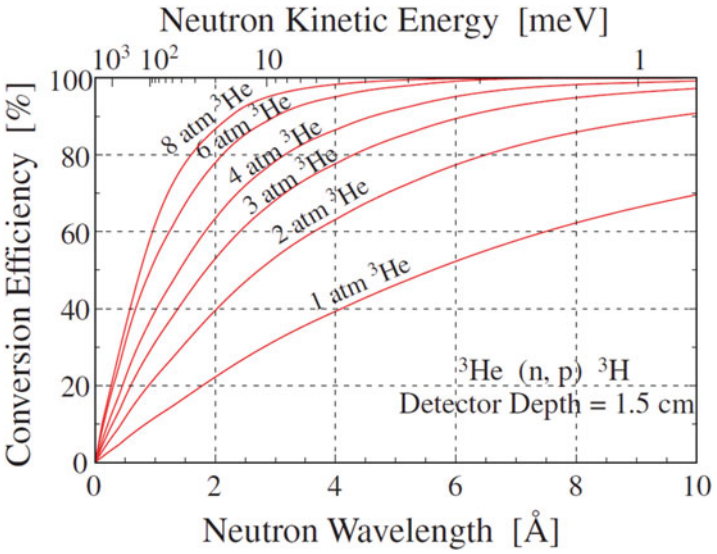

Fig. 3.39 Neutron conversion efficiency versus wavelength for a range of ^{3}He gas pressures. This plot is for a detector depth of 1.5 cm, which corresponds to the BNL 20 cm detectors [18]. Neutron is represented by n, and proton is represented by p

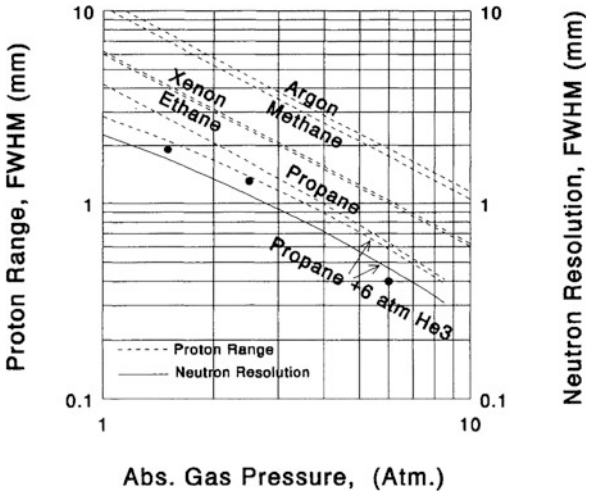

Fig. 3.40 Calculated range of 573 keV protons in various stopping gases as a function of gas pressure (dashed lines). The solid curved line in the middle of the figure represents the calculated neutron spatial resolution for propane combined with 6 atm ^{3}He. The dots are measured data for the spatial resolution with this gas composition [19]

recirculating pump operates continuously by forcing gas through the purifier at a rate of 1–2 L/min. The pump and purifier are identified in the photo in Fig. 3.41.

Two concentric elastomer O-ring seals contain the detector gas. However, these detectors lose gas pressure at an observed loss rate of approximately 3–4 psi/year. The loss of gas pressure results in a noticeable increase in gas gain, which requires a

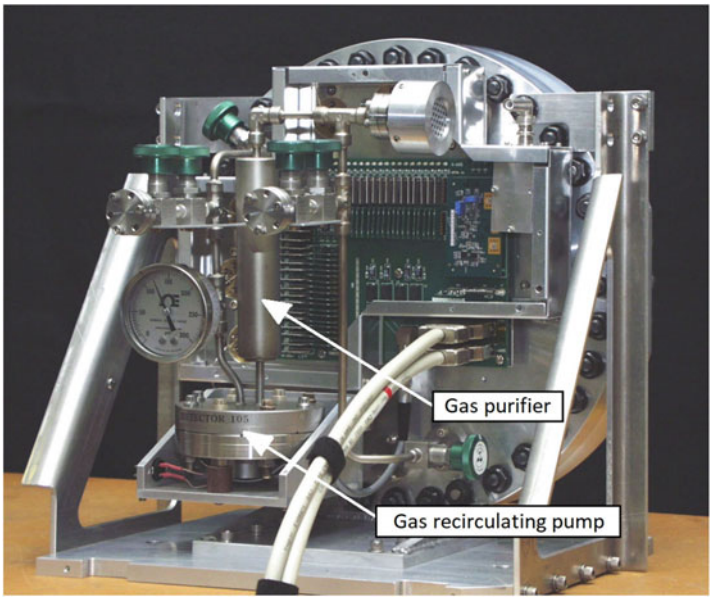

Fig. 3.41 Rear view of the Brookhaven 20 cm detector. The gas recirculating pump and gas purifier are labeled in the figure

periodic (roughly annual) adjustment of the anode voltage to maintain a reasonable anode signal amplitude (i.e., within the range of the sampling ADC). After a period of several years, the gas pressure decreases to the point at which the detector must be restored to original operating conditions. To date this restoration has been achieved by adding only ^{3}He gas under the assumption that the permeation rate of helium far exceeds that of propane.

3.4.2 Details of Construction: Wire Grids and Preamplifiers

Internal electrode construction consists of a single anode grid at positive high voltage sandwiched between two orthogonally oriented cathode grids at ground potential, which are referred to here as the x and y cathode grids. Traversing the detector gas volume from front to back, the first electrode encountered is the y cathode readout grid, then the anode grid, followed by the x cathode readout grid. The spacing between wire grid planes is 1.59 mm (1/16 in.). Figure 3.42 shows a section view of the three grid planes.

The y cathode grid comprises 226 wires, and each wire is 50 μm in diameter. The wires are electrically connected in pairs. The spacing between each wire pair is 1.59 mm (1/16 in.). These wires run horizontally relative to the orientation in Fig. 3.38. Thus, they provide information to determine the y, or *vertical*, coordinate.

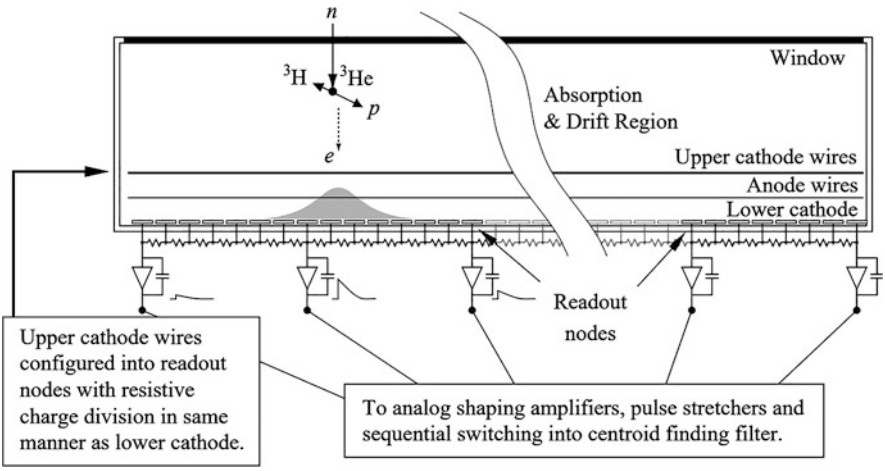

Fig. 3.42 Diagram showing the three grid planes inside the BNL 20 cm detector. The uppermost grid is the *y* cathode wire grid readout, and the bottom grid is the *x* cathode strip grid readout. The anode wire grid is sandwiched between the two cathode grids. Preamplifier readout nodes are connected to every seventh wire or strip. Chip resistors between each wire or strip create a resistive charge division network between preamplifier nodes [20]

At one end of the *y* cathode grid, 15 kΩ chip resistors are soldered between each wire pair to form a resistor chain. A series of charge-sensitive preamplifiers are attached to provide the output of every seventh cathode wire, forming a charge-division network between neighboring preamplifiers. The *y* cathode grid comprises 17 charge-sensitive preamplifiers. The distance between adjacent preamplifiers is 11.1 mm, and the width of the *y* cathode grid is 178 mm.

The anode grid comprises 112 gold-plated tungsten wires, each of a diameter of 12 μm. The wire spacing is 1.59 mm (1/16 in.). These wires run in the same direction (horizontally) and in registry with the wire pairs in the *y* cathode grid. Two guard wires of larger diameter are located on each side (four in total) to reduce electric field fringing at the edges.

The *x* cathode grid is farthest back on the detector, closest to the rear of the detector vessel, and is comprised of 134 vertically oriented copper strips vacuum deposited onto a glass plate. The strip width is 1.016 mm, and the pitch is 1.59 mm (1/16 in.). Like with the *y* cathode grid, 15 kΩ chip resistors are soldered between adjacent strips. A charge-sensitive preamplifier is connected to every seventh strip. Twenty preamplifiers are placed on the *x* cathode grid. The width of the *x* cathode grid is 211 mm.

In addition to these three grid electrodes, a copper coated Kapton drift electrode is attached to the inside of the front entrance window. It is electrically isolated from the detector housing and is negatively biased to provide an adjustable component to set the electric drift field within the detector gas volume.

3.4.3 Principle of Operation

Previously, this chapter described the process by which a neutron is captured in ^{3}He gas. The resulting ionization charge for these detectors is estimated to be approximately 25,000 electron–ion pairs, or 4 fC. The anode grid is positively biased, typically around 2 kV, and the drift electrode is negatively biased at around 1 kV. These two electrodes set the planar electric drift field to approximately 2 kV/cm. The primary ionization charge (electron–ion pairs) drifts through this constant electric field region, with electrons being pulled toward the anode grid and ions toward the drift electrode.

No gas gain occurs in this drift region. As the electrons approach within one wire spacing of the anode wire plane (1.6 mm), the field increases rapidly, approximating the coaxial $1/r$ form very near the wires. Here, the electric field values become sufficiently large that a charge avalanche can occur. These detectors are designed to operate with a relatively low gas gain of approximately 25 to minimize the known detrimental effects on detector longevity from extended high gas gain operation. Thus, the event charge collected at the anode is approximately 100 fC (25 × 4 fC). Less than half of this charge, approximately 40 fC, is induced onto the two orthogonal cathodes and provides the current signal used for position calculations.

An external motherboard contains 37 (20 for the x readout, 17 for y) sets of front-end electronics, namely charge-sensitive preamplifiers paired with signal buffer/driver boards. These boards convert the 40 fC signal charge to a voltage pulse of an amplitude of approximately 100 mV. The boards also provide a 50 Ω differential output to drive these analog signals along shielded, twisted pair cables to the signal-shaping and digitizing electronics. Figure 3.43 shows a picture of this motherboard. The preamplifiers and buffer/driver boards are identified in the photo. A detailed description of the detector front-end electronics is found in [21].

The charge signal from the anode grid is sent to a discriminator circuit. When the anode signal exceeds a programmed threshold, the anode trigger module initiates the data collection process, and the outputs from all 37 preamplifiers are individually digitized in 12-bit ADCs (1 per channel). The channel with the largest amplitude is identified, and the signal charge from it and its two adjacent neighbor channels are used in the calculation of the neutron interaction location, which is based on Eq. (3.109).

This operation is performed separately and independently for the x and y cathode grids. The individual x and y positions are combined in software to provide an (x, y) coordinate pair for each event and a time stamp coincident with the firing of the discriminator. The entire process occurs within an event processing time of just over 4 μs.

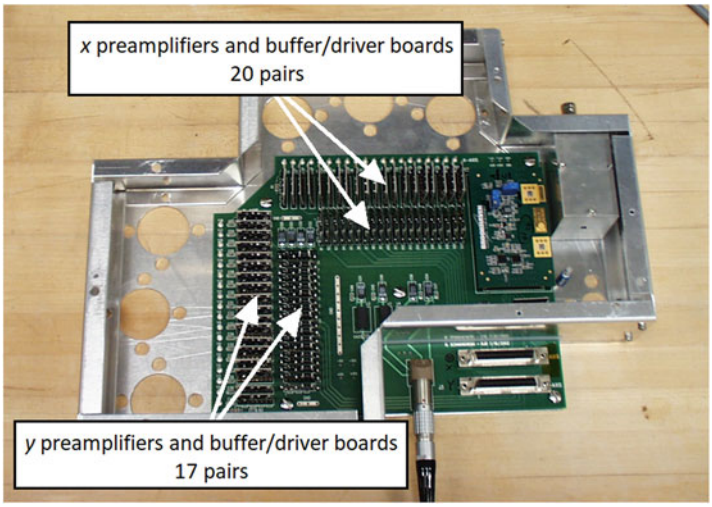

Fig. 3.43 Front-end electronics motherboard with rows of *x* and *y* preamplifiers and buffer/driver boards. In the lower right corner of the photo, two 50-pin signal connectors and the power input cable are also shown. The motherboard is installed on the rear of the gas detector, as seen in Fig. 3.41

The BNL detector is designed such that the signal charge is collected on two or (at most) three cathode wires (or strips). The mathematics of the position calculation is described in the following eqs.

B represents the measured charge in the channel with the largest charge signal. *A* and *C* represent the measured charge in the two channels adjacent to *B* (one on each side). The calculation is performed using Eq. (3.109):

$$P = \frac{C - A}{A + B + C} \tag{3.109}$$

The 210 kΩ resistance chain (15 kΩ × 14) between preamplifiers *C* and *A* is treated as a resistive charge-division network. The value of *P* ranges from −1 to +1, depending on the relative strengths of charges *A*, *B*, and *C*. A few examples are evaluated in the following three cases.

In case 1, if the neutron event is centered over *B*, then $A \approx C$, and $P = 0$.
In case 2, if the neutron event is midway between *B* and *C*, then $B \approx C$, $B \gg A$, and $C \gg A$. For this case, $P = C/(B + C) = +0.5$.
In case 3, if the neutron event is midway between *A* and *B*, then $P = -0.5$ (using the same argument as case 2).

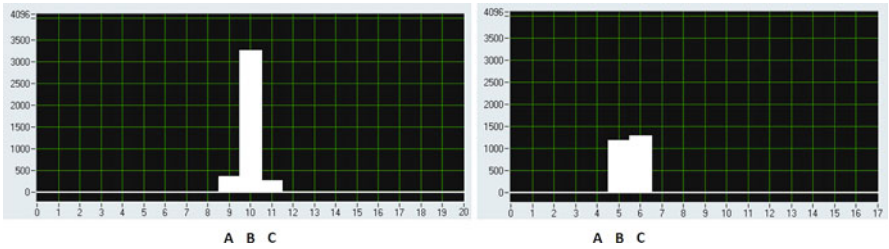

Fig. 3.44 Images illustrating the concept of position determination using two or three adjacent preamplifier outputs. The left figure shows the induced signal charge centered over preamplifier B ($A \approx C$, case 1 in the text), and the right figure shows induced signal charge midway between preamplifiers B and C ($B \approx C$, with $B \gg A$ and $C \gg A$, case 2 in the text) [22]

As Eq. (3.109) suggests, P can take on a continuum of values. When the neutron event location approaches A (or C), it then becomes the dominant charge output, and the wire assignments for A, B, and C all shift one wire over, but Eq. (3.109) is otherwise evaluated in the same way.

Once P is determined and assigned to its associated preamplifier channel (along either the x or y direction), the specific pixel is defined. The denominator is the summed charge from all three preamplifiers (A, B, and C) included in the expression to normalize the value to account for any variation in total signal charge. Representative examples of this calculation are illustrated in Fig. 3.44.

A neutron-absorbing pinhole and slit mask was constructed from 5 mm thick boron-doped aluminum. Figure 3.45 shows the hole and slit dimensions of this mask and the 2D neutron image through the mask. Figure 3.45 clearly shows the fine spatial resolution of this detector.

3.5 Brookhaven National Laboratory 120° Curved Multiwire Proportional Chamber

In 2002, BNL delivered a curved, 2D multiwire ^{3}He gas-proportional detector to Los Alamos National Laboratory to be installed on the new Protein Crystallography Station flight path FP15 at the Los Alamos Neutron Science Center. It utilized essentially the same internal design, construction, and operational parameters as the 20 cm multiwire proportional detectors but this time incorporating eight curved readout grids to create a seamless active area approximately 20 cm high and 150 cm wide, spanning a 120° arc with the radius of the curvature equal to 70 cm. This detector remained in operation at the Protein Crystallography Station from 2002 until the instrument was scheduled for decommissioning in 2015, and then it became available to the neutron scattering user program at ORNL. An instrument upgrade project was initiated and approved to (1) transport the detector to ORNL and (2) upgrade the data acquisition interface to be compatible with the standardized

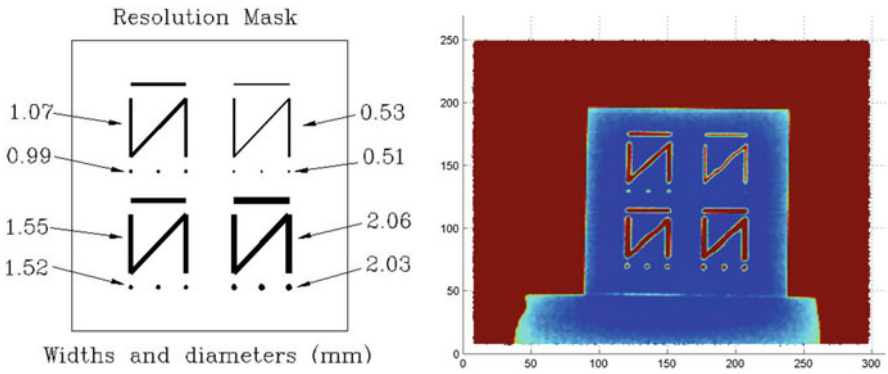

Fig. 3.45 The drawing on the left shows the dimensions of pinholes and slits in the neutron absorbing mask (5 mm thick borated aluminum) used to produce the image on the right

EPICS-based software platform used at SNS and HFIR. Staff from Los Alamos National Laboratory and BNL were integral to the success of this project. The 120° curved multiwire proportional chamber (MWPC) is one of two such BNL-built detectors in existence—the other one is currently in operation at the Wombat powder diffractometer at the Australian Nuclear Science and Technology Organisation.

3.5.1 Details of Construction: Pressure Vessel and Fill Gas

Owing to the much larger window area compared with the 20 cm detectors, the main detector housing was constructed from a higher strength aluminum alloy (7075-T6). The tensile strength of 7075-T6 is 73,000 psi compared with 40,000 psi for 6061-T6, which was used for the 20 cm detectors. The entrance window is 8 mm thick. The upper flange plate is made from 304 stainless steel and contains the feedthrough flanges for the preamplifiers and the high voltage inputs. Two gas recirculating pump and purifier assemblies are attached to the detector body (one at either end). These components are shown in Fig. 3.46. For the reasons outlined in Sect. 3.4.1, the gas composition and pressure are the same as for the BNL 20 cm detectors (i.e., ^{3}He at 100 psia and propane at 40 psia).

3.5.2 Details of Construction: Wire Grids and Preamplifiers

The readout grids are of essentially the same design as the 20 cm detectors (i.e., horizontal and vertical wires and strips). For ease of construction, the 120° readout grid structure was subdivided into eight identical segments, each subtending 15°

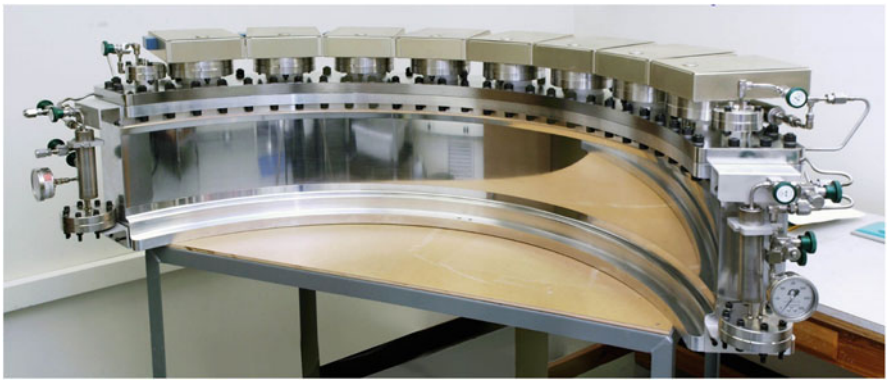

Fig. 3.46 The BNL 120° multiwire proportional detector [18]

horizontally and 15° vertically (relative to the 70 cm radius of curvature). Like the 20 cm detectors, each segment consists of an anode grid in between two orthogonal cathode grids.

However, the requirement for a curved, seamless readout led to a significant design change compared with the planar wire and grid construction used in the 20 cm detectors. Specifically, the curved wire and grid assembly required swapping the orientation of the cathode wires and strips. For the 20 cm detectors, the vertical copper strips defining the *x*-axis readout were furthest from the entrance window so as not to impede charge transport to the anode grid. The much-less-intrusive horizontal wires defining the *y*-axis were located closer to the front of the detector. Rather than attempt a horizontal curved wire design, the readout grid for the 120° detector consists of horizontal copper strips on a curved substrate for the vertical (*y*-axis) readout, which is located furthest from the entrance window, and the less-intrusive vertical wire grid for the *x*-axis readout is closer to the entrance window. The anode wires are vertically oriented and in registry with the *x*-axis cathode wire grid.

The front cathode grid comprises 120 wires, each 50 μm in diameter on a 1.59 mm (1/16 in.) wire pitch. These wires are vertically oriented, thus providing information to determine the *x*, or horizontal, coordinate. The chip resistors are 11 kΩ. Charge-sensitive preamplifiers are attached to provide the output of every eighth cathode wire. This setup forms an 88 kΩ charge-division network between adjacent preamplifiers. The *x* cathode grid comprises 15 charge-sensitive preamplifiers (per segment).

The anode grid consists of 120 gold-plated tungsten wires, each with a 15 μm diameter. The wire spacing is 1.59 mm (1/16 in.). These wires run in the same direction (vertically) and in registry with the *x* cathode grid.

The *y* cathode grid, which is closest to the rear of the detector vessel, comprises 129 horizontally oriented copper strips on a ceramic substrate. The strip width is 1.016 mm, and the pitch is 1.59 mm (1/16 in.). The *y* cathode grid uses 6.25 kΩ chip

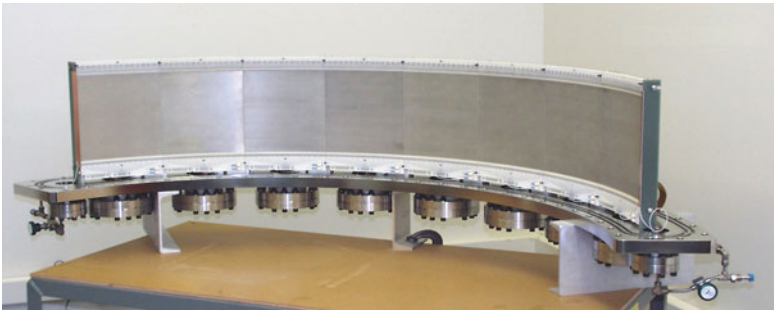

Fig. 3.47 Photo of the eight-segment wire and strip readout assembly [23]

resistors between adjacent strips. Charge-sensitive preamplifiers are present every eighth strip. Along the *y* cathode grid are 17 preamplifiers (per segment).

All eight segments abut to produce a continuous and seamless detection response over the entire 120° span. Figure 3.47 shows a photo of the eight-segment readout grid assembly.

3.5.3 Principle of Operation

Functionally, each of the eight segments has its own dedicated, parallel, and identical signal processing electronics such that the 120° detector operates like eight individual detectors. Thus, detector operation is largely the same as for the 20 cm detectors that are described in Sect. 3.4.3. The main difference is in how the boundaries between segments are treated. Figure 3.48 illustrates how the physical interface between two adjacent segments is realized. The distance between each vertical boundary wire and the substrate edge is half the wire pitch, so when two adjacent segments are abutted side by side, the interwire spacing is maintained across the boundary. Each boundary anode wire is bussed to its neighboring boundary anode wire in an adjacent detector segment and connected to a separate boundary anode preamplifier. When an event is triggered by the anode boundary preamplifier, the leftmost *x* boundary cathode (as viewed from the sample position) is disabled, and the rightmost *x* boundary cathode wire is used for the edge position calculation. Only enabling the rightmost *x* boundary cathode avoids double counting at the segment boundary. The principles of operation outlined in Sect. 3.4.3 Principle of Operation are otherwise applicable for the 120° detector as well.

Figure 3.49 shows a powder diffraction pattern from a silicon sample. The 120° coverage enables simultaneous data collection of the forward and backward scattered Debye–Scherrer cones.

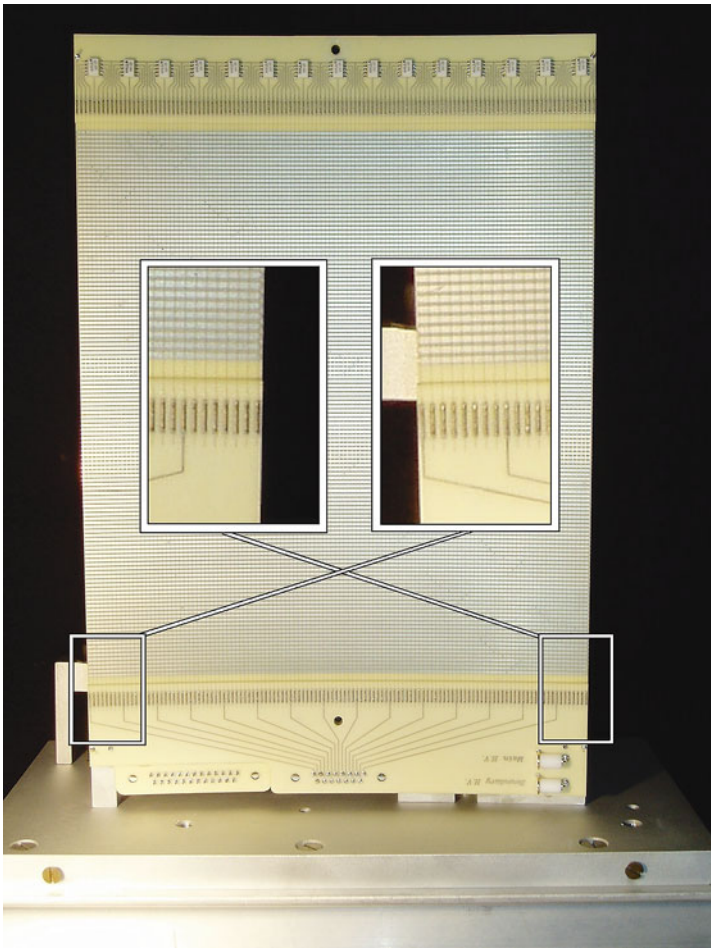

Fig. 3.48 Photo of one of the 8 readout segments seen in Fig. 3.47. In this view, the wires run vertical and the strips run horizontal. A portion of the left and right edges are seen in the two insets. When two of these segments are abutted side by side, both the vertical wire pattern and horizontal strip pattern are reproduced across the interface, generating a seamless readout [24]

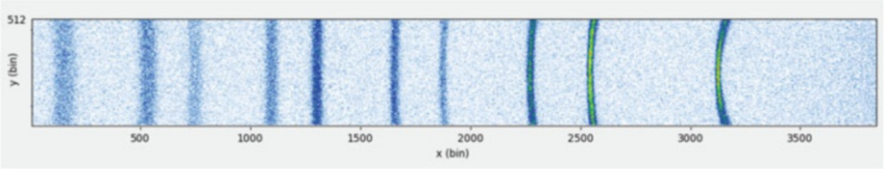

Fig. 3.49 Diffraction pattern from a powdered silicon sample [25]

3.6 Denex Delay Line Detector

The DENEX model DNX-300TN is a ^{3}He-filled neutron detector that utilizes delay line encoding for position determination. Unlike charge-division readout, delay line detectors rely on a comparison of the relative arrival times of the current signals along a 1D line. Combining the results from two orthogonal delay lines provides the (x, y) coordinate pair, which defines the neutron interaction location.

3.6.1 Details of Construction: Pressure Vessel and Fill Gas

Figure 3.50 shows the front view of the detector vessel. The aluminum front plate is machined thinner in the region defining the active area, consistent with the competing needs of containing the pressurized gas with minimal deflection in the entrance window and minimizing neutron scattering from the aluminum. The window thickness is 10 mm, and the machined recess is 30 × 30 cm.

The detector fill gas consists of ^{3}He at a pressure of 4 bar and CF_4 at 2 bar. US Department of Transportation regulations restrict the transportation of noncompliant pressurized gas vessels above a gauge pressure of 2 bar; therefore, the DENEX detector was shipped to ORNL with only the 2 bar (absolute) of CF_4 gas (99.99%

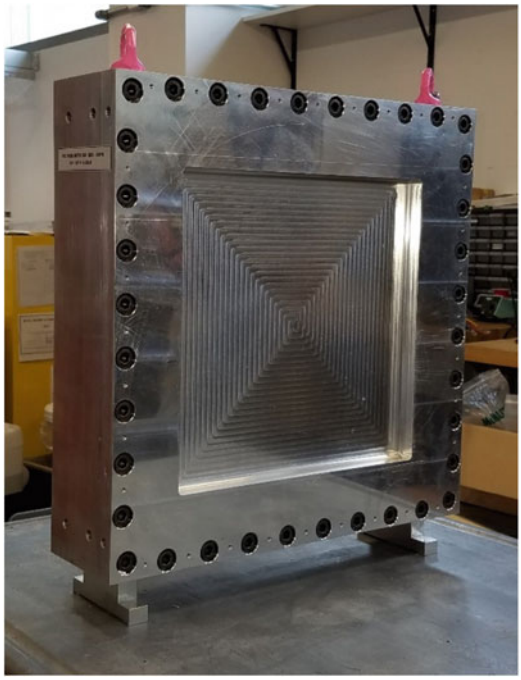

Fig. 3.50 Front view of the DENEX model DNX-300TN neutron detector. The active area is 30 × 30 cm, indicated by the machined recess in the aluminum entrance window

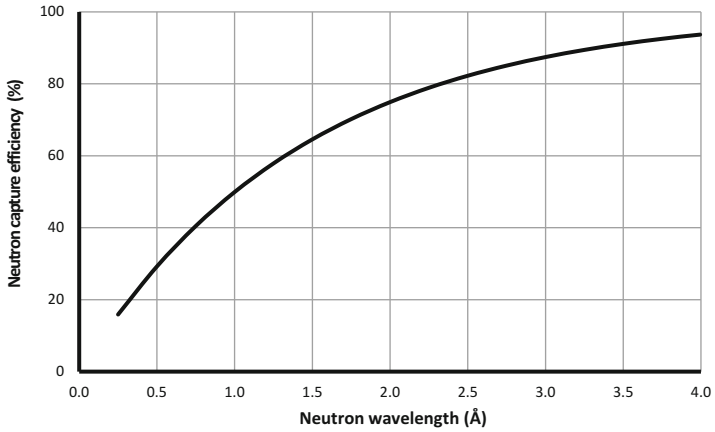

Fig. 3.51 Neutron conversion efficiency of the DENEX-300TN as a function of neutron wavelength

pure). The ^{3}He gas (99.999% pure) was added once it arrived on site. As previously discussed, ^{3}He gas is for neutron conversion, and CF_4 serves as both the quench and the stopping gas. The neutron efficiency versus wavelength curve for this ^{3}He gas pressure (4 bar) and gas depth (22 mm) is shown in Fig. 3.51.

The DENEX detector utilizes an all-metal seal (indium foil) to contain the pressurized gas; thus, loss of gas pressure is expected to be practically nonexistent. A pressure sensor is installed on the detector vessel to give a reading of detector fill gas pressure. This sensor is shown in the detector rear view in Fig. 3.52. The pressure sensor output drifts slightly with changes in room (and detector) temperature, but no decrease in pressure has been observed during the several years that the detector has been in operation.

3.6.2 Details of Construction: Wire Grids and Preamplifiers

The internal construction of the DENEX delay line detector consists of an anode grid at positive high voltage sandwiched between two orthogonally oriented cathode grids at ground potential. Delay line detectors rely on a comparison of the relative arrival times of the current signals at either end of a 1D (x or y) cathode. Signal propagation speeds in metallic wires are generally much too fast for any meaningful separation of these two signals in time, so they must be slowed for delay line detectors to operate effectively. In the case of the DNX-300TN, this propagation delay is achieved via a network of discrete LC (inductor/capacitor) elements along both the horizontal (x) and vertical (y) axes.

Preamplifiers are attached at the ends of each propagation delay line—two for x and two for y—to measure the relative arrival times of these current pulses. The neutron position is determined by examining the relative timing of these pulses.

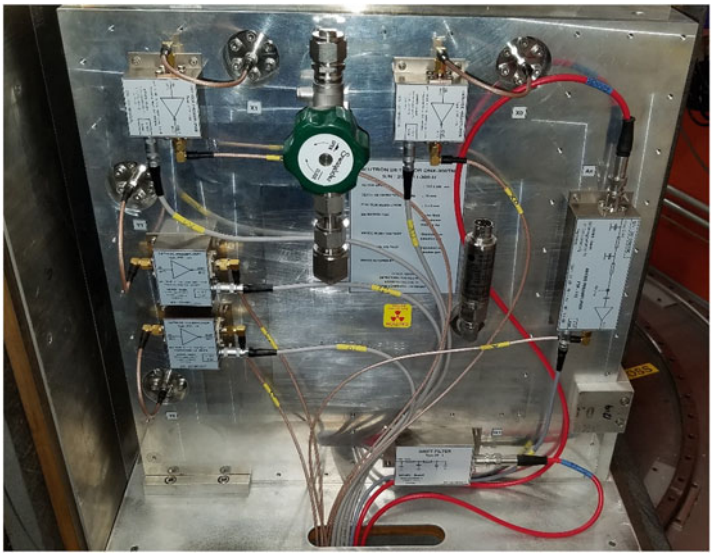

Fig. 3.52 Rear view of the DENEX model DNX-300TN neutron detector. The gas fill valve is just left of center, and the pressure sensor is just right of center. The anode and cathode preamplifiers and high-voltage filters are inside the white labeled boxes

Position determination is performed independently for x and y channels, and the intersection determines the coordinate. A fifth preamplifier records the output of the current signal on the anode grid and acts as the T_0 trigger on which to base the time measurements. These five preamplifiers (two for x, two for y, and the anode) are shown in the detector rear view in Fig. 3.52.

A drift electrode is epoxied to the inside of the front entrance window. It is a layered aluminum and Teflon assembly that is negatively biased (−1200 V) to help set the electric drift field. It is electrically isolated from the detector vessel housing.

The y cathode is located 5 mm from the inside surface of the entrance window. It consists of 300 horizontally oriented wires on a 1 mm pitch. The cathode wires are 30 μm diameter gold-plated tungsten/rhenium at ground potential. LC delay components connect each adjacent wire, yielding a roughly 1.7 ns delay between wires. This delay forms the vertical delay line. The summed propagation delay over the entire 299 mm length of the y cathode is 508 ns. Two preamplifiers are attached to the y delay line, one at either end. The y cathode acts as a 1D PSD.

The anode grid is located 5 mm behind the y cathode. It consists of 150 horizontal wires on a 2 mm pitch. The anode wires are also gold-plated tungsten/rhenium but with a 12 μm diameter. The anode wires are bussed together and connected to a single preamplifier output. The anode grid is positively biased (+4000 V) during operation.

The x cathode sits 5 mm behind the anode grid. It is identical in construction to the y cathode, but here, the wires run vertically. Like the y cathode, the x cathode has two preamplifiers, one at either end of the horizontally oriented delay line, which also act as 1D position-sensitive detectors independently from y.

3.6.3 *Principle of Operation*

Like the other detectors in this chapter, the process of neutron detection begins with neutron conversion in the ^{3}He gas, resulting in a primary ionization charge. The positively biased anode grid and the negatively biased window electrode create an electric drift field to separate the charges. The electrons drift toward the anode, where gas gain begins to occur at roughly 2 mm from the anode wire grid. Current signals are induced on the nearest *x* and *y* cathode wires.

These current signals travel to the ends of the delay lines, divided according to the line impedance between the interaction point and the nearest preamplifier. The line impedance is proportional to the length of delay line, which allows the position determination to be realized. These four cathode preamplifier signals, two each for *x* and *y*, are sent to the five-channel main amplifier along with a charge signal from the anode grid. The main amplifier provides voltage gain. An oscilloscope image of the four cathode preamplifier outputs is shown in Fig. 3.53.

The five signals from the main amplifier are individually fed into a constant fraction discriminator (CFD) for a more precise pulse time determination. Because pulses of different amplitude often have different rise times, threshold triggering is

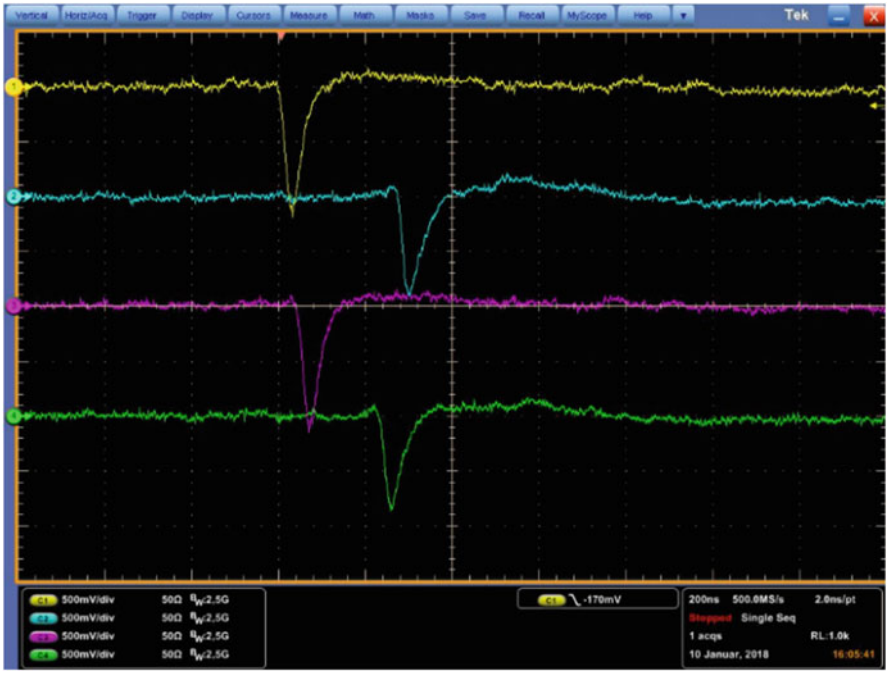

Fig. 3.53 Oscilloscope traces from the four preamplifier outputs (two for *x* and two for *y*) of the DENEX-300TN detector. The vertical scale is 500 mV/division, and the horizontal scale is 200 ns/division

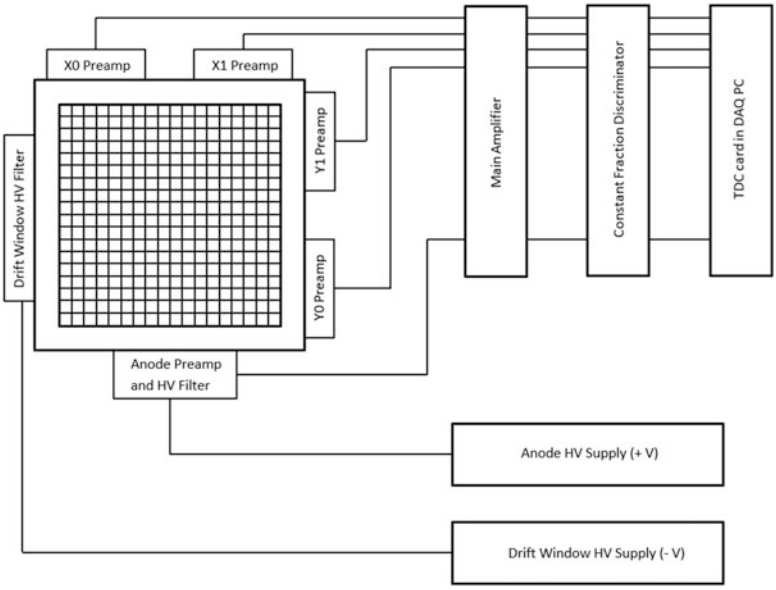

Fig. 3.54 Component and cabling diagram of the signal processing chain. Signals from the four cathode preamps (two for *x* and two for *y*) and the anode preamp are fed to a main amplifier, followed by a constant fraction discriminator, then to a time-to-digital convertor (TDC) card (installed in the data acquisition computer) for timing analysis, which allows for position determination

not a practical technique for applications in which precise timing is required. The role of the constant fraction discriminator is to identify a fixed fraction of the rise time for each pulse, independent of pulse amplitude.

A step-pulse timing signal is then delivered from the constant fraction discriminator to a time-to-digital convertor card (one for each preamplifier) to calculate the propagation time along each axis. From this propagation time, the location along both the *x* and the *y* axes is determined. The neutron interaction location is defined by the intersection of the independent *x* and *y* measurements. Figure 3.54 shows a layout of the main components in the signal processing chain.

As an illustration of the capabilities of this detector, the powder diffraction image from a sample of NAC ($Na_2Ca_3Al_2F_{14}$) is shown in Fig. 3.55. The detector is located at approximately $2\theta = 90$-degrees, hence both forward and backscattered Debye-Scherrer cones are visible in the image.

3.7 Ordela Preamplifier per Wire Detector

The ORDELA model 2410N detector is a ^{3}He-filled 2D position-sensitive proportional counter, which incorporates a preamplifier per cathode wire design. The detector active volume is a 40.6 × 40.6 × 2.5 cm gas depth. This detector was

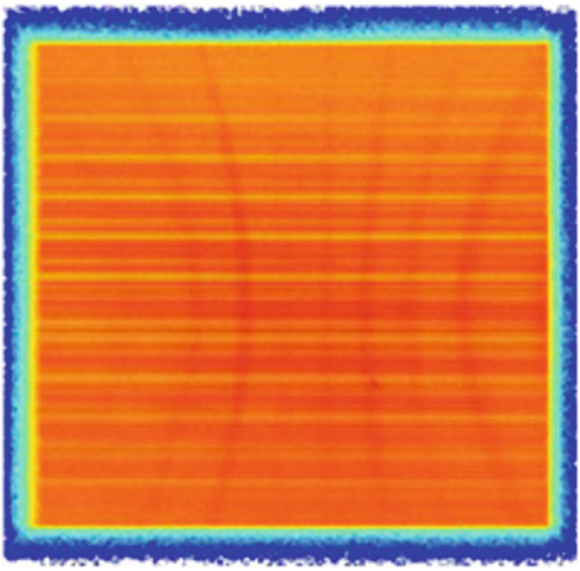

Fig. 3.55 Powder diffraction from NAC sample ($Na_2Ca_3Al_2F_{14}$)

originally built for the Intense Pulsed Neutron Source (IPNS) at Argonne National Laboratory, but it was brought to ORNL following the closure of the IPNS in 2008.

3.7.1 Details of Construction: Pressure Vessel and Fill Gas

The ORDELA 2410N is shown in Figs. 3.56 and 3.57. The pressure vessel is constructed from 6061-T6 aluminum, and the entrance window is machined to a thickness of 10 mm to define the active area of 40.6 × 40.6 cm. The detector gas composition is 1.78 atm ^{3}He plus 0.80 atm CF_4, which provides a nominal 50% detection efficiency at 2 Å. The signal processing electronics, power supplies, and cabling are in an electronics compartment located directly behind the detector, which can be sealed with an air-tight cover for vacuum operation.

3.7.2 Details of Construction: Wire Grids and Preamplifiers

The internal construction consists of three multiwire electrode grids: two orthogonal cathodes at ground potential and one anode grid at positive high voltage. Like the other multiwire designs, the anode grid is positioned between the two cathode grids. Traversing from front to back, the first grid is the *y* coordinate cathode, located 0.75 cm from the inside surface of the entrance window. The *y* cathode grid consists of 128 active wires and an additional 3 wires at each end of the grid (6 total), which

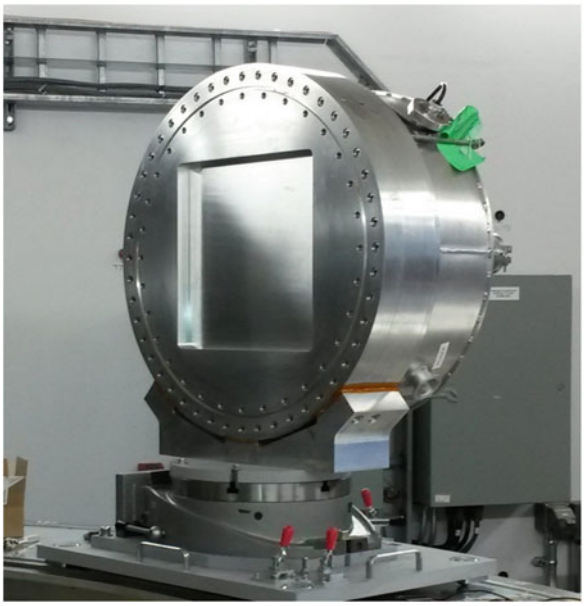

Fig. 3.56 Front view of the ORDELA 2410N detector. The 40.6 × 40.6 cm entrance window is machined to a thickness of 10 mm

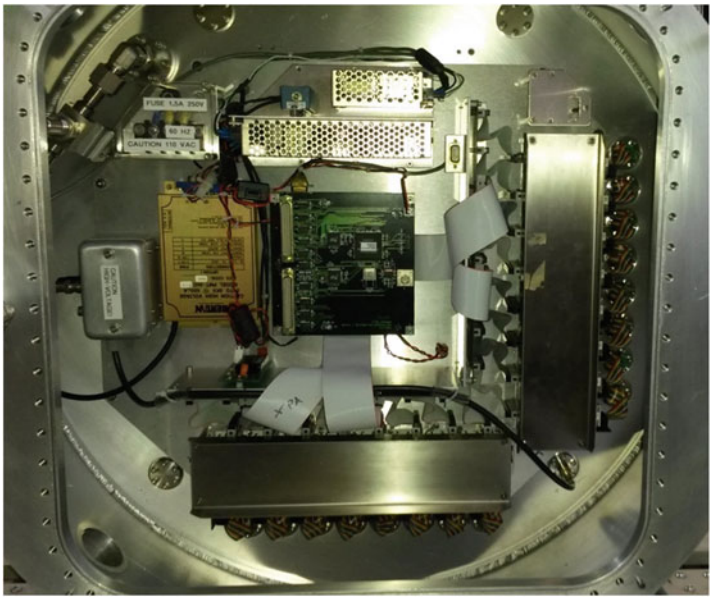

Fig. 3.57 Rear view of the ORDELA 2410N showing the electronics compartment. A cover plate can be installed if vacuum operation is desired

act as guard electrodes to maintain electric field uniformity near the edges. The cathode guard wires are connected to ground. The wires in the *y* cathode are 75 μm diameter stainless steel, oriented horizontally on a wire with a pitch of 0.313 cm.

The anode grid is located 0.5 cm behind the *y* cathode and is of identical construction. The wires in the anode grid are also oriented horizontally. The anode wires are bussed together to form a common electrode and held at positive high voltage (+3100 V) during operation.

The *x* cathode grid sits 0.5 cm behind the anode grid. The wires in this grid are oriented vertically, but otherwise its construction is identical to the *y* grid.

Each of the 256 cathode wires is connected to its own wide-bandwidth, low-noise, charge-sensitive preamplifier and discriminator. The 256 wires are combined into 16 groups of 16 (8 for *x* and 8 for *y*). These groups are shown in Fig. 3.57: the 16 groups of wires along the bottom feed into the horizontal preamplifier box, and the groups of wires along the right-side feed into the vertical preamplifier boxes.

3.7.3 Principle of Operation

The operating bias is determined by inspection of the counting curve, which is shown in Fig. 3.58. The counting curve is a measure of the detector count rate as a function of anode voltage. The operating bias occurs where the curve begins to level off (called the *knee* of the curve) because increasing bias further does not increase the count rate. For this detector, an operating bias of 3100 V was used.

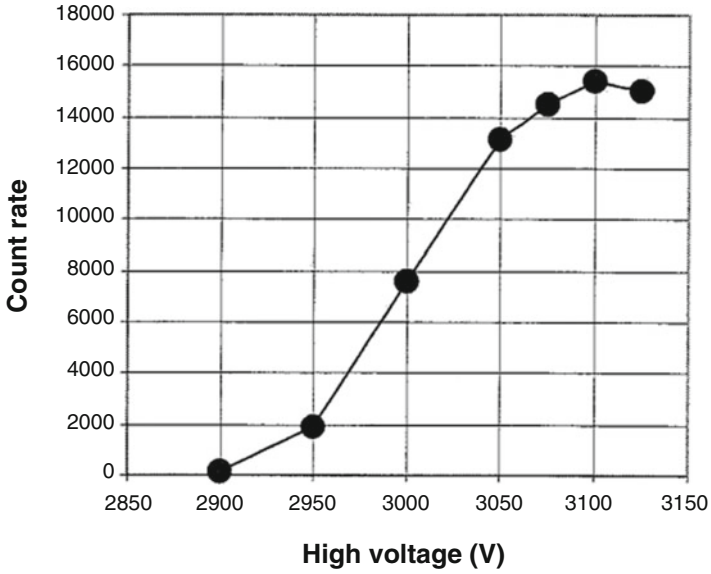

Fig. 3.58 Counting curve used to determine the operating voltage (3100 V) of the anode

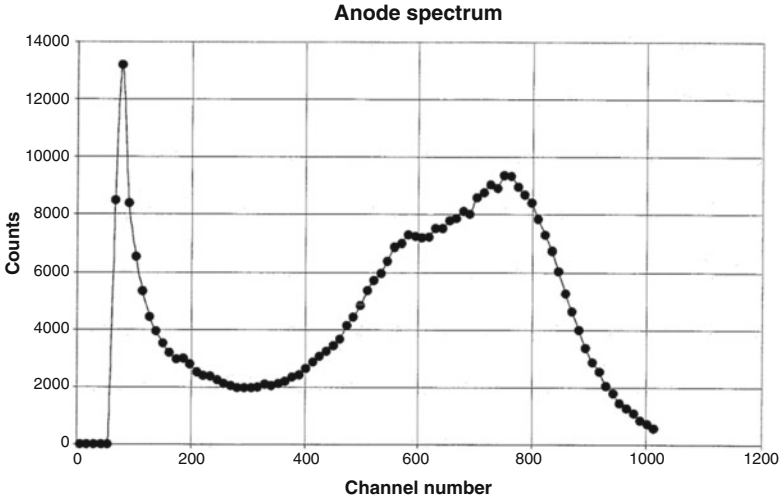

Fig. 3.59 Representative pulse amplitude spectrum illustrating the optimal choice for the discriminator setting to be around channel 300. This spectrum is for an anode voltage of 3075 V

An optimal setting for the discriminator was determined for each of the 256 cathode outputs. Figure 3.59 shows a typical pulse amplitude spectrum. The broad peak to the right (channels 400–1000) corresponds to detected neutron events, and the sharply rising peak to the left (below channel 200) results from lower amplitude events (typically electronic noise or gamma rays). The intervening valley represents the best discriminator setting, which rejects the unwanted low-amplitude events and retains events that result from neutron interactions in the detector.

The model 2410N position-sensitive proportional counter operates with a relatively low gas gain (~37) [26]. The ionization charge is estimated to be approximately 25,000 electron–ion pairs for the gas mix used, or approximately 4 fC per neutron. A gas gain of 37 produces an avalanche charge of approximately 150 fC on the anode grid, which induces current signals on the nearest *x* and *y* cathode wires as the ions drift from the anode toward the cathode wires. The combined proton–triton track length is approximately 0.66 cm (mostly resulting from the partial pressure of CF_4), which is about twice the anode and cathode wire pitch. Thus, up to three adjacent cathode wires can have an induced signal.

Position encoding consists of one preamplifier/discriminator per active wire, for independent amplification and discrimination of each of the 256 outputs (128 each for *x* and *y*). To avoid counting from multiple wires, each discriminator upon firing inhibits the triggering of its two adjacent neighbors, ensuring that only one discriminator from each cathode grid contributes to the position calculation. If two or more neutrons are detected simultaneously within a 100 ns time window, then they are flagged as pileup and rejected. All 256 cathode outputs are connected to an onboard processor for coincidence analysis. The neutron location is defined as the intersection of coincident events on the *x* and *y* cathode grids. Figure 3.60 shows an image of a 2D detector flood pattern under uniform illumination from a neutron source.

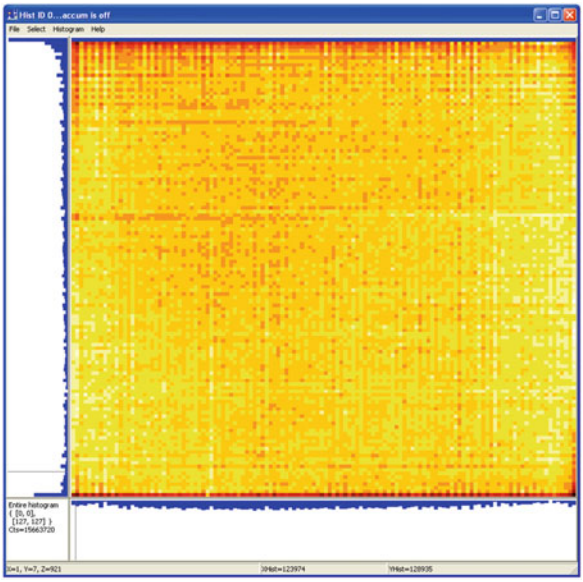

Fig. 3.60 2D detector flood pattern from the ORDELA 2410N detector. The horizontal and vertical integrated counts are shown along the bottom and the left edges

3.8 Beam Monitors

3.8.1 Introduction

Beam monitors are a critical component in neutron scattering experiments. They are used to characterize neutron beams, calibrate beamline equipment, and normalize data. For use in a neutron scattering environment, beam monitors are specifically designed neutron radiation detectors that monitor the neutron flux at various points along the beam path. They differ from typical neutron detectors in that their neutron detection efficiency is purposely low. Having a low enough collection efficiency so as to not distort too much of the neutron beam must be balanced with having a high enough count rate to obtain usable counting statistics.

Most of the neutron experiments at SNS and HFIR make use of cold and thermal neutrons, meaning that the neutrons are moderated or slowed to a range of approximately 0.12–12 meV (2.6–26.1 Å) for cold neutrons and 12–100 meV (0.9–2.6 Å) for thermal neutrons. Detectors and beam monitors designed for neutron scattering are built using isotopes that express a high probability that an incident neutron at these energies interacts to produce a measurable response. This reaction probability for a given isotope is called the *neutron cross section* and depends on the energy of the incident neutron. Table 3.4 lists the most-used isotopes for cold and thermal neutron detection and gives examples of typical detector topology in which they are used. The isotopes ^{3}He and ^{14}N are currently found in most beam monitors used at SNS and HFIR. In the following sections, beam monitor designs, theories of operation, acceptance criteria, and calibration techniques are examined.

Table 3.4 Commonly used isotopes for neutron detection

Isotope	Reaction	Q -value (MeV)	Neutron detection technology	Cross section at 1.8 Å (barns)
^{3}He	^{3}He + n → p (0.57 MeV) + ^{3}H (0.19 MeV)	0.764	Proportional gas counter Geiger–Muller tube	5330
^{14}N	^{14}N + n → p + ^{14}C	0.627	Low eff. proportional gas counter	1.91
^{10}B	^{10}B + n →		Gas electron multiplier Boron-lined ionization chamber	3840
	(6%) ^{7}Li (0.84 MeV) + ^{4}He (1.47 MeV)	2.792		
	(94%) ^{4}He + ^{7}Li + 0.48 MeV γ	2.310		
^{6}Li	^{6}Li + n → ^{4}He (2.05 MeV) + ^{3}H (2.73 MeV)	4.780	Scintillator detectors	940
^{235}U	^{235}U + n → fission fragments + n (5 MeV)	~200	Fission chambers	585

3.8.2 Neutron Beam Monitors

Neutron beam monitors are neutron detectors that are designed to have low absorption efficiencies to thermal and cold energy neutrons, permitting the maximum number of neutrons to reach the experiment sample and subsequent detector array. Beam monitors must also have a large dynamic range for thermal neutrons to provide sufficient counting statistics without saturation in high–neutron flux environments while also being able to discriminate neutron events from gamma ray and system noise in low-level background environments. Furthermore, beam monitors must have sufficient timing resolution to be used in TOF experiments, as well as a high level of radiation hardness, which is required for long-term operation in high-radiation environments. An ideal neutron beam monitor would allow for 100% transparency of the neutron beam, provide 2D position resolution to monitor the beam alignment, and be able to reproduce the complete incident beam energy profile to 100% accuracy independent of the impinging beam flux. However, this ideal monitor does not exist.

3.8.3 Beam Monitors Used in Neutron Science Experiments

Beam monitors perform instrument diagnostic checks, monitor neutron flux stability over an extended time period, normalize detector array data, correct chopper phasing, and calibrate other beamline equipment. At HFIR, monitors collect counting statistics to determine the number of neutrons that went into the sample and that scattered into the detector array. At SNS, the data collected from a beam monitor are

time stamped in reference to the accelerator pulses, and a TOF spectrum can be created for the intersecting neutron beam. This TOF spectrum can then be used to ensure that the instrument beam choppers are correctly phased to minimize the initial prompt pulse from the accelerator or to ensure that the chopped beam produces the correct energy band of neutrons required for a particular experiment. The beam monitor TOF spectrum can also be used to normalize the data collected by the main detector array because the beam presented to the instrument sample tends to have a variable distribution in the number of neutrons per energy bin. Additionally, the neutron flux and stability over time are vital for tracking overall facility health.

3.8.4 *Operation Physics of the Multiwire Proportional Chamber Beam Monitors*

The most widely used beam monitor type is based on an Multiwire Proportional Chamber (MWPC) design. This design includes a gas-filled proportional chamber that has multiple anode wires running through the active area. In the original design, each of these anode wires fed individual readout electronics to effectively create multiple radiation detectors within the same gas volume. To be used as a neutron flux beam monitor, these anode wires are connected to a common node to effectively create one continuous anode. The gas volume of the MWPC active area is filled with either ^{3}He or ^{14}N, depending on the intended efficiency range, as well as stopping and quenching gases. Stopping gases are added to limit the travel distance of the ionizing daughter particles created during a neutron absorption, thereby improving event localization. Quenching gases are polyatomic gas molecules, such as CF_4 or CO_2, that are added to absorb photons, which can be emitted during de-excitation of the energized molecules in the gas. If not captured, these photons can create their own avalanching effects and distort the data. Some gases, such as CF_4, have properties of stopping and quenching gases and can cover both necessities.

MWPC beam monitors work according to the following process. When a neutron is absorbed by the chosen isotope, the reaction creates ionizing daughter particles, as described in Table 3.4. These particles travel in opposite directions away from the interaction site. Electron–ion pairs are created by these daughter particles as they drift through the surrounding gas atoms and create ionization trails. The average number of primary electron–ion pairs created depends upon the type of fill gas in the MWPC. With the fill gas composition known, the total number of primary electron–ion pairs can be approximated using Eq. (3.110) and Table 3.5:

$$n_0 = \frac{\Delta E}{w_{\mathrm{i}}} \tag{3.110}$$

where ΔE represents the charged particle energy loss, and w_{i} is the average energy needed to create a pair dependent upon the used gas [27].

Table 3.5 Commonly used detector fill gases with calculated maximum number of electron–ion pairs created by a neutron absorption

Fill gas	w_i (eV)	n_0 for ^{3}He (all 764 keV are lost)	n_0 for ^{14}N (all 627 keV are lost)
H_2	37	20,649	16,946
He	41	18,634	15,293
N_2	35	21,829	17,914
O_2	31	24,645	20,226
Ne	36	21,222	17,417
Ar	26	29,385	24,115
CO_2	33	23,152	19,000
CH_4	28	27,286	22,393
CF_4	54	14,148	11,611
Xe	22	34,727	28,500

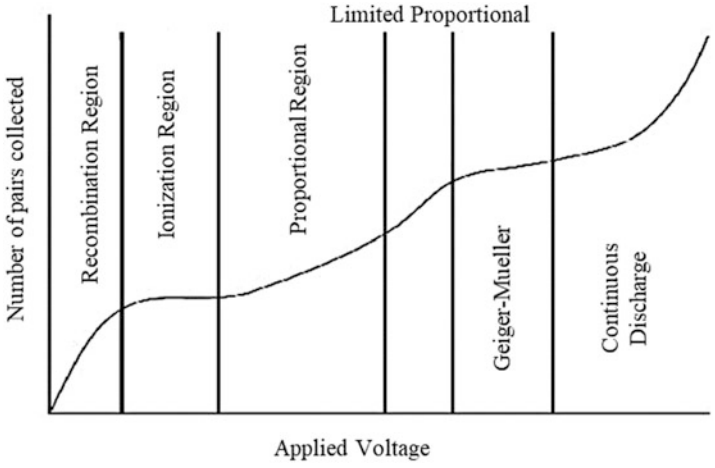

Fig. 3.61 Ionizing radiation detector operation range. Applied bias voltage depicts the number of electron–ion pairs collected [28]

The anode bias voltage is set such that the monitor operates in the proportional region, as described in Fig. 3.61. Within this operation region, the freed electrons begin to quickly drift toward the positively charged anode wire, and the positive ions drift toward the cathode walls. While the freed electrons drift in a small field, no additional charge is generated, corresponding to Fig. 3.65a. Unlike many other MWPC-type detectors, beam monitors often have a small number of anode wires at spacings that are large compared with the distance between the chamber walls. This design prohibits the monitor from forming a constant field drift region away from the anode wires. Instead, the potential distribution takes on the more complicated form shown in Fig. 3.62, which was obtained from a solution to the

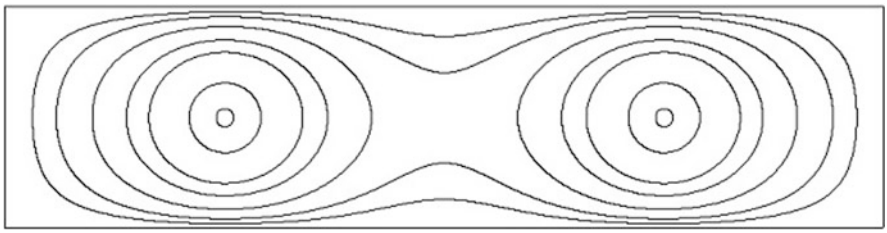

Fig. 3.62 Equipotential lines surrounding biased anode wires in a cross section of a typical beam monitor geometry. An active area 125 mm high by 500 mm wide is depicted with two anode wires centered vertically and 125 mm from the walls horizontally. The equipotential contours are for 10, 20, 40, 70, 100, and 200 V, assuming a 700 V bias

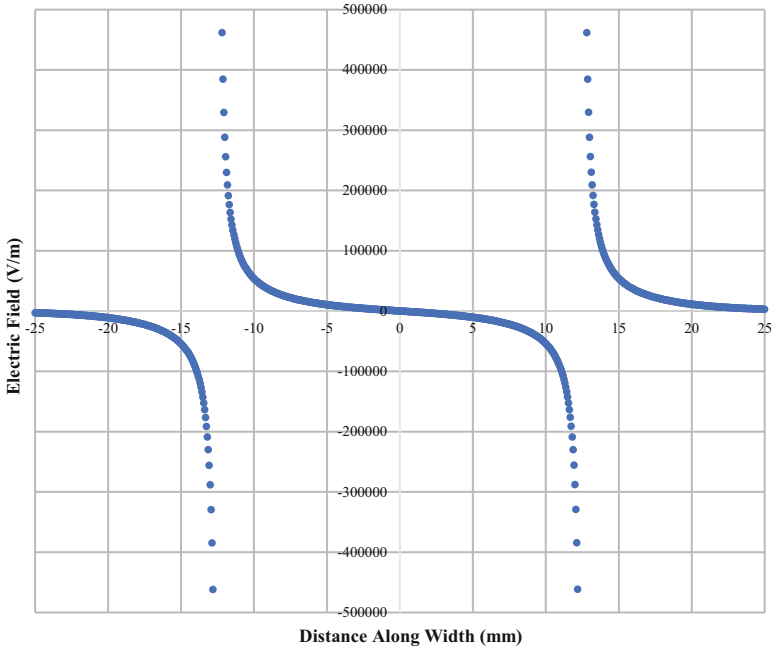

Fig. 3.63 Electric field along a line parallel to the long direction of the monitor shown in Fig. 3.62, passing through the anode wires. The horizontal field component is shown with positive values for the direction, which would drive a positive charge toward higher distance values

electrostatic boundary value problem. Figure 3.63 shows the electric field along an axis intersecting the anode wires from this solution. The high-field regions near the wires can be seen, but they are superimposed on a background field. The charged anode wires induce image charges on the chamber walls. The background field is generated mainly by these image charges, with a small additional contribution from the other anode wire.

As the electrons move closer to the anode wire, they enter the strong electric field surrounding the wire. Within this electric field, the freed electrons accumulate enough kinetic energy to produce secondary electron–ion pairs, as shown in Fig. 3.65b. This effect continues as the secondary electrons drift through the electric field and create tertiary (and more) electron–ion pairs, as shown in Figs. 3.65b and 3.66c, leading to a signal-multiplication effect called the *Townsend avalanche*. Equation (3.111), the Townsend avalanche equation, details the number of electrons created (dn) per path (ds), where α is the first Townsend coefficient of the gas. This coefficient depends on the electric field strength at a particular radial distance r from the center of the anode wire, as detailed in Fig. 3.64. Below the threshold for gas multiplication, the Townsend coefficient is zero, and it increases quickly above the threshold for gas multiplication [27].

$$dn = n\alpha ds \tag{3.111}$$

If n_0 electrons enter the avalanche region, then they will increase to n_f electrons passing through it, where Eq. (3.112) defines n_f as the following:

$$n_f = n_0 \exp\left\{\int \alpha ds\right\} \tag{3.112}$$

As described in Eq. (3.113), the total charge (Q_T) generated by the absorption of a neutron is dictated by the number of primary electron–ion pairs produced and the gas gain (M) of the monitor [9]. Gas gain is the average multiplication factor applied to the initial number of electron–ion pairs. Equation (3.114) shows that, in general, gas gain is dependent on the anode bias voltage and subsequent electric field, the first Townsend coefficient for the given electric field strength, the radius of the anode wire (a), the radial distance moving away from the center of the anode wire (r), and the critical radial distance (r_c) away from the anode wire beyond which there is not enough field strength to inhibit electron multiplication [9]. This Townsend avalanche effect eventually creates clouds of electrons and positive ions that surround the anode wire, as shown in Fig. 3.65d.

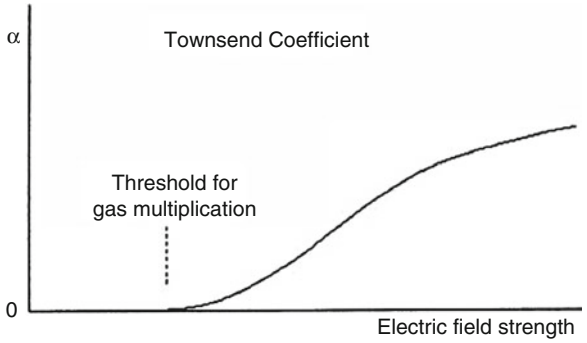

Fig. 3.64 Plot of the first Townsend coefficient vs. applied electric field strength [9]

$$Q_T = n_0 eM = en_f = en_0 \exp\left\{\int_a^{r_c} \alpha dr\right\} = en_0 \exp\left\{\int_{E(a)}^{E(r_c)} \alpha(E) \frac{\partial r}{\partial E} dE\right\} \quad (3.113)$$

$$\ln M = \int_{E(a)}^{E(r_c)} w(E) \frac{\partial r}{\partial E} dE \quad (3.114)$$

If only elastic collisions occur, then the electrons and ions drift through the gas at a rate proportional to the electric field (E) and the mean free path between collisions. This mean free path is inversely proportional to the gas pressure (p), so the drift velocity is proportional to E/p. If the charged particle accumulates enough energy from the electric field between collisions, then it can have an inelastic interaction with the atom or molecule that is struck, decreasing its velocity. The accumulated energy is proportional to the electric field multiplied by the mean free path between collisions and is thus proportional to E/p. The drift velocity remains a function of E/p, but the function is not linear. The ionization events within the Townsend avalanche region are examples of these inelastic collisions. Because the ions are several thousand times heavier than the electrons, they accelerate more slowly in the electric field, causing them to have much lower drift velocities.

The electrons released in the Townsend avalanche region are in a high–electric field region, have high mobility, and are near the anode wire. Therefore, they reach the anode wire and are absorbed by it within a few nanoseconds, as shown in Fig. 3.65e. The released ions do not move very far during this time. They are left behind to create a region with a positive space charge, which capacitively attracts electrons in the anode wire and in the beam monitor wall. Initially, this attraction keeps most of the electrons that were deposited on the wire confined to a region near where they were absorbed. At the wall, the attraction of electrons by the space charge is mostly canceled out by the repulsion from the extra electrons on the anode wire. As time passes, the ions drift away from the anode wire. The ions become less effective at confining the electrons that were deposited on the wire, allowing those electrons to disperse and create a current of electrons that are conducted through the anode wire and transfer into the external readout electronics. At the beam monitor

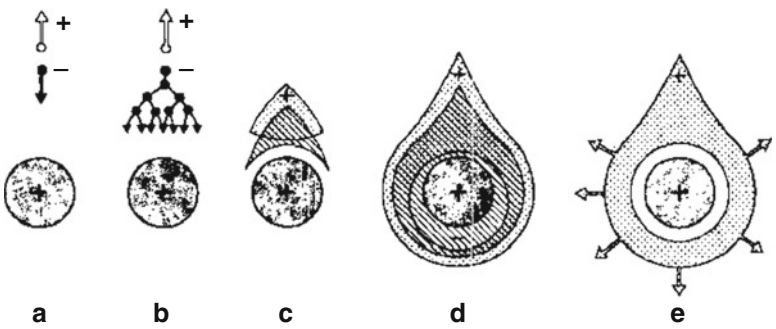

Fig. 3.65 Step-by-step development of charge clouds in general proportional counter [29]

wall, the attraction of electrons by the space charge is no longer fully canceled out by the repulsion from the extra electrons on the anode wire, allowing electrons to be pulled into the wall through an external connection. Eventually, over several microseconds, some of the ions drift all the way to the beam monitor wall. They pick up an electron from the wall and become neutral. This ion consumes one of the electrons that was attracted to the wall. However, it does not alter the electric field distribution within the beam monitor, and it does not cause more electrons to enter the wall from an external connection.

At the end of this process, all the charge that was deposited on the anode will have traveled through an external connection to the beam monitor wall. The motions of the positive ions influence the rate at which this external transfer occurs, but the bulk of the charge transfer may occur during a shorter time than it takes for the ions to reach the wall. The charge directly released by a neutron reaction is small compared with the charge generated near the anode wire by the Townsend avalanche. Each electron from the directly released charge that reaches the Townsend avalanche region near the anode wire creates a current pulse whose time evolution is set by the geometry of the wire relative to the beam monitor wall, not by the location of the initial release. This process occurs over a characteristic time (T_A), which could be defined as the FWHM. The arrival rate of electrons from the directly released charge to the anode wire also disperses by some characteristic time T_I. The position where the neutron absorption occurs should only influence the output pulse shape if T_I is a substantial fraction of T_A.

3.8.5 Beam Monitor Performance Characteristics

3.8.5.1 Count Rate Limitations

For a given neutron event, the resulting charge pulse has a current exceeding the discriminator setting for some time T. The value of T varies from pulse to pulse, but it has some average value T_d, which is often in the 1–2 μs range for the MWPC beam monitors. If a second event occurs in the same vicinity before a previous charge event has dissipated, then the second charge pulse will ride on top of the previous pulse, resulting in pulse pileup. If neutrons react within the beam monitor at a low rate (R_n), then some fraction of events (RT_d) is missed owing to the pulse pileup, resulting in a measured count rate (R_m) described by Eq. (3.115). Pulse pileup can cause the readout electronics to incorrectly measure the magnitude of both pulses, resulting in incorrect counting statistics. Figure 3.66 shows a graphic representation of the pulse pileup effect. At high rates, the chances of multiple pulse pileups within the time T_d becomes appreciable, and results in Eq. (3.115) taking on an exponential form, detailed in Eq. (3.116).

$$R_m = R(1 - RT_d) \tag{3.115}$$

$$R_m = R\exp\{-RT_d\} \tag{3.116}$$

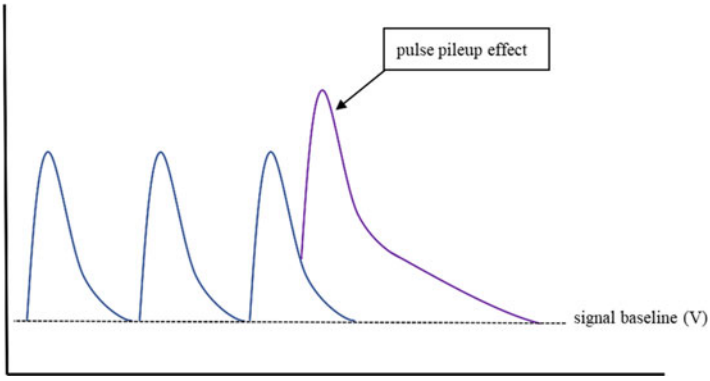

Fig. 3.66 Pulse pileup effect on pulse height measurement

As the impinging rate increases, the measured count rate first increases linearly until a maximum is reached at $R_m = 1/T_d$, then it decreases to zero. The rate at which an MWPC detector begins to experience degradation in counting linearity has been experimentally determined to be between 10,000 and 15,000 counts per second. At very high-count rates, the charge clouds that surround the anode wire begin to accumulate for a prolonged period without being able to fully dissipate. The charge clouds effectively saturate the anode and change the pulse shape from an event. The saturation is a more complex effect that is not easily modeled by a simple equation. In practice, it would be difficult to drive an MWPC beam monitor hard enough to progress beyond the reduced-linearity region. Figure 3.67 predicts the count rate linearity vs. impinging neutron flux based on the regimes governed by Eqs. (3.115) and (3.116).

3.8.5.2 Beam Monitor Neutron Absorption Probability

Two main probability factors determine the MWPC beam monitor neutron detection efficiency. The first factor is the probability (P_{eff}) that a neutron will be absorbed by a ^{3}He or ^{14}N nucleus and result in the emission of an energized charged particle. As shown in Eq. (3.117), this probability is influenced by the absorption cross section (σ), the number density of the nuclei (N), and the distance (D) that the neutron can travel through the gas medium. Many materials used for neutron absorption, including ^{3}He and ^{14}N, have an absorption cross section that is proportional to the incident neutron wavelength; therefore, the reaction probability is also proportional to the neutron wavelength. MWPC beam monitors are designed such that $\sigma ND \ll 1$, so $P_{eff} \approx \sigma ND$. For higher efficiencies, generally between 10^{-3} and 10^{-4}, ^{3}He is the preferred isotope, and for lower efficiencies, generally between 10^{-4} to 10^{-6}, ^{14}N is used.

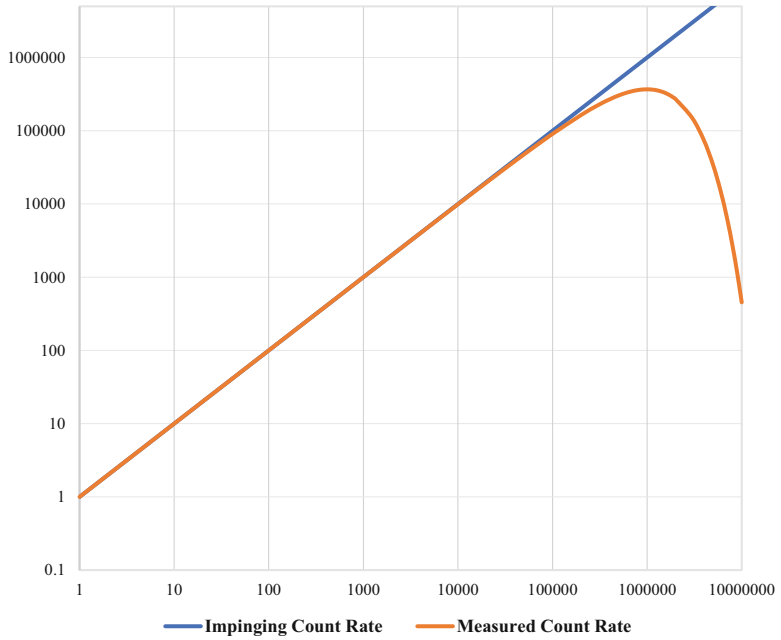

Fig. 3.67 Theorized flux rate vs. measured rate for an MWPC beam monitor

$$P_{\text{eff}} = 1 - \exp\{-\sigma ND\} \tag{3.117}$$

The cross sections of neutron absorbers are often quoted as their value σ_T for neutrons thermalized to 300 K, where they have an average wavelength $\lambda_T = 1.8$ Å. For wavelength λ, $P_{\text{eff}} = [(\sigma_T\lambda)/\lambda_T]ND$. A beam monitor's absorption probability is often quoted as $P_{\text{Thermal}} = \lambda_T ND$. This equation can be converted to $P_{\text{eff}} = P_{\text{Thermal}}(\lambda/\lambda_T)$ for other wavelengths.

For gaseous absorbers, the ideal gas law, $p = N_M k_B T$, can be used to calculate the desired partial pressure of the absorber. Here, N_M is the number density of molecules, k_B is the Boltzmann constant ($k_B = 1.38 \times 10^{-23}$ J/K), T is the temperature, and p is the gas pressure. If r_m is defined as the number of absorber atoms per molecule N/N_M, then $N_M = N/r_m = P_{\text{eff}}/(\sigma D r_m)$, and $p = (P_{\text{eff}} k_B T)/(\sigma D r_m)$. If a monitor operates at 300 K with $D = 1.2$ cm, and the desired efficiency using ^{3}He is 1×10^{-3} at $\lambda = 1.8$ Å, then $r_m = 1$, and $\sigma = 5330$ barn. These parameters yield a gas pressure of 647 Pa. This pressure is low enough that some carrier gas, such as argon, should be added when filling the monitor. If a 1×10^{-5}efficiency is desired using $^{14}N_2$ as the absorber, then $r_m = 2$, and $\sigma = 1.91$ barn. These parameters yield a gas pressure of 9031 Pa, which is still low enough that a carrier gas should be added. For a 1×10^{-4}efficiency monitor using $^{14}N_2$, the gas pressure is 90,310 Pa, which is nearly atmospheric pressure. In this case, the nitrogen might be the dominant component of the gas mixture.

3.8.5.3 Beam Monitor Neutron Event Detection Probability

The second factor is the probability that the current pulse created by a neutron absorption is large enough to activate the discriminator and generate an output pulse from the beam monitor system. Knowledge of the pulse-height spectrum is required to predict the influence of the discriminator setting on the fraction of neutron reactions that get discriminated. The pulse-height spectrum can be represented as a function (S) of the collected charge (Q) from a current pulse corresponding to a neutron reaction, where S is defined such that the probability that the collected charge from a current pulse is between Q, and $Q + \Delta Q$ is proportional to $S(Q)\Delta Q$. If a discrimination between accepted and rejected pulses could be based on some charge threshold Q_m, then Eq. (3.118) determines the probability that a neutron reaction passes the discriminator setting and triggers the output electronics (P_{Dis}). Here, Q_m represents the entire range of charge for which the function S has an appreciable value. Figure 3.68 shows an idealized depiction of a pulse-height spectrum from a neutron detector used to show appropriate choices for Q_{D} and Q_m, as used in Eq. (3.118). The discriminator level, Q_{D}, is carefully selected to just above the level of gamma ray detections and electronic noise to eliminate false counts in the system; both such events are shown on the far left of Fig. 3.68.

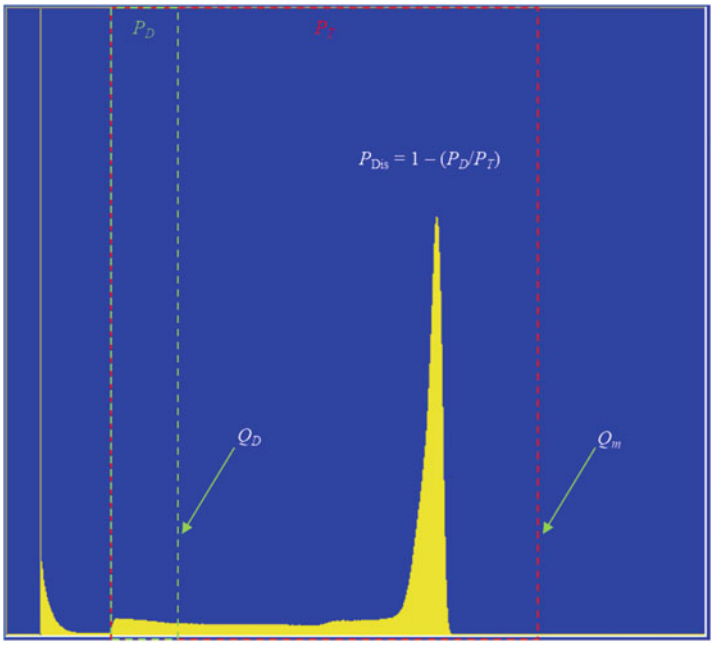

Fig. 3.68 The probability that an event triggers discriminator electronics [30]

$$P_T = \int_0^{Q_m} SdQ$$

$$P_D = \int_0^{Q_D} SdQ$$

$$P_{\text{Dis}} = 1 - \frac{P_D}{P_T} \tag{3.118}$$

Figure 3.69 shows a measured pulse-height spectrum from a 1×10^{-3}efficiency ^{3}He beam monitor operating at 580 V bias. The charge was determined by integrating the current from a pulse generated by a neutron event during a 3 μs period. The cutoff of the spectrum for charges less than 0.05 pC is an artifact of the measurement apparatus, which required a discriminator level to be set to trigger the integrations. The true spectrum would have some amplitude in this region. This spectrum's shape differs significantly from the idealized depiction shown in Fig. 3.68. The peak count rate corresponds to a charge that is approximately one-third of the maximum charge.

Figure 3.70 illustrates the dependence of the charge range of the pulse-height spectrum on the bias voltage. The data was collected using the same beam monitor and measurement apparatus as that for Fig. 3.69. The maximum charge is defined as

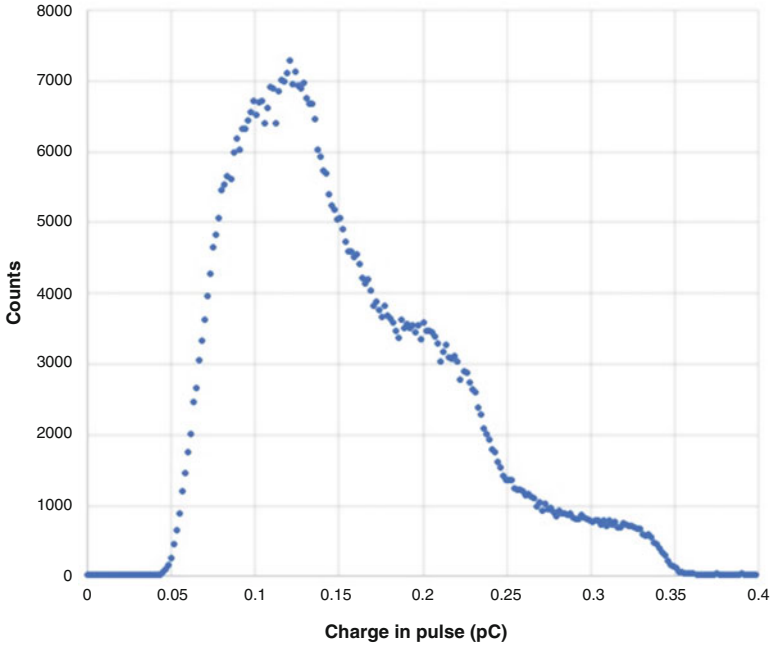

Fig. 3.69 Pulse-height histogram for a 1×10^{-3}efficiency beam monitor using ^{3}He as an absorber. A 580 V bias was used. The charge is measured by integrating the current from a pulse over a 3 μs period

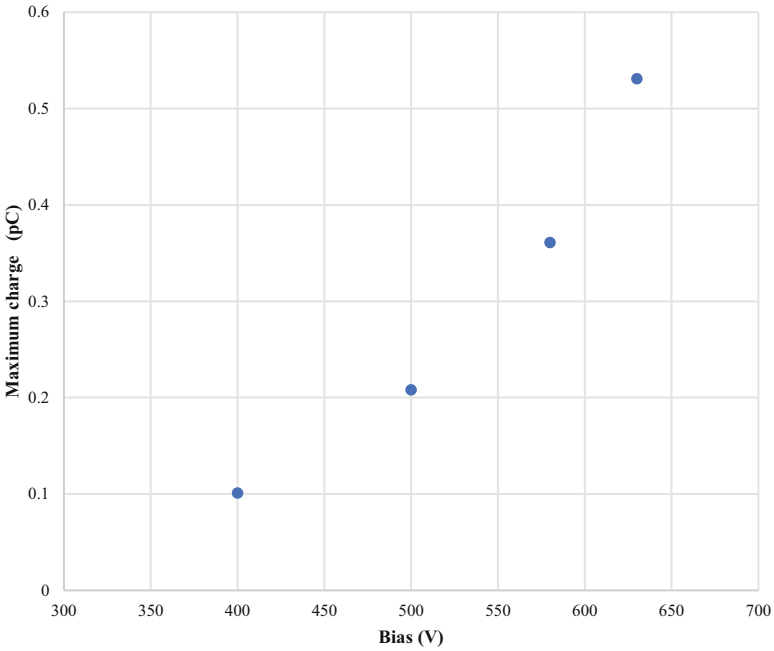

Fig. 3.70 Dependence of pulse-height spectrum range on the bias voltage. This used the same 1×10^{-3}efficiency^{3}He beam monitor and measurement setup that obtained the pulse height spectrum of Fig. 3.69. Maximum charge refers to the highest charge for which the pulse-height spectrum is observed to rise above the background level

the highest charge for which the pulse-height spectrum is observed to rise above the background level. The maximum charge depends strongly on the bias. The overall shape of the spectrum does not vary much as the bias changes. Higher bias voltages are more likely to trigger the discriminator, but they can also cause preamplifier saturation, raise the required discriminator level needed to reject gamma ray detections and noise, and reduce the recovery time between neutron events.

Figure 3.71 gives an example of a neutron pulse triggering the discriminator circuitry. This pulse reaches its maximum amplitude within 1 μs and maintains an appreciable amplitude over a time interval of approximately 3 μs. Significant variations in shape exist among the pulses. These variations include the time it takes for a pulse to reach maximum amplitude and the width of the of the pulse. Figure 3.72 shows an example of a gamma ray pulse from a ^{60}Co source that does not have the pulse height required to trigger the discriminator.

The decision to measure a detector pulse cannot initially be based on its charge because the charge is not known until after the pulse current has been integrated. Instead, most practical discrimination circuits rely on the pulse's peak amplitude to trigger the discrimination. If the pulse shape does not remain constant, then the ratio of the peak amplitude to the charge will not be constant. An amplitude-based

Fig. 3.71 Oscilloscope measurement of (*yellow trace*) neutron event triggering (*green trace*) discriminator circuitry. Discriminator level set to approximately 100 mV above baseline in this example

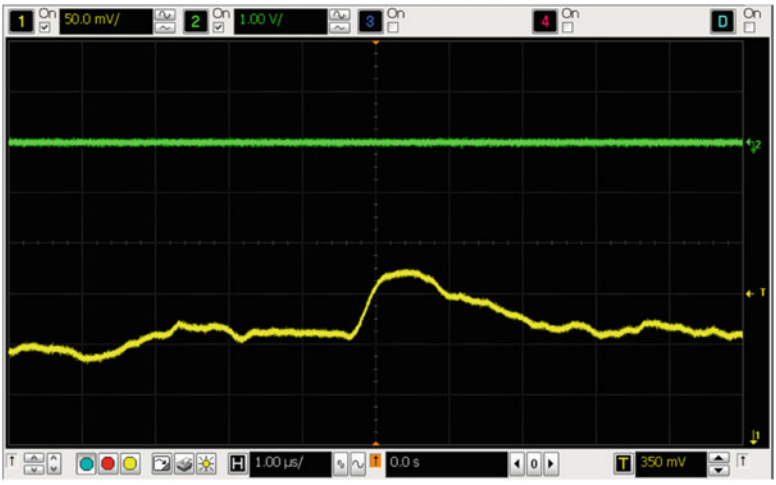

Fig. 3.72 Oscilloscope measurement of (*yellow trace*) gamma event using a ^{60}Co source that is too low in amplitude to trigger (*green trace*) discriminator circuitry. Discriminator level set to approximately 100 mV above baseline in this example

discrimination will cause some pulse-to-pulse variation in the charge Q_D from a pulse whose peak amplitude is just large enough to trigger the discriminator. Despite this variation, a peak amplitude-to-charge ratio for a typical pulse shape can be used to estimate the value of Q_D, which corresponds to a peak amplitude discriminator

voltage V_D. Dividing the total area under a time plot of a pulse by the peak amplitude of the pulse yields a time t_p. Multiplying the peak current I_p of the pulse by t_p gives the charge of the pulse. Between the beam monitor output and the discriminator is a preamplifier with some current-to-voltage gain R_A. For a pulse whose amplitude is just large enough to trigger the discriminator, $V_D = R_A I_p = R_A(Q_D/t_p)$, which means $Q_D = (t_p/R_A)V_D$. For the pulse in Fig. 3.71, t_p is approximately 2 μs. The preamplifier used at SNS has R_D = 5,600,000 V/A, giving $t_p/R_A = 3.57 \times 10^{-13}$ C/V.

The pulse-height spectrum is also influenced by the fill gas composition and pressure. Because the mean free path is reduced, increasing the pressure increases the bias voltage required to achieve a desired gas gain. The gas composition affects the energy required to form electron–ion pairs, influencing the number of such pairs produced by the detection event and the amount of charge multiplication. Therefore, a dependence exists between the fill gas composition and pressure and the required beam monitor bias voltage to obtain an adequate charge range in the pulse-height spectrum. This charge range is needed to keep discriminator cutoff of low-amplitude pulses from causing an unacceptably high loss of beam monitor efficiency. To obtain similar performance to a 1×10^{-3}efficiency ^{3}He monitor with 600 V bias, a 1×10^{-4}efficiency $^{14}N_2$ monitor needs 1250 V, and a 1×10^{-5}efficiency $^{14}N_2$ monitor needs 750 V.

As shown in Fig. 3.83, which appears later in Sect. 3.8.8, experiments have revealed that the detection efficiency of a beam monitor can be lower for neutrons arriving far from an anode wire than that of neutrons arriving near the wire. This effect is most pronounced when the monitor is operated at low bias voltages, possibly because the spread in arrival times for the electrons generated by a neutron detection far from the anode is larger than that for electrons from a neutron detection near the anode. This arrival time spread corresponds to the value T_I in the Townsend avalanche discussion. If the arrival time spread is large enough, then the pulse width increases, lowering the peak amplitude-to-charge ratio. This lower ratio increases the discriminated charge cutoff Q_D, causing a greater fraction of events to be rejected. The fraction of rejected events must be high for this effect to produce any significant distortion in the monitored count rate.

If the bias voltage is varied without making compensating changes to the discriminator setting, then the fraction of rejected events is highest at low bias voltages. This high fraction of rejected events may explain the bias dependence of the efficiency variations. Determining how much time the electrons need on average to drift to the anode helps to evaluate the importance of this effect. The drift velocity (v) depends on the electric field, the gas pressure, and the gas composition. Owing to the availability of published data on drift velocities [31], this velocity is calculated for nitrogen at a pressure of 1 atm and a temperature of 293 K. The calculated velocity is a reasonable approximation to conditions in a 1×10^{-4}efficiency monitor.

Figure 3.73 shows a log plot created using published data [31] for the dependence of drift velocity on E/p for nitrogen at a temperature of 293 K, where v is in units of centimeters per second, and E/p is in units of volts per torr-centimeters. The dependence seems nonlinear. A line of slope equal to one-half is also plotted on

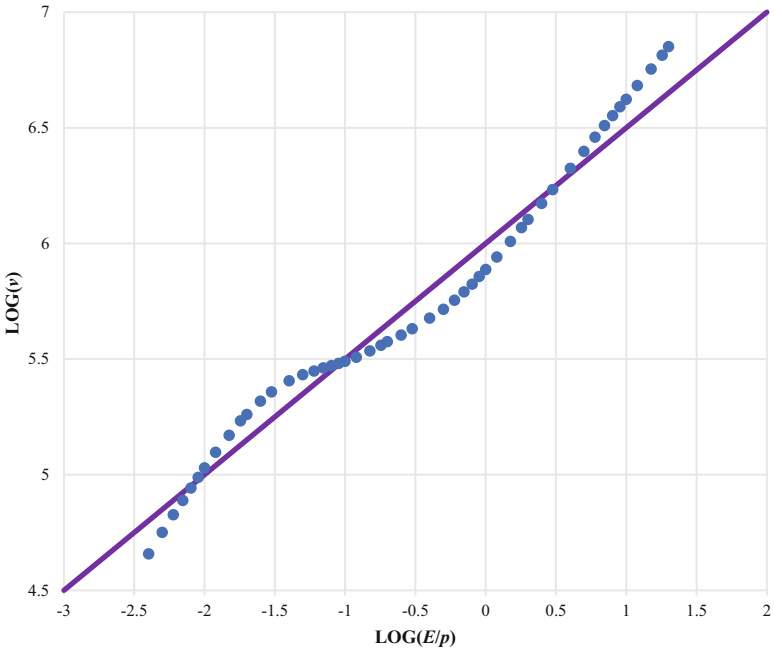

Fig. 3.73 Log plot to show dependence of v on E/p for nitrogen at 293 K

Fig. 3.73, corresponding to Eq. (3.119). Although the linear slope is not a perfect representation of the plotted data, it does remain within a factor of 2 of the plotted data's slope.

$$v = k\sqrt{\frac{E}{p}} \quad \text{where } k = 10^6 \left(\frac{\text{Torr} \cdot \text{cm}^3}{\text{s}^2\text{V}}\right)^{\frac{1}{2}} \tag{3.119}$$

Equation 3.120 calculates the time (t) that an electron released by an event that occurs at a distance (D) from the wire will take to drift to the anode wire. Equation 3.121 gives the formula for estimating the electric field that is present at a distance (r) from the wire, where V_{Bias} is the anode bias voltage, a is the radius of the anode wire, and r_{wall} is the distance from the anode wire to the beam monitor wall. Equation 3.121 should be accurate for distances that are short compared with r_{wall}. As shown in Fig. 3.63, Eq. (3.121) becomes more approximate at larger distances because of the noncylindrical wall and overlapping fields from other anode wires.

$$t = \int_0^D \frac{dr}{v} = \frac{\sqrt{p}}{k} \int_0^D \frac{dr}{\sqrt{E}} \tag{3.120}$$

$$E = \frac{V_{\text{Bias}}}{k_1 r} \quad \text{where } k_1 \approx \ln\left(\frac{r_{\text{wall}}}{a}\right) \tag{3.121}$$

Combining these equations leads to the estimate of the electron drift time in Eq. (3.122).

$$t = \frac{1}{k}\sqrt{\frac{pk_1}{V_{\text{Bias}}}}\int_0^D \sqrt{r}dr = \frac{2}{3k}\sqrt{\frac{pk_1 D^3}{V_{\text{Bias}}}} \tag{3.122}$$

For a beam monitor filled with nitrogen at 1 atm ($p = 760$ Torr) with a 25 μm anode wire radius and a 5 mm distance to the monitor wall operating at 700 V anode bias, Eq. (3.122) calculates that the electrons created from an event 2 cm from the wire will take approximately 4.5 μs to reach the wire. This time is a little longer than the duration of a typical output pulse from the beam monitor.

If all the electrons from the event were drifting at the same velocity, they would reach the anode with no spread in their arrival times, creating an output pulse that is delayed but whose width is not altered. The drift velocity refers to an average rate of travel, and the paths that the individual electrons take include some randomness. This randomness creates a spread in the electron arrival times, which might be a substantial fraction of the total drift time, in which case the spread widens the beam monitor output pulse, decreasing its peak amplitude-to-charge ratio. This ratio decrease increases the likelihood that the peak amplitude is below the discriminator threshold, causing the pulse to be rejected. Arrival time spreads of approximately a microsecond—one-fourth of the estimated drift time—are needed for this effect to become significant. Beam monitor output pulses have significant variations in duration, suggesting that significant variations in charge arrival times are occurring.

Charge recombination is another possible mechanism for position-dependent efficiency variations. The conjecture is that the low drift velocities and long travel times for charges generated far from the anode increase the fraction of the charges that recombine. This increase in charge recombination decreases the amount of charge reaching the anode, decreasing the amplitude of the output pulse. This pulse is more likely to be rejected by the discriminator. One possibility is that the charges recombine very soon after they form, before they have time to move apart. This fast recombination can be important in solids and liquids. The lower density of gases causes the generated charges to be more widely dispersed, which makes this form of recombination much less likely.

A second possibility is that the electrons are captured while they are on their way to the anode. The likelihood of this possibility depends on the presence of electronegative gases. An *electronegative material* is a substance whose atoms or molecules can form negatively charged ions. A free electron encountering such a material can be absorbed by it, creating a slowly drifting ion that does not contribute to the output pulse. The gases chosen to fill beam monitors are not electronegative, but the presence of an electronegative material as an impurity cannot be ruled out.

Although neither of the recombination mechanisms seems likely to account for substantial levels of charge recombination, the measured shape of the pulse-height spectrum must be considered. If all the charge from every event makes it to the anode, then a pulse-height spectrum that is strongly peaked near the maximum

charge cutoff is expected. However, this strong peak is not observed in the pulse-height spectrum.

3.8.6 *Mechanical Design of MWPC Beam Monitors*

Most of the beam monitors employed at SNS and HFIR are based on MWPC technology. As shown in Fig. 3.74, these monitors are made using a vacuum-sealed aluminum enclosure that presents a 1 mm thick window on either side of the active area. This active area (and, thus, the overall monitor size) is customizable depending on application requirements. The preamplifier enclosure is attached directly to the active area of the monitor and contains two feedthroughs, which access the monitor's active area, as shown in Fig. 3.75. One of the feedthroughs fills the enclosure with a volume of gas composed of a mixture of selected fill gas to ensure proportional mode operation, along with a finely controlled amount of either ^{3}He or ^{14}N as the neutron absorber. Depending on the length and width of the monitor's active area, two or four anode wires–on the order of 0.0005 in. in diameter (1.27 μm)–are routed through the active area. These wires are all connected at a central node to effectively make one continuous anode. The anode is positively biased by an external source using the second feedthrough. MWPC monitors are biased such that the monitor operates in the proportional mode to enable pulse height discrimination. Figure 3.76 shows the internal design of the active area for this type of monitor.

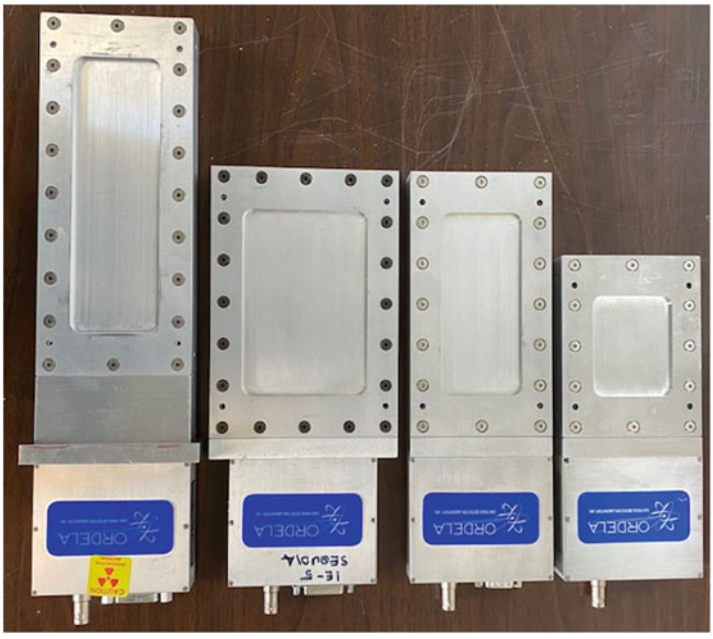

Fig. 3.74 MWPC beam monitors

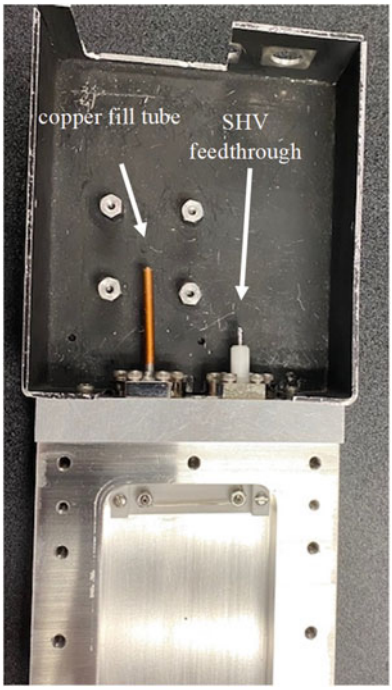

Fig. 3.75 MWPC active area feedthroughs

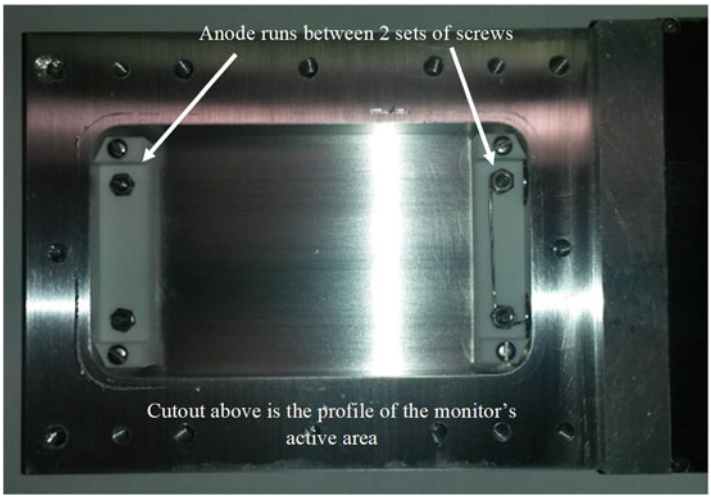

Fig. 3.76 Mechanical design of the MWPC beam monitor

3.8.7 Beam Monitor Readout Electronics Overview

3.8.7.1 Preamplifier

This section details the readout electronics of the SNS-style beam monitor system. The beam monitors used at HFIR employ an Ordela manufactured readout system, which will not be discussed here. The SNS beam monitor preamplifier housing, shown in Fig. 3.77, is attached directly to the beam monitor enclosure to limit potential noise pickup and signal attenuation of the charge pulse. Inside the housing sits the Beam Monitor Preamplifier Board; Fig. 3.78 shows an electrical schematic for the SNS-style beam monitor preamplifier. The preamplifier board consists of a low-pass filter and DC (direct current) blocking circuit, followed by four distinct stages of pulse shaping and amplification before a comparator circuit and single-ended to differential converter circuit. First, a low-pass filter consisting of a resistor and capacitor is connected in series with a 1 MΩ resistor to filter the anode bias

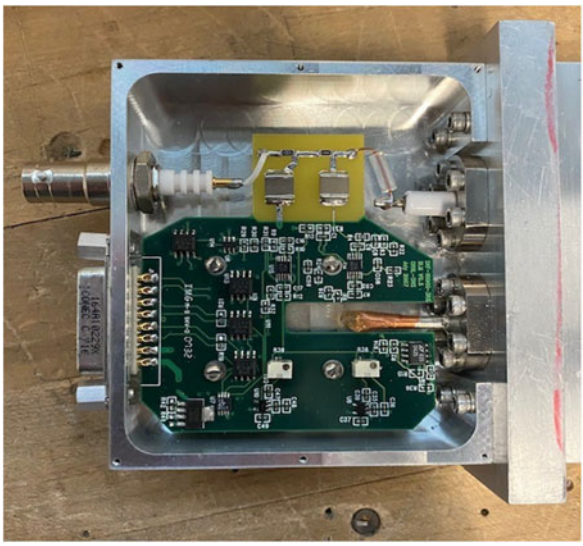

Fig. 3.77 Beam monitor preamplifier housing

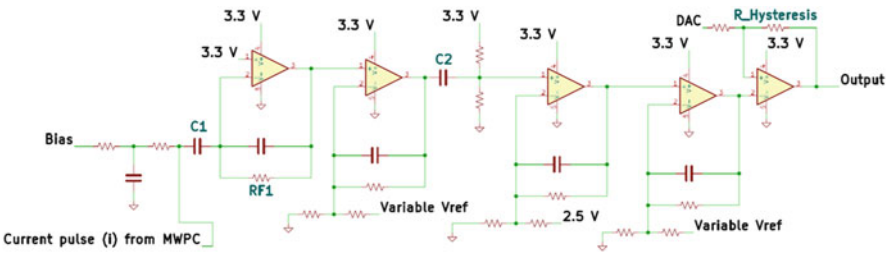

Fig. 3.78 MWPC SNS-style preamplifier schematic

voltage that is supplied from an external source through the safe high voltage bulkhead. A 15 nF capacitor, labeled C1 in Fig. 3.78, then blocks the DC bias voltage while allowing the detection current pulse to reach the subsequent amplification stages. The first amplification stage is a transimpedance amplifier, which transforms the current pulse (I) from the monitor to a voltage output through resistor *RF1* in Fig. 3.78, as detailed in Eq. (3.123).

$$V = I \times RF1 \tag{3.123}$$

Next, the voltage output of the first stage is shaped and amplified by three voltage amplification circuits. Stages one and three each have a potentiometer to manually adjust their respective voltage references, and the voltage reference used in stage two is set via a resistive voltage divider circuit. A series capacitor (C2) is used between the second and third stages of amplification to improve the preamplifier's thermal stability. Without this series capacitor, thermal drift in the voltage offset from the first stage would be amplified by the full gain of the remaining stages.

Finally, the last stage of the preamplifier board consists of an operational-amplifier comparator circuit, which acts as a discriminator for the amplified signal. An onboard DAC is used to set the discriminator threshold remotely. Another resistor (R_Hysteresis) is added between the DAC output and the positive input of the comparator. This resistor is part of a hysteresis circuit that prevents more than one triggered pulse per neutron event. The comparator output is then converted to a differential pair and sent to a beam monitor control box via a 15-pin data bus connector.

3.8.7.2 Control Box

The beam monitor data acquisition system consists of a beam monitor, beam monitor control box, and a data stream packetizer (DSP) board. The beam monitor control box, shown in Fig. 3.79, houses two main electronics boards: the beam monitor ethernet controller and the high-voltage module. Bias to the monitor anode is supplied by the high-voltage module. This module can receive an external interlock signal that quickly disrupts and lowers the bias voltage in the event of a vacuum leak or other undesired event. The FPGA on the controller configures the DAC settings for the preamplifier board and the high-voltage module. A network connection allows the ethernet controller to access these configurations and to remotely update the FPGA firmware.

Figure 3.80 shows an example of a beam monitor graphical user interface (operator interface [OPI]) used to control the beam monitor high voltage, control the comparator discriminator level, and display the TOF spectrum, among other features. The beam monitor ethernet controller receives the differential output signal from the beam monitor preamplifier and converts it to a logic-level, single-ended output. This signal is then passed to the onboard FPGA, where the signals can be locally acquired and used as diagnostic tools. The locally acquired histogram is

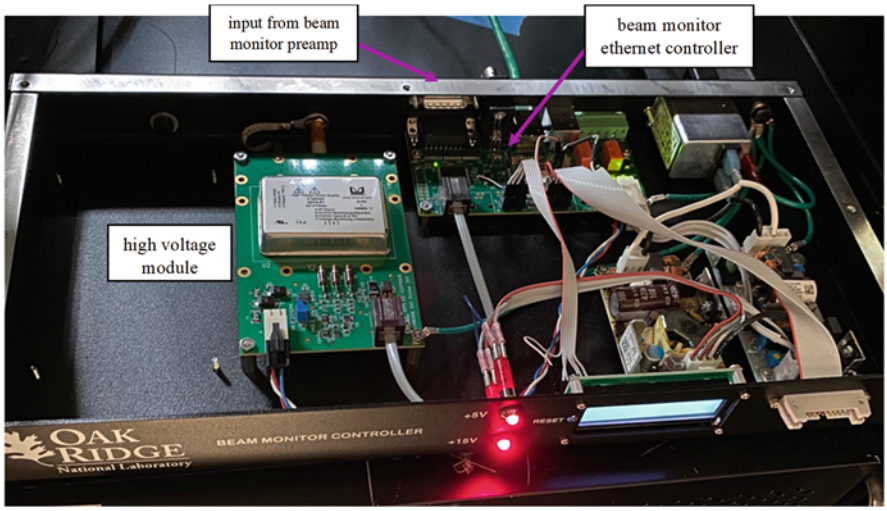

Fig. 3.79 Beam monitor control box

Fig. 3.80 Beam monitor OPI

transmitted to the instrument data acquisition system via the ethernet connection of the beam monitor ethernet controller. The beam monitor OPI reads this histogram and displays it as the blue bars shown in Fig. 3.80. The signal is also passed to a DSP

input. The DSP also receives signals from the accelerator, including a Tsync signal, which is synchronized to the times when the accelerator target generates bursts of neutrons. The DSP uses the difference in arrival times between the Tsync signal and the beam monitor signal to generate a time stamp. The DSP forwards this time stamp and the pixel ID associated with the beam monitor to the instrument data acquisition system. The data acquisition system reads this stream of beam monitor time stamps to create a TOF histogram. This histogram is displayed as the continuous red line overlapping the controller data in the TOF plot in Fig. 3.80.

3.8.8 Beam Monitor Characteristic Tests

Before any monitor is installed into a beamline at SNS or HFIR, it is first tested for overall performance characteristics to determine correct anode bias voltage and discriminator settings and to measure the monitor's efficiency for thermal neutrons. Typically, these tests are performed at the CG-1A experimental beamline located at the HFIR Cold Guide Hall. Here, a monochromatic neutron beam of approximately 4.2 Å is created via a pyrolytic carbon monochromator [32]. Figure 3.81 shows the CG-1A beamline layout. This beamline is allocated for the testing of new detector prototypes and configurations.

3.8.8.1 Beam Monitor Efficiency Test

Before installation, all beam monitors undergo a test to measure their efficiency for 1.8 Å neutrons, and this measured efficiency is compared with the manufacturer's designed efficiency for accuracy. To set up these tests, a control beam monitor with known efficiency is placed in the path of the neutron beam, and the monitor to be evaluated is placed closely behind it. A neutron absorber that is larger than the overall size of the largest beam monitor being tested is selected (usually borated aluminum), and an aperture roughly the size of the smallest monitor active area is

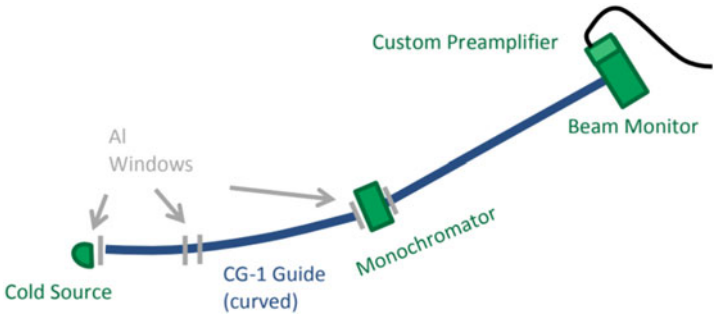

Fig. 3.81 Layout of beamline CG-1A located at the HFIR Cold Guide Hall [32]

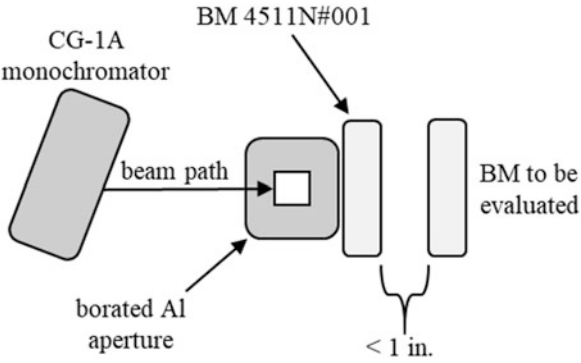

Fig. 3.82 Experimental setup for beam monitor (BM) efficiency test

created from it. This absorber is placed in front of the control beam monitor with the aperture aligned with the center of the active area of both monitors. An Ordela monitor designated as 4511N#001 is used as the control monitor for these tests because its known efficiency is 4.5×10^{-3} at 1.8 Å. Figure 3.82 illustrates this standard experimental setup.

Once set up, multiple acquisitions are collected at various bias voltages and discriminator threshold settings, and the count rates of the two monitors are compared to determine the new monitor's ideal operating condition. The efficiency for the new monitor is calculated using Eq. (3.124), where BM stands for beam monitor. This test only approximates the new beam monitor's efficiency as a ratio to that of the monitor with known efficiency characteristics. Some variables such as scatter or attenuation induced by the control monitor are not considered here.

$$\text{New BM eff.} = \frac{(\text{Control BM eff.}) \times (\text{New BM count rate})}{\text{Control BM count rate}} \tag{3.124}$$

In addition to the thermal efficiency measurement, tests have been conducted to determine the effects of inadequate anode bias and beam position within the beam monitor active area and the effects on efficiency for both. These tests were conducted on a ^{3}He monitor and a ^{14}N monitor at the CG-1A beamline with a similar setup to that shown in Fig. 3.82. For the first acquisition, the neutron beam was collimated using a 1 cm^2 aperture and positioned centered over one of the monitor's anode wires. Then, the acquisition was repeated, with the center of the collimated beam displaced 0.5 in. away from the anode wire toward the center of the monitor active area. The results for both monitors are shown in Fig. 3.83. The results show that adequate anode bias is a more critical parameter than the beam position on the monitor. With an inadequate anode bias, a substantial change in measured efficiency occurred when the neutron beam was not centered over the anode wire. This change makes sense considering that the electric field strength at low biases is not strong enough to create an output pulse with enough amplitude to trigger the discriminator electronics. As shown in Fig. 3.83, the on-anode and off-anode measurements agreed within approximately 4% at adequate anode biases.

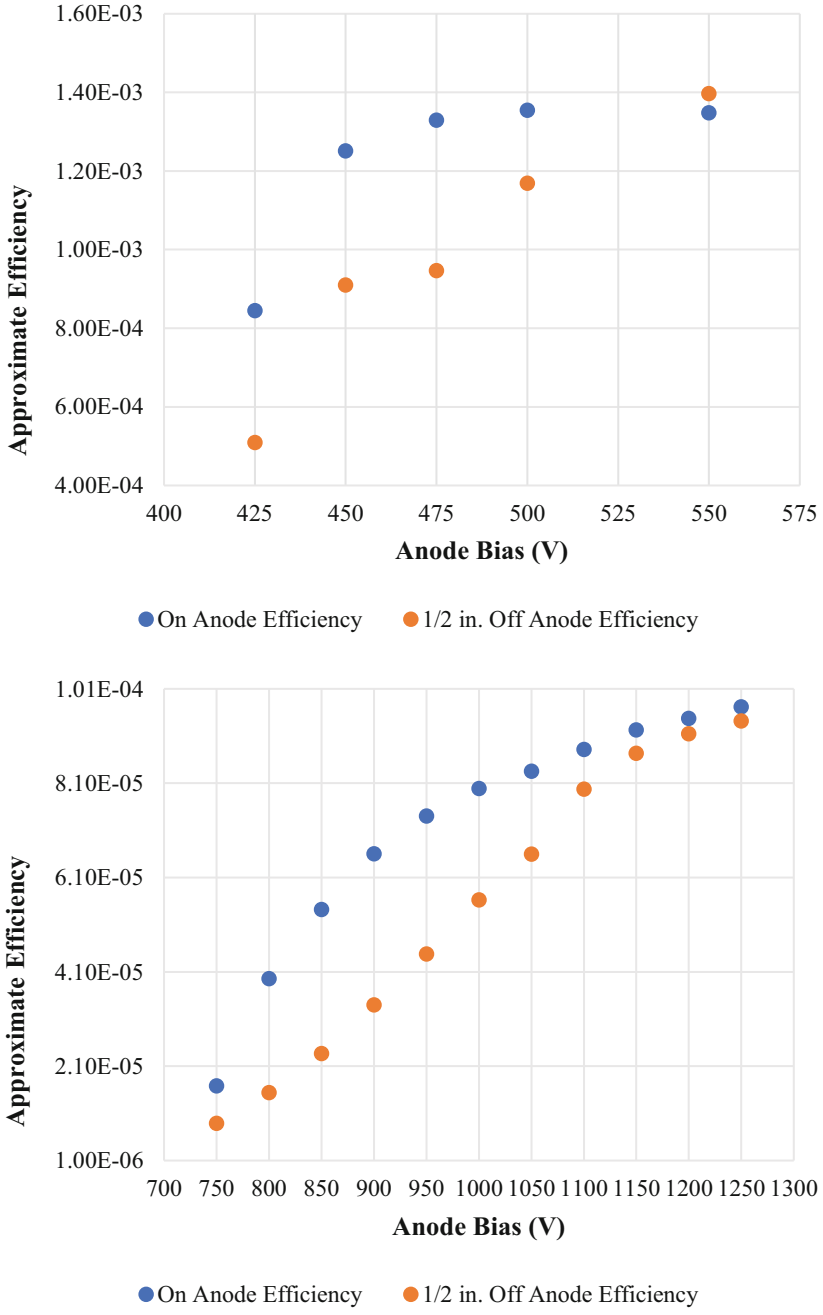

Fig. 3.83 Beam efficiency vs. anode bias voltage results for different beam positions. (*top*) ^{3}He monitor and (*bottom*) ^{14}N monitor

3.8.8.2 Beam Monitor Attenuation Test

Tests have been conducted at CG-1D in the HFIR Cold Guide Hall to determine the neutron wavelength-dependent transparency of a beam monitor. This beamline has a chopper at the beam port, which allows for neutron TOF calculations to measure the loss in count rate related to impinging neutron wavelength. Figure 3.84 illustrates the CG-1D beamline layout and the attenuation test setup.

The beam monitor in question is placed in the beam path with an aperture fixed in front of it to shield neutrons outside of the monitor's active area. Then, a high-efficiency (i.e., >95% at 1.8 Å) LPSD is placed behind it, and a TOF spectrum is taken on the high-efficiency detector. Next, the monitor is removed, and the measurement is taken again with only the LPSD. Finally, the count rate per wavelength for the two measurements can be compared to determine the percentage of rate lost per neutron wavelength. The results from this test are shown in Fig. 3.85. Using this method, the loss of beam intensity through Ordela monitor 4511N#001 was found to be approximately 5% over a wavelength spectrum from 1 to 10 Å.

3.8.8.3 Beam Monitor TOF Test

Neutron beam monitors at SNS can produce a TOF spectrum that can be used to determine the wavelength of the impinging neutron beam. The CG-1D beamline at HFIR has been used to test beam monitors for their accuracy in producing a reasonable time spectrum. The setup for this test was very similar to the attenuation test described previously except that no LPSD was required. The beamlines at HFIR

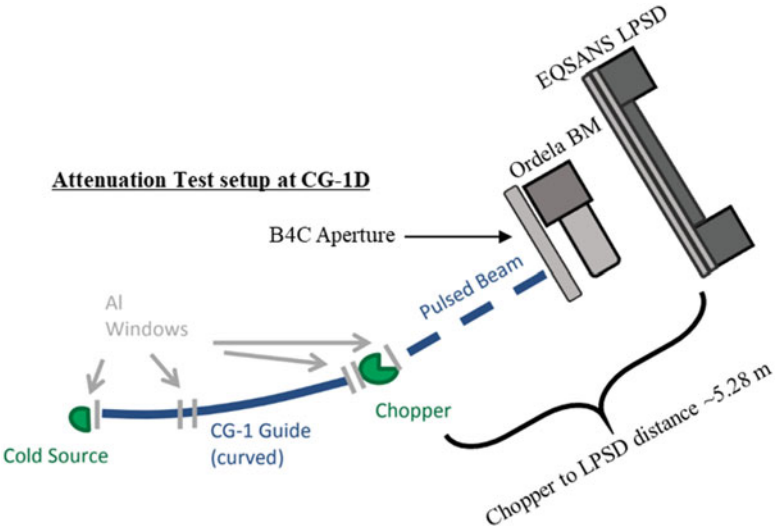

Fig. 3.84 CG-1D configuration and beam monitor attenuation test setup [32]

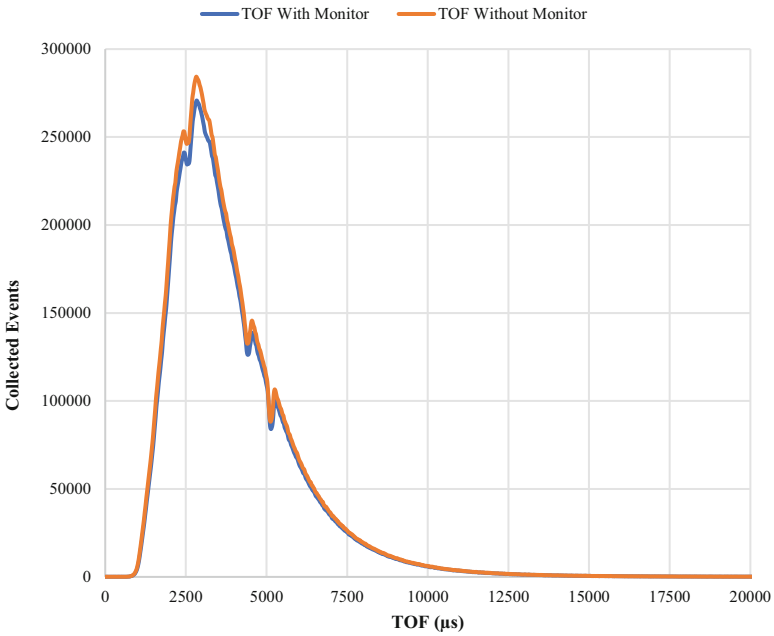

Fig. 3.85 Beam monitor wavelength-dependent attenuation test results

Table 3.6 Calculated results for aluminum attenuation based on Miller Indices using Eq. (3.125)

Al Miller Indices (h, k, l)	d_{hkl} (Å)	Wavelength (Å)	Calculated TOF (µs)	Delayed TOF (µs)
111	2.338	4.676	6242	7442
200	2.025	4.049	5405	6605
220	1.432	2.863	3822	5022
311	1.221	2.442	3259	4459
222	1.169	2.338	3121	4321

were built with aluminum windows, shown in Fig. 3.84, and they present a drop in transmitted neutrons at wavelengths parallel to the aluminum crystal lattice plane, at $\sin\theta = 1$ in Eq. (3.127), which is also known as Bragg's Law. Equation (3.125) details how the TOF is calculated. Table 3.6 gives the resulting calculations for the five aluminum crystal planes that can be seen in the 25 ms spectrum. The wavelength for the associated crystal lattice planes is calculated using Eq. (3.126) and Eq. (3.127), knowing that the lattice parameter (a) for aluminum is 4.05 Å, and n refers to the number of constructive harmonics of the given interatomic spacing (d_{hkl}) wavelength that fit within the timescale of the experiment—approximately 25 ms in this example. If the distance from the chopper to the beam monitor is known, then the TOF for these indices can be calculated and compared with the attenuation dips measured in the TOF spectrum to determine the monitor's TOF

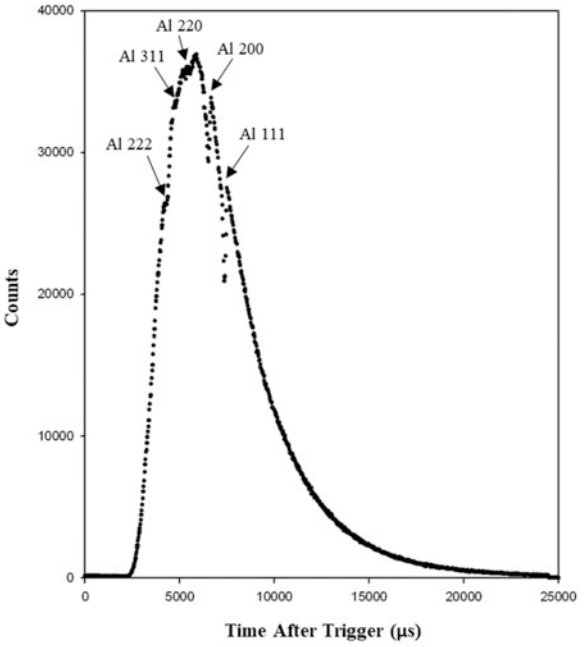

Fig. 3.86 TOF measurement results showing aluminum crystal lattice dips in transmission

capabilities. The arrival time of the timing signal is offset by 1200 μs from the chopper and the neutron pulse. This offset is captured in the measured waveform and is accounted for in the final column in Table 3.6. Comparing the calculated TOF for each of the indices and the measured results, as shown in Fig. 3.86, reveals that all the dips in neutron transmission measurement are close to the calculated time bin. Therefore, the monitor tested here is fully capable of producing an acceptable TOF spectrum.

$$\lambda = \frac{h}{mv} = \frac{3{,}956.0339 \times TOF}{D} \rightarrow TOF = \frac{D \times \lambda \mathrm{hkl}}{3{,}956.0339} + 1{,}200\ \mu\mathrm{s} \tag{3.125}$$

$$d_{hkl} = \frac{a}{\sqrt{h^2 + k^2 + l^2}} \tag{3.126}$$

$$\lambda = \frac{2\sin(\theta) d_{hkl}}{n} \tag{3.127}$$

3.8.9 Conclusion and Future Requirements

To conclude, a summary of some important performance characteristics for the MWPC beam monitor are shown in Table 3.7.

Table 3.7 Summary of performance characteristics for MWPC beam monitors

Performance characteristic	MWPC beam monitor
Thermal neutron efficiency	^{3}He: 10^{-3}–10^{-4}
	^{14}N: 10^{-4}–10^{-6}
Attenuation/scattering	4%–5%
Max count rate	~100,000 counts/s

The MWPC beam monitors are the default monitors employed at SNS and HFIR. The only real decisions made on a per-beamline basis are the number of beam monitors required, their location in the beamline, and their desired efficiencies. Because of this lack of attention, two surveys that asked how instrument beam monitors are used and what realistic improvements are desired were completed by SNS scientists in 2018 and HFIR scientists in 2021. These results were then compressed and tabulated to determine the beamline scientists' most pressing needs. The most-requested improvements are the following:

- Increased transparency of the neutron beam
- Position sensitivity
- Increased count rate
- Improved long-term stability

These findings have motivated efforts to identify and qualify commercially available monitors. Furthermore, research and development projects are focused on addressing one or more of the requested improvements.

One such commercially available monitor is a scintillator-based monitor manufactured by Quantum Detectors. This monitor was designed specifically for beamline diagnostics at the ISIS Neutron and Muon Source at the Rutherford Appleton Laboratory in the United Kingdom. The monitor was designed to provide a high level of neutron transparency, excellent neutron-to-gamma ray discrimination, and very high–count rate capabilities. Information pertaining to detailed performance characteristics for the ISIS beam monitor is contained in the literature [33, 34]. A sample monitor from Quantum Detectors was tested at BL-16B at SNS in December of 2014. The amplified detector signal was connected to a manufacturer-supplied discriminator card that was tuned to reject signals that fell below a 700 mV setting. This card produces a 200 ns width, −2 V amplitude pulse output per neutron absorption. Because each event produces the same output, the monitor is designed to be an event counter. These event pulses were fed to modified, SNS-style electronics to allow existing data acquisition software to be used for measurements and data logging.

To quantify the efficiency and count rate, the monitor was placed in front of an Ordela MWPC monitor with a known efficiency of 9.09×10^{-6} at 1.8 Å. A 1 mm thick borated aluminum plate with a 28 × 42 mm aperture was placed such that the aperture covered the quoted active area of the scintillating monitor while attenuating the beam elsewhere. The control monitor was placed 2 cm downstream of the scintillating monitor and had an 8 mm thick borated plate with a similar aperture cut into it to effectively mimic the same active area of the scintillating monitor. Once set up, the monitors sampled the neutron beam for approximately 20 min. The TOF

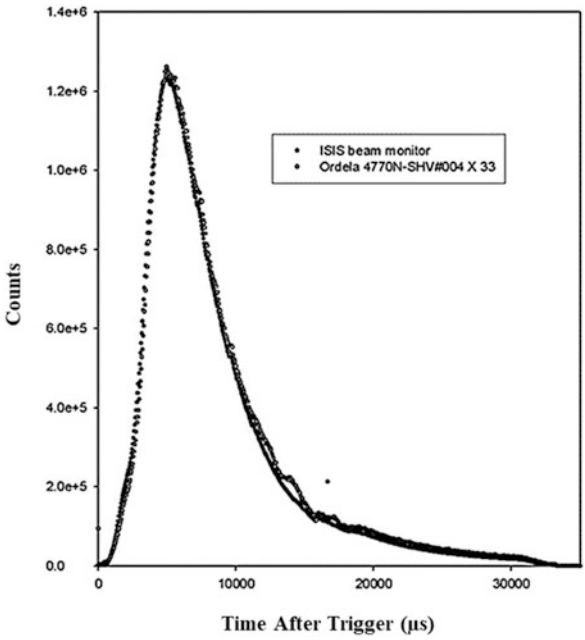

Fig. 3.87 TOF spectrum comparing ISIS beam monitor and MWPC monitor

spectrum results comparing the two monitors are shown in Fig. 3.87. The ISIS beam monitor was shown to track the TOF spectrum of the MWPC monitor extremely well. The efficiency of the Quantum Detectors scintillating bead monitor was calculated using Eq. (3.124) as approximately 2.9×10^{-4}. The ISIS monitor was tested up to 150,000 counts per second without saturation, which equates to approximately 1×10^{9} range beam flux. Upon completion of these tests, an ISIS monitor was purchased and commissioned for SNS BL-4A.

An R&D project was conducted to find a high–count rate and high–dynamic range beam monitor that ideally would not use ^{3}He as the conversion isotope. The monitor was based on a parallel-plate design inside a gas-filled enclosure. During project development, several different combinations of electrode materials, fill gas composition, and neutron conversion materials were used to determine a wide range of operating characteristics for this design. A particular combination yielded a count rate of 1×10^{6} counts per second at a thermal neutron efficiency of 10^{-3} without saturation. The data for this combination indicates that this specific monitor design can measure a neutron beam with a thermal flux rate of 1×10^{9} neutrons per second. All the information pertaining to the parallel-plate avalanche beam monitor was retrieved from a master's thesis, under which the project results were summarized [32]. Table 3.8 summarizes the results from this project and the different design methods that were tested.

In 2022, a research and development effort began that aimed to produce beam monitors based on semiconductor technology. Owing to their fast electron drift velocity, these devices provide superior high–count rate capabilities compared

Table 3.8 Parallel-plate beam monitor R&D summary of results and attempted designs

Beam monitor design A–C–isotope	Measured neutron efficiency	Expected beam flux that can be measured	Approximate flux used for measurement
Quartz–aluminum–^{3}He	$(4.0 \pm 0.5) \times 10^{-4}$	4.0×10^{10}	$(3.0 \pm 0.8) \times 10^{9}$
Alumina–aluminum–^{3}He	$(1.0 \pm 0.5) \times 10^{-5}$	1.0×10^{11}	$(1.4 \pm 0.2) \times 10^{8}$
Alumina–boron-doped silicon	$(1.1 \pm 0.3) \times 10^{-5}$	1.1×10^{11}	$(1.1 \pm 0.6) \times 10^{5}$
Silicon–boron-doped silicon–^{3}He	$(1.2 \pm 0.2) \times 10^{-3}$	1.2×10^{9}	$(1.4 \pm 0.2) \times 10^{8}$
Alumina–aluminum–LiF sample 1	$(2.2 \pm 0.5) \times 10^{-6}$	2.2×10^{12}	$(4.1 \pm 0.4) \times 10^{8}$
Alumina–aluminum–LiF sample 2	$(9.8 \pm 0.6) \times 10^{-7}$	9.8×10^{13}	$(4.1 \pm 0.4) \times 10^{8}$

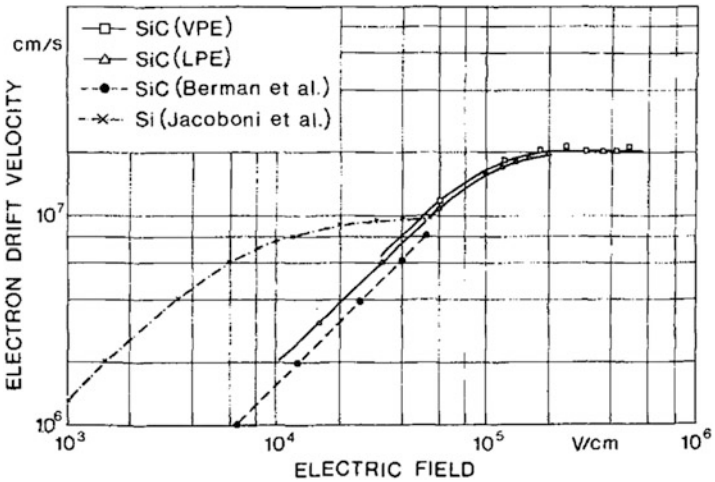

Fig. 3.88 Electron drift velocity vs. electric field potential for silicon [35]

with the MWPC beam monitors. As shown in Fig. 3.88, at very high electric fields (5×10^5 V/cm), the saturated electron drift velocity (v_s) approaches 2×10^{11} μm/s [35]. With this value, Eq. (3.128) calculates that the expected transit time (T_t) for electrons in the 300 μm thick ($Si_{\text{Thickness}}$) silicon semiconductor beam monitor is approximately 1.5 ns. By employing custom readout electronics that have 15 ns resolution time, the readout system for these monitors can track this electron drift alone. This ability allows for up to three orders of magnitude faster readout capabilities (theoretically, greater than 100×10^6 counts per second) than the MWPC, which is limited by the drift time of the heavier positive ions. For this project, two monitors are being constructed; one will provide a zero-dimensional counting mode

design that will be used as a high-rate flux monitor, and the second is being constructed as a 2D, position-sensitive design that can be used for beam profiling. Theoretically, by using semiconductors that have natural boron as the p-type doping material and the flexibility of adding either a ^{10}B or ^{6}Li layer on the entrance window, monitors of this design enable a controllable variation in thermal neutron absorption efficiencies.

$$T_t = \frac{Si_{\text{Thickness}}}{V_s} \approx 1.5 \text{ ns} \tag{3.128}$$

References

1. W-values from ICRU Report 31, "Average Energy Required to Produce an Ion Pair," International Commission on Radiation Units and Measurements, Washington D.C. 1979.
2. R.K. Crawford, Position Sensitive Detection of Slow Neutrons: Survey of Fundamental Principles. In *Proceedings of SPIE International Symposium on Optical Applied Science and Engineering*, San Diego, CA, July 19–24, 1992. https://www.osti.gov/servlets/purl/5095599
3. A. Doumas, G.C. Smith, Comparison of various stopping gases for ^{3}He-based position sensitive neutron detectors. Nucl. Instrum. Methods Phys. Res., Sect. A **675**, 8–14 (2012). https://doi.org/10.1016/j.nima.2012.01.035
4. V. Radeka, N.A. Schaknowski, G.C. Smith, B. Yu, High precision thermal neutron detectors, in*Neutrons in Biology*, Basic Life Sciences, ed. by B.P. Schoenborn, R.B. Knott, vol. 64, (Springer, Boston, 1996), pp. 57–67
5. E. Storm, H.I. Israel, Photon cross sections from 1 keV to 100 MeV for elements Z = 1 to Z = 100. Nucl. Data Tables **A7**, 565–688 (1970). https://doi.org/10.1016/S0092-640X(70)80017-1
6. X Ray Proportional Counter. *PhysicsOpenLab*. 23 July 2017. https://physicsopenlab.org/2017/07/23/x-ray-proportional-counter-2/
7. I. Dioszegi, B. Yu, G. Smith, N. Schaknowski, J. Fried, P.E. Vanier, C. Salwen, L. Forman, A new pad-based neutron detector for stereo coded-aperture thermal neutron imaging, in *Proceedings of 2013 IEEE Nuclear Science Symposium and Medical Imaging Conference*, Seoul, South Korea, October 27–November 2, 2013. https://doi.org/10.1109/NSSMIC.2013.6829416., https://ieeexplore.ieee.org/stamp/stamp.jsp?tp=&arnumber=6829416
8. N. Schaknowski, J. Fried, G. Smith, G. Mahler, B. Yu, Design and construction of a 1 m × 1 m thermal neutron imager operating in ionization mode with pad readout, in *Proceedings of 2018 IEEE Nuclear Science Symposium and Medical Imaging Conference*, Sydney, Australia, November 10–17, 2018. https://doi.org/10.1109/NSSMIC.2018.8824283., https://ieeexplore.ieee.org/stamp/stamp.jsp?tp=&arnumber=8824283
9. G.F. Knoll, *Radiation Detection and Measurement*, 4th edn. (Wiley, 2010)
10. W. Diethorn, A Methane Proportional Counter System for Natural Radiocarbon Measurements. Thesis, Carnegie Inst. of Tech., Pittsburgh, PA, 1956
11. K.D. Berry, et al., Characterization of the neutron detector upgrade to the GP-SANS and Bio-SANS instruments at HFIR. Nucl. Instrum. Methods Phys. Res., Sect. A **693**, 179–185 (2012). http://dx.doi.org/10.1016/j.nima.2012.06.052
12. W. Shockley, Currents to conductors induced by a moving point charge. J. Appl. Phys. **9**(10), 635 (1938). https://doi.org/10.1063/1.1710367
13. S. Ramo, Currents induced by electron motion. Proc. IRE **27**(9), 584–585 (1939). https://doi.org/10.1109/JRPROC.1939.228757

14. D. McGregor, J.K. Shultis, *Radiation Detection: Concepts, Methods, and Devices* (CRC Press, 2020)
15. Analog Devices, Inc *Data Sheet AD8022, Rev. C*, 2011
16. J. Alberi, J. Fischer, V. Radeka, L.C. Rogers, B. Schoenborn, A two-dimensional position-sensitive detector for thermal neutrons. Nucl. Instrum. Methods **127**(4), 507–523 (1975). https://doi.org/10.1016/0029-554X(75)90654-0
17. B. Yu, J.A. Harder, J.A. Mead, V. Radeka, N.A. Schaknowski, G.C. Smith, Neutron detector development at Brookhaven. Nucl. Instrum. Methods Phys. Res., Sect. A **513**(1–2), 362–366 (2003). https://doi.org/10.1016/j.nima.2003.08.063
18. J. Fried, J.A. Harder, G.J. Mahler, D.S. Makowiecki, J.A. Mead, V. Radeka, N.A. Schaknowski, G.C. Smith, B. Yu, A large, high performance, curved 2D position-sensitive neutron detector. Nucl. Instrum. Methods Phys. Res., Sect. A **478**(1–2), 415–419 (2002). https://doi.org/10.1016/S0168-9002(01)01787-9
19. V. Radeka, et al., in: B.P. Schoenborn, R.B. Knott (Eds.), Neutrons in Biology, Plenum Press, New York, 1996, pp. 57-67.
20. B. Yu, et al., Nucl. Instr. Meth. A **513**, 362-366 (2003).
21. B. Yu, Z. Zojceski, J.A. Harder, A. Hrisoho, V. Radeka, G.C. Smith, Front-end electronics for high rate, position sensitive neutron detectors. Nucl. Instrum. Methods Phys. Res., Sect. A **485**(3), 645–652 (2002). https://doi.org/10.1016/S0168-9002(01)02111-8
22. ORNL generated image.
23. J. Fried, et al., Advanced two-dimensional thermal neutron detectors for scattering studies Proc. SPIE 4785, Advances in Neutron Scattering Instrumentation, (18 November 2002); https://doi.org/10.1117/12.456300.
24. Photo courtesy Graham C. Smith, Brookhaven National Laboratory, Upton, New York
25. ORNL generated image courtesy Matthias Frontzek
26. *2410N Test and Calibration Report*; (ORDELA Inc., Oak Ridge, 2011)
27. G. Mauri, Development and Characterization of Detectors for Large Area Application in Neutron Scattering and Small Area Application in Neutron Reflectometry. PhD Thesis, Universita Degli Studi di Perugia, Perugia, Italy, 2019
28. Electric Power Research Institute. Portable Survey Instruments: RP0201 Approved Rev. SlideToDoc, retrieved August 19, 2022. https://slidetodoc.com/portable-survey-instruments-rp-02-01-approved-rev/
29. G. Charpak, F. Sauli, High-resolution electronic particle detectors. Ann. Rev. Nucl. Part. Sci. **34**, 285–349 (1984). https://doi.org/10.1146/annurev.ns.34.120184.001441
30. K.D. Berry, *Neutron Lifecycle Series: Helium-3 Gas Detectors at the SNS and HFIR*, The Neutron Lifecycle Lecture Series (Oak Ridge National Laboratory, 2016)
31. J. Lowke, The drift velocity of electrons in hydrogen and nitrogen. Australian J. Phys. **16**(1), 115–135 (1963). https://doi.org/10.1071/PH630115
32. A.K. Barnett, Investigation of Higher Count Rate and Helium-3 Alternative Beam Monitors for Neutron Scattering Facilities. MS Thesis, The University of Tennessee, Knoxville, TN (2013)
33. F. Issa, A. Khaplanov, R. Hall-Wilton, I. Llamas, M.D. Riktor, S.R. Brattheim, H. Perrey, Characterization of Thermal Neutron Beam Monitors. *arXiv* (*physics.ins-det*), February 3, 2017, 1702.01037v1. https://arxiv.org/pdf/1702.01037
34. Quantum Detectors, *Operational Guide for the ISIS Neutron Beam Monitor*. Retrieved April 7, 2022. ISIS-Neutron-Beam-Monitor (kosinc.co.kr)
35. W.V. Muench, E. Pettenpaul, Saturated electron drift velocity in 6H silicon carbide. J. Appl. Phys. **48**, 4823 (1977). https://doi.org/10.1063/1.323506